Technische Universität München
Fakultät für Elektrotechnik und Informationstechnik

Sensing of Metabolites using Optoacoustic Spectroscopy

Mir Mehdi Seyedebrahimi

Vollständiger Abdruck der von der Fakultät für Elektrotechnik und Informationstechnik der Technischen Universität München zur Erlangung eines Doktors der Ingenieurwissenschaften (Dr.-Ing.) genehmigten Dissertation

Vorsitz: Prof. Dr.-Ing. habil. Dr. h.c. Alexander W. Kock
Prüfer der Dissertation:
1. Prof. Dr. Vasilis Ntziachristos
2. Prof. Dr. Ghulam Destgeer

Die Dissertation wurde am 22.03.2021 bei der Technischen Universität München eingereicht und durch die Fakultät für Elektrotechnik und Informationstechnik am 03.11.2021 angenommen.

Dedication
To my Wife and Parents.

Abstract

Non-invasive glucose sensing has been a long sought after target in diabetes management, promising to avoid the inconvenient monitoring of blood glucose based on direct blood measurements by finger prick. Currently, reliable glucose sensing is done with the Clarke electrode, which requires invasive blood measurements, which are inconvenient for daily use. Minimally invasive biochemical sensing (mostly transdermal) has offered a promising alternative to glucose sensing, avoiding the use of blood samples. However, these technologies indirectly sense glucose in the interstitial fluid, sweat, salvia, or tear, and not in blood, coming with a recommendation to verify traditional blood sampling readings. Moreover, transdermal measurements of glucose concentrations suffer from low reproducibility because of changes in the volumes of extracted tear, salvia, sweat, or ISF, dilution, and evaporation of these fluids prior to sampling, as well as contamination, irritation, and variations in skin temperature and pH. Optical and optoacoustic methods have also been investigated for glucose sensing and offer non-invasive operation, which provides better tolerability and safety over fluid sensing techniques. Despite these advances, the accuracy and precision of previously reported optical and optoacoustic studies are all limited by their use of indiscriminate “bulk skin” measurements to quantify glucose. These inaccuracies can arise from variations in background absorption between different skin layers. Last but not least, all previous optical and optoacoustic methods are limited when measuring target molecules in aqueous solution by strong water absorption, particularly at infrared wavelengths, reducing detection sensitivity.

In this study, we propose a new non-invasive glucose measuring concept that senses glucose within the blood vasculature, i.e., at the organ of interest where glucose offers

the highest concentration. This is achieved by a layer-specific optoacoustic sensor (LSOS) operating in the short-wavelength infrared (SWIR). Powered by machine learning, LSOS identifies different skin layers and characterizes glucose concentration in the highly vascular hypodermal plexus. Validated against blood-glucose strips serving as the gold-standard, we observed that the hypodermis' glucose measurements showed a higher correlation coefficient. We conclude that layer-specific detection is essential for optical measurements through the skin and can lead to a new portable glucose sensing concept.

To avoid the problem of water absorption, which is a common problem in all IR spectroscopies, we suggested another technique to push the limitation of previous spectroscopy techniques. Based on the optoacoustic signal's dependence on the temperature of the probed medium, we introduce cooled IR optoacoustic spectroscopy (CIROAS) to mute water contributions in optoacoustic spectroscopy. We showcase that spectral measurements of proteins, lipids, and glucose in the short-wavelength infrared (SWIR) region, performed at 4 °C, lead to marked sensitivity improvements over conventional optoacoustic or IR spectroscopy. We elaborate on optoacoustic signals' dependence on water temperature and demonstrate polarity changes in the recorded signal at temperatures below 4 °C. We further elucidate the optoacoustic signal's dependency and the muting temperature on sample concentration and demonstrate that changes in these dependencies enable quantification of the solute concentration. We discuss how CIROAS may enhance the abilities for molecular sensing in the infrared.

Abstrakt

Nicht-invasive Glukoseerfassung ist seit langem ein begehrtes Ziel bei der Behandlung von Diabetes und verspricht, die unbequeme Überwachung des Blutzuckers auf der Grundlage direkter Blutmessungen mit einem Fingerabdruck zu vermeiden. Derzeit erfolgt eine zuverlässige Glukoseerfassung mit der Clarke-Elektrode, für die invasive Blutmessungen erforderlich sind, die aber für den täglichen Gebrauch unpraktisch sind. Die minimal-invasive biochemische Messung (meistens transdermal) bietet eine vielversprechende Alternative zur Glukoseerfassung, wobei die Verwendung von Blutproben vermieden wird. Diese Technologien erfassen jedoch indirekt Glukose in der interstitiellen Flüssigkeit, im Schweiß, im Salvia oder in der Träne und nicht im Blut, und es dabei wird empfohlen, die herkömmlichen Blutproben zu überprüfen. Darüber hinaus leiden transdermale Messungen der Glukosekonzentrationen unter einer geringen Reproduzierbarkeit aufgrund der Änderungen des Volumens der extrahierten Tränen, Salbei, Schweiß oder ISF, Verdünnung und Verdunstung dieser Flüssigkeiten vor der Probenahme sowie Kontamination, Reizung und Hautveränderungen Temperatur und pH. Optische und optoakustische Methoden wurden ebenfalls für die Glukoseerfassung untersucht und bieten eine nicht-invasive Funktionsweise, der eine bessere Verträglichkeit und Sicherheit gegenüber Flüssigkeitserfassungstechniken bietet. Trotz dieser Fortschritte sind die Genauigkeit und Präzision der zuvor gemeldeten optischen und optoakustischen Studien durch die Verwendung wahlloser Messungen der Hautmasse zur Quantifizierung von Glukose begrenzt. Diese Ungenauigkeiten können sich aus Schwankungen der Hintergrundabsorption zwischen verschiedenen Hautschichten ergeben. Last but not least sind alle bisherigen optischen und optoakustischen Verfahren begrenzt, wenn Zielmoleküle in wässriger Lösung durch starke Wasserabsorption, insbesondere bei Infrarotwellenlängen, gemessen werden, wodurch die Nachweisempfindlichkeit verringert wird.

In dieser Studie schlagen wir ein neues nicht-invasives Glukosemesskonzept vor, das Glukose im Blutgefäßsystem erfasst, d. H. An dem interessierenden Organ, an dem Glukose die höchste Konzentration bietet. Dies wird durch einen schichtspezifischen optoakustischen Sensor (LSOS) erreicht, der im kurzwelligen Infrarot (SWIR) arbeitet. Durch maschinelles Lernen identifiziert LSOS verschiedene Hautschichten und charakterisiert die Glukosekonzentration im hochvaskulären Plexus hypodermalis.

Validiert gegen Blutzuckerstreifen, die als Goldstandard dienen, beobachteten wir, dass die Glukosemessungen der Hypodermis einen höheren Korrelationskoeffizienten zeigten. Wir schließen daraus, dass die schichtspezifische Detektion für optische Messungen durch die Haut wesentlich ist und zu einem neuen tragbaren Glukose-Sensorkonzept führen kann.

Um das Problem der Wasserabsorption zu vermeiden, das bei allen IR-Spektroskopien häufig auftritt, haben wir eine andere Technik vorgeschlagen, um die Beschränkung früherer Spektroskopietechniken zu verschieben. Basierend auf der Abhängigkeit des optoakustischen Signals von der Temperatur des untersuchten Mediums führen wir die gekühlte optoakustische IR-Spektroskopie (CIROAS) ein, um die Wasserbeiträge in der optoakustischen Spektroskopie zu dämpfen. Wir zeigen, dass spektrale Messungen von Proteinen, Lipiden und Glucose im kurzwelligen Infrarotbereich (SWIR) bei 4 ° C zu deutlichen Empfindlichkeitsverbesserungen gegenüber herkömmlicher optoakustischer oder IR-Spektroskopie führen. Wir gehen auf die Abhängigkeit optoakustischer Signale von der Wassertemperatur ein und zeigen Polaritätsänderungen im aufgezeichneten Signal bei Temperaturen unter 4 ° C. Wir untersuchen die Abhängigkeit des optoakustischen Signals und die Muting-Temperatur von der Probenkonzentration weiter und zeigen, dass Änderungen dieser Abhängigkeiten eine Quantifizierung der Konzentration gelöster Stoffe ermöglichen. Wir erforschen, wie CIROAS die Fähigkeit zur molekularen Erfassung im Infrarot verbessern kann.

Acknowledgment

It would be impossible to fulfill justice if I were to try to fully appreciate or even name all individuals who have helped me with their words, support, advice, or sheer presence along the path of my doctoral studies.

Foremost, I wish to thank my supervisor Professor Vasilis Ntziachristos for giving me the opportunity to work in this exciting field under his supervision. I appreciate all the intriguing research ideas and accurate scientific judgments and provide me with the freedom and independence to pursue my intuition. I appreciate his dedication to guiding and supporting me throughout my Ph.D.

I am greatly indebted to Dr. Jaya Prakash and Dr. Pouyan Mohajerani, who were outstanding mentors, colleagues, and friends. They have helped me to view science from a different perspective, sharing their experience in research. I further appreciate Dr. Miguel Pleitz, Dr. Ara Ghazarian, Dr. Vipul Gujreti, Dr. Juan Pablo, and Dr. Andre Stiel, for their helpful and encouraging comments.

I would also like to thank my colleagues at the institute for biological and medical imaging (IBMI), Helmholtz Zentrum München (HMGU), and TranslaTUM: Bingwen Wang, Parastoo Afshari, Jaber Malekzadeh, Dr. Razansky, Dr. Stiel, Dr. Zakian, Qutaiba Mustafa, Roman Shnaiderman, Zak Ali, Yuanhui Huang, Kanuj Mishra, who supported me and made this Ph.D. a beautiful adventure.

I would like to thank the entire administrative group at IBMI for their help in all administrative matters during my Ph.D.: Susanne Stern, Dr. Andreas Hillmair, Pro. Dr. Karl-Hans Englmeier, Dr. Roland Boha, Dr. Nike Tsalas, Dr. Christina Nagler, Dr. Julia Thomas, Ines Baumgartne, Dr. Bettina Lehman, Lidia Seidl, Dr. Doris Bengel, Dr.

Manfred Tuerke. I appreciate Pia Anzenhofer, Uwe Klemm, and Sarah Glasl, for their exemplary assistance in the lab. I appreciate the editing assistance of Dr. Chapin Rodríguez, Dr. Robert Wilson, and Dr. Sergey Sulima. I am particularly grateful to thank prof. Dr. Mickaël Tanter and prof. Dr. Murat Eyuboglu, whose way was inspiring for me in my entire research and carrier course.

I would also like to thank TUM, Helmholtz research center, and the European Research Council (ERC) under the European Union’s Horizon 2020 research and innovation programme under grant agreement No 694968 (PREMSOT) as part of my research support, without which this thesis would not have been possible.

Last but not least, I would like to express my deepest thanks to my parents, my sister Maryam, my brother Morteza, my nephew Mani, and my mother, sister, and brother in law for always being supportive of my career and for their unconditional love. Research is a collaborative, but also very solitary, environment, which makes such support invaluable. The constant support of my family and friends is what helped me complete my work.

My most heartfelt appreciation is for my kind, lovely and beautiful wife, Maryam Karimi, for all her love, dedication, and support along this path. She is the meaning of my life. I have not made it without her; of this, I am very sure.

Contents

ABSTRACT .... **IV**

ABSTRAKT .... **VI**

ACKNOWLEDGMENT .... **VIII**

ACRONYM .... **XIII**

1 INTRODUCTION **1**

1.1 GOALS AND OBJECTIVES 5
1.2 STRUCTURE OF DISSERTATION AND OUTLINE 6

2 THEORETICAL BACKGROUND **8**

2.1 OPTICAL TECHNIQUES TO DETECT GLUCOSE 9
2.1.1 Near-infrared Spectroscopy 9
2.1.2 Mid-Infrared Spectroscopy 10
2.1.3 Raman Spectroscopy 10
2.1.4 Fluorescence spectroscopy 11
2.1.5 Optical coherent tomography (OCT) 11
2.1.6 Optoacoustic Spectroscopy 12
2.2 GOVERNING EQUATIONS OF THE OPTOACOUSTIC EFFECT 14
2.2.1 Initial pressure elevation following the illumination with pulsed laser 14
2.2.1. Optoacoustic wave propagation 16
2.2.3. Sound propagation in a biological sample 18
2.2.4. Optoacoustic signal attenuation 20
2.3. ULTRASOUND DETECTORS 20

3 LAYER-SPECIFIC OPTOACOUSTIC SENSOR FOR A NON-INVASIVE GLUCOSE DETECTION SENSITIVITY OF THE SKIN **24**

3.1 INTRODUCTION 24
3.2 METHOD 25
3.2.1 Experimental Setup 25
3.2.2 Data analysis – Algorithm 28
3.2.2.1 SIGNAL TO NOISE IMPROVEMENT - PULSE-TO-PULSE CORRECTION. 29
3.2.3 Comparison of glucose versus water absorption spectra 36
3.2.4 In-vivo measurements 38
3.3 RESULTS AND ANALYSIS 41
3.4 CONCLUSION AND DISCUSSION 52

4 SHORT WAVELENGTH OPTOACOUSTIC SPECTROSCOPY BASED ON WATER MUTING **56**

4.1 LITERATURE AND THEORETICAL BACKGROUND 56
4.2 INTRODUCTION 58
4.3 METHOD 59
4.3.1 Theory 59
4.3.2 Cooled IR Optoacoustic Spectroscopy 62
4.3.3 Data collection and processing 64
4.3.4 Experimental Measurements. 64
4.4. RESULTS 65
4.5. CONCLUSION AND DISCUSSION 77

5 FUTURE AND OUTLOOK **81**

LIST OF FIGURES **85**

LIST OF TABLES **91**

BIBLIOGRAPHY **92**

LIST OF PUBLICATIONS **99**

Acronym

AMP	Amplifier
ARE	Absolute relative error
BS	Beam splitter
BSA	Bovine serum albumin
CC	Correlation coefficient
CIROAS	Cooled IR optoacoustic spectrometer
DAQ	Data acquisition card
FTIR	Fourier transform infrared
HWP	Half-wave plate
IR	Infrared
LOD	Limit of detection
LOOC	Leave one out cross-validation
LSOS	Layer-selective optoacoustic sensor
MIR	Mid-infrared
NIR	Near-infrared
NIRS	Near-infrared spectroscopy
OA	Optoacoustic
OAI	Optoacoustic intensity
OAS	Optoacoustic spectroscopy
OCT	Optical cohorent tomography
PBS	Phosphate-buffered saline
PC	Personal Computer
SD	Standard deviation

SNR	Signal to noise ratio
SWIR	Short-wavelength near-infrared
UST	Ultrasound transducer
UV	Ultraviolet

1 Introduction

Diabetes is a chronic metabolic disorder that is considered to be one of the main threats to human health in the 21st century, mainly because of lifestyle changes [1]. More than 420 million humans suffer due to diabetes worldwide [1], and the incidence rate is increasing. A primary necessity for diabetes management today relies on frequent and accurate glucose sensing. Glucose sensing could enable maintain blood glucose at normal levels and guide the dosage of insulin to be administered [2]. The conventional glucose sensor, the glucometer, is a biochemical sensor that requires an invasive measurement (fingerpick) to obtain blood for direct glucose measurement. The Clark electrode, first introduced by Leland Clark in 1962 [3], is a sensor that uses an enzyme electrode that converts glucose concentration to electrical current. Nevertheless, despite its widespread use, the need for frequent glucose monitoring has launched wide-reaching research into technologies that could detect blood glucose levels without the need to obtain blood droplets (invasive measurement). Repeated glucose measurement is required for proper diabetes management, and any invasive approach leads to large discomfort to the patients. The non-invasive measurement of blood glucose has thus become a Holy Grail in the management of diabetes, and several alternative approaches are being investigated to produce a new generation of glucose sensors.

Minimally invasive approaches for glucose detection have been pursued in recent years. The most promising of these technologies are based on transdermal electro-impedance spectroscopy or electro-osmosis techniques, wherein sweat is extracted from the skin surface, or interstitial fluid (ISF) is extracted; these fluids are then used to measure metabolites by enzyme electrodes [4], [5]. These techniques are the basis for the Gluco Watch Biographer [6], tattoo based iontophoresis [4], and path selective iontophoresis [7]. However, transdermal measurements can lead to skin irritation due to the electrical current needed to extract sweat or ISF. Furthermore, the glucose concentrations in sweat and ISF do not directly represent the concentration of glucose in the blood, as analytes enter these fluids by diffusion from surrounding capillaries (leading to dilution of 10-1000 times in ISF and sweat, respectively) [8], [9]. The transdermal measurements of glucose concentrations suffer from low reproducibility because of changes in the volumes of extracted sweat or ISF, evaporation of these fluids prior to sampling, and other variations like skin temperature and pH. As a result of transdermal sensors' unreliability, readings often need to be calibrated by a conventional finger-prick test before each measurement, resulting in not repeatable glucose readings.

Saliva [10], [11] and tears [12], [13] are also desirable targets to be sampled for indirect, non-invasive blood glucose quantification, as they contain readily accessible biomarkers, including glucose [14]. However, glucose concentrations in saliva and tears correlate even more poorly (diluted more than 1000 times) with blood glucose concentration than using ISF and sweat. Furthermore, it is also challenging to obtain consistent glucose measurements from saliva and tears due to irregular fluid excretion rates, very low glucose concentrations, contamination, and variations in pH and temperature. Thus, glucose measurements from saliva and tear are not reliable and reproducible [8], [9]. Such limitations led to the discontinuation of work on the ocular wearable biosensor, produced in a collaboration between Google and Novartis [12]. Optical methods have also been investigated for glucose sensing and offer non-invasive operation, which provides better tolerability and safety over fluid sensing techniques. Generally, optical glucose sensing relies on detecting a change in the tissue interrogated optical property as a function of glucose concentration. Spectroscopic techniques have been proposed in the near-infrared (NIR, 750 – 1300 nm), short-wavelength infrared (SWIR, 1300 – 2500 nm), or mid-infrared (MIR, 2500 – 10000 nm) [15]–[17] for detecting wavelength-specific changes in optical absorption due to glucose concentration [15]'[18]. However, optical detection of glucose is complicated due to strong background signals from other tissue moieties. Moreover, due to the strong photon scattering in tissue, optical sensing interrogates bulk tissue measurements, diluting the glucose signal's contribution and reducing sensitivity. In addition, the varying optical properties of different skin types and tissues [19], [20] further affect the signal recorded and therefore the accuracy of the glucose concentration measurements. The mid-infrared region has gained wide-spread attention for glucose sensing [21]–[25] since the absorption signal of glucose in this spectral region is narrower and more pronounced than other optical wavelength bands, potentially leading to higher accuracy, sensitivity, and specificity in glucose detection. However, MIR detection suffers from low penetration (only a few micrometers) in the skin due to high attenuation by water, as well as expensive light sources, which has limited the development of glucose measurement devices. Scattering contrast has also been explored for glucose sensing. In principle, Raman scattering provides sharp glucose spectral signatures that offer good contrast over the background [26]. However, the signal-to-noise ratio achieved is generally very low, necessitating very long acquisition times prone to measurement errors [27]. Optical coherent tomography (OCT) has also been applied for noninvasively determining the glucose concentration by measuring changes in the index of refraction as a function of glucose concentration. Although the technology showed promise in clinical trials carried out by the company GlucoLight [28], OCT is limited by its sensitivity to motion, skin temperature, pH, and humidity. Furthermore, the measured signal changes are relatively small and can be disproportionally affected by other physiological parameters [29]. These confounding factors have limited the application of optical techniques for accurate glucose sensing: despite decades of research with optical interrogation, no optical technology has so far been successfully applied to clinical practice.

Recently, optoacoustic methods have been considered as an alternative to optical technologies for glucose sensing. Optoacoustic operates by using light to generate ultrasonic waves in the biological tissue. The absorption of transient light energy generates ultrasound by tissue absorbers due to thermoelastic expansion. By using ultrasound detection instead of photon detection, optoacoustic sensors can measure in reflection mode; in contrast to optical spectroscopy, which typically requires transmission measurements [30]. This principle has been put to use in mid-infrared (MIR) optoacoustic spectroscopy for non-invasive glucose sensing [31]–[36], demonstrating that almost 100% of the measured glucose values from three volunteers were in Zone A + B of a Clarke Error Grid (CEG) [32]. Despite the advantage of operation in reflectance mode, MIR optoacoustic requires Quantum Cascade Lasers (QCL), which are expensive and large form factor light sources not appropriate for point-of-care diagnostics. Moreover, due to insufficient light penetration because of the high attenuation of MIR radiation by water [29], the method only indirectly estimates glucose concentrations in the interstitial fluid (ISF) or peritoneal fluid, i.e., offering a similar limitation as biochemical sensors. To sum up, after all the efforts up to now, non of the mentioned approaches were able to produce a commercial sensor for non-invasive glucose monitoring.

1.1 Goals and objectives

This dissertation aims to used optoacoustic spectroscopy to detect metabolite *in vivo* and *non-invasively* at the short-wavelength near-infrared (SWIR) regime. This study aims to design a sensor to detect the glucose concentration in the skin's most informative region. Such a capability would help improve the lifestyle of almost 420 million diabetic patients who suffer from a lack of non-invasive, continuous glucose monitoring sensor. The majority of the studies in this particular area have just reported *in-vitro* results. Comparing the approaches presented in this study and previous studies, our approaches made it possible to detect metabolite at higher sensitivity and selectivity *in-vivo* and *in-situ*. This study first involved detecting metabolite (i.e., glucose) from the most informative skin region where we have a higher concentration of that metabolite. To achieve this, an optoacoustic sensor was designed and developed to allow sampling of the epidermal and dermal layers. Consequently, we developed a layer-selective optoacoustic sensing method at the short wave near-infrared (SWIR) regime and interrogated the accuracy of glucose concentration determination for measurements obtained from different skin layers. Layer selection was performed using a machine learning algorithm trained to identify the skin surface and different layers of the skin. Next study involved creating an infrared spectroscopy method that may overcome the boundaries of existing Raman or IR spectroscopy implementations and improve the sensitivity and accuracy attained in detecting solute concentration in aqueous solution. We hypothesized that we might be able to increase the sensitivity of optoacoustic spectroscopy by decreasing water contribution using temperature modulation of the sample being examined. This specific hypothesis relies on the fact that water expansion becomes zero at 4 °C. Therefore, we aimed to remove the substantial contributions from water on the signal collected in the NIR-II window and detect these moieties with higher sensitivity at 4 °C.

1.2 Structure of dissertation and outline

This work is divided into five chapters. Chapter 1 is an overall introduction containing the importance of noninvasive sensors for diabetes and as well as the ultimate goal of the dissertation. Chapter 2 is a description of the principles discussed along with the study, such as optoacoustic spectroscopy and principles. Chapter 3 presents the development of a layer-selective optoacoustic sensor (LSOS) to detect glucose concentration *in vivo* and *noninvasively.* In this chapter, we discuss the experimental setup, measurements, and data analysis procedures. The results obtained from 16 mice are then presented and discussed at the end of the chapter. Chapter 4 presents the development of a cooled IR optoacoustic spectrometer (CIROAS). Next, CIROAS sensors application for *in situ* measurements to detect metabolites such as glucose, lipid, and protein was elaborated. Similar to chapter 3, the development of the sensor, experiment procedures, data analysis, and results are discussed in the same chapter. This chapter also demonstrates measurements from CIROAS showing improved metabolite concentration detection's sensitivity by five times compared to conventional optical and optoacoustic sensors. The general conclusions and outlook are given in chapter 5.

2 Theoretical background

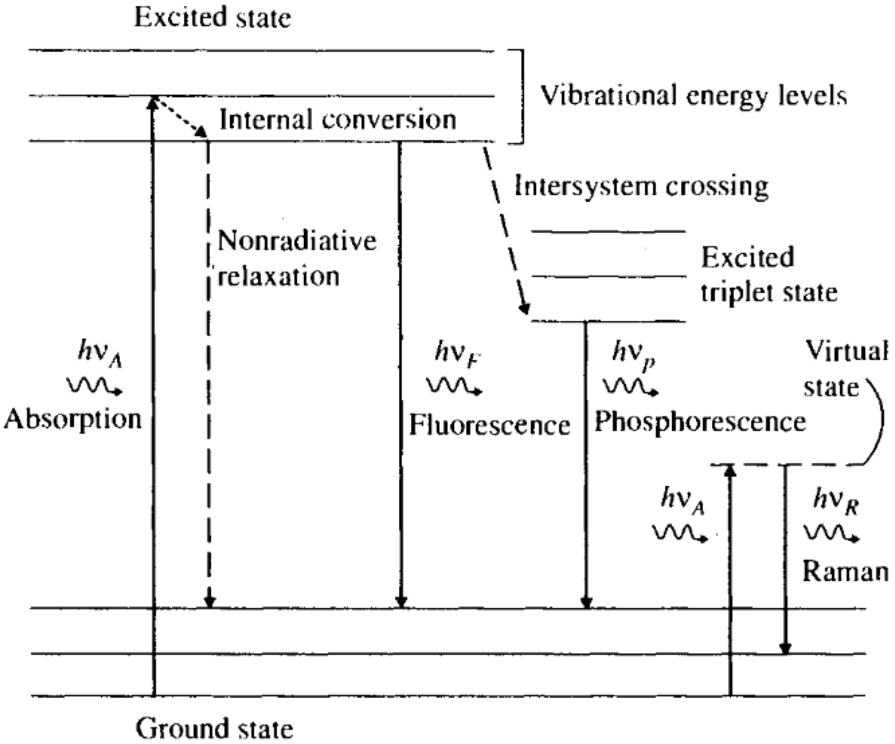
Excited state
Vibrational energy levels
Internal conversion
Intersystem crossing
Nonradiative relaxation
Excited triplet state
$h\nu_A$
Absorption
$h\nu_F$
Fluorescence
$h\nu_p$
Phosphorescence
Virtual state
$h\nu_A$
$h\nu_R$
Raman
Ground state

Figure 2.1 The energy diagram depicts the excitation and relaxation mechanism. $h\nu$ represents the photon energy, and A, F, P, and R denote absorption, fluorescence, phosphorescence, and Raman scattering [37].

Spectroscopic techniques can be applied over a wide spectral range, from X-rays to the terahertz region. Optical spectroscopy is a method originating from the interaction of light with matter. When light interacts with matter, the incident light can be absorbed, scattered, transmitted, and reflected. Depending on the molecule's spatial configuration, the absorbed photon can excite electrons to different energy levels, leading to other molecular states, i.e., electronic, vibrational, or rotational states (Figure 2.1). The absorbed photon energy will then be released after a stipulated time defined by excitation state lifetime through different mechanisms such as energy transfer, luminescence, photochemistry, thermal relaxation. The timespan and proportion of the reemitted light after traversing the biological vortex carries information about the matter's intrinsic property and is used for diagnosis and characterization.

2.1 Optical techniques to detect glucose

Improvements in glucose sensing can have a direct impact on diabetes healthcare. Optical techniques are particularly attractive because they work in real-time, apply non-ionizing radiation, and do not require specific reagents. Different optical methods have been considered for achieving non-invasive glucose measurement. The main premise of these sensors is to illuminate light onto a tissue and detect a photon property that changes in response to different physiological glucose concentration.

2.1.1 Near-infrared Spectroscopy

Significant research attention has been given to near-infrared spectroscopy (NIRS) due to the readily available inexpensive detectors. NIRS, particularly in the spectral region of 700 – 2500 nm [15]–[17], whereby glucose presents several overtones and combinations of the fundamental vibration due to the hydrogen vibration (CH, NH, OH); also called the fingerprint region [15]. Light can probe signals from the stratum corneum and epidermis in this spectral region and is preferentially attenuated at specific wavelength bands as dictated by the absorption spectrum of the different molecules [17]. Despite the original promise and achieving prediction error of 35.6 mg/dl [38], and 27.2 mg/dl [18] in-vivo (by calculating the root mean square error between predicted glucose values and gold standard glucose concentrations), the photon scatter, and the varying optical properties of different tissues imparted significant variations in the NIRS signals, leading to insufficient accuracy and sensitivity for sensing glucose molecules [19], [20].

2.1.2 Mid-Infrared Spectroscopy

Mid-infrared (MIR) spectral region is also considered for non-invasive glucose monitoring in the range of 4,000-1000 cm^{-1} (2500-10000 nm). The advantage of using MIR over other spectral regions like NIR is that glucose absorption is defined by fundamental vibrations (rather than overtones) at 3000, 1400, 1200, and 1000 cm^{-1}. Fourier transform infrared (FTIR) spectrometer or quantum cascade lasers are mostly used as light sources in this spectral region. Several research groups worked on MIR spectroscopy for continuous monitoring *in-vivo* [21]–[25] and achieved a measurement error of less than 20%, R^2 of 0.75. However, low penetration (only a few micrometer) in the skin, highly dependability to water content, expensive and weak light sources made MIR spectroscopy less interesting for non-invasive glucose measurements.

2.1.3 Raman Spectroscopy

Raman spectroscopy is another optical approach used in glucose detection. Raman spectroscopy is based on inelastic scattering of monochromatic light, in which the information is acquired according to the frequency shift of the light after interaction with the tissue, called the Raman effect [26]. Other advances have been achieved with variations such as surface-enhanced Raman Spectroscopy [39]. Raman Spectroscopy was partially successful and predicted the glucose concentration with an error (root mean square error) of approximately 27-36 mg/dl [40] and R^2 of 0.8 [41] on average. However, the Raman technique has a fundamental challenge due to its weaker signal than the fluorescence signal, which covers the Raman scattering signal by interfering with the fluorescence signal [27]. Additionally, a long acquisition time is required to compensate for low SNR.

2.1.4 Fluorescence spectroscopy

There were also other attempts to detect glucose using fluorescence techniques. In the notable advance, an exogenous fluorophore is introduced to the body to tag with glucose molecules. When excited with light, the tagged fluorophores will emit a fluorescence signal, with the detected fluorescence signal's intensity proportional to the concentration of glucose [42]. The technique achieved an average relative error (ARE) of about 11-13%. However, this fluorescence scheme has several challenges, like using different fluorophores makes the technique minimally invasive rather than non-invasive and can lead to toxicity issues at higher wavelength excitations. These probes require complete pharmacokinetic analysis to establish the safety standards as are necessary for human use. Further, for minimally or non-invasive measurements, fluorescence spectroscopy needs calibration against fingerstick measurements. The gradual loss of fluorophores due to photobleaching leads to a drift in the fluorescence signal. Lastly, the nonlinearity of the fluorescence signal over the physiological range of glucose concentrations poses accurate quantitation issues [29].

2.1.5 Optical coherent tomography (OCT)

Optical coherent tomography (OCT) was used to detect glucose noninvasively [43]. The changes in the scattering coefficient and concomitant variations in the interferogram is used to determine the glucose concentration. *In-vivo* measurements based on OCT showed an ARD of 11.5% [28]. However, OCT is known to be highly sensitive to motion artifacts and variations in the local environment, such as skin temperature, pH, and humidity. The measured scattering coefficient is relatively small, which is the major challenge in OCT, and the scattering coefficient can also be affected by the variation in other physiological compounds [29].

2.1.6 Optoacoustic Spectroscopy

A wide range of analytical approaches is under investigation to detect metabolites non-invasively. However, as discussed in chapter 1, optoacoustic spectroscopy (OAS) has shown promise for non-invasive glucose monitoring [31]. In optoacoustic spectroscopy, nonionizing relaxation (non-radiative decay) mechanisms drive a dominant photothermal phenomenon following the excitation of photon propagation through matter. The deposited energy elevates the excited volume's temperature depending on the matter's intrinsic optical and thermodynamic properties along the direction of an illuminating light beam. The increase in the medium's temperature drives secondary effects provoking a thermoelastic expansion in the heated volume of matter; this thermoelastic expansion in the medium generates an acoustic wave due to a rise in the medium's mechanical pressure. The generated acoustic wave propagates through the medium (generated by a phenomenon called optoacoustic effect) and is then sensed by piezoelectric sensors or microphones directly in-contact with the sample or through the coupling medium. An indirect form of optoacoustic effect can also be employed in a way that modulated heat in the excited volume could generate an acoustic wave with a frequency equal to the modulation of the light source in the so-called frequency domain optoacoustic effect. The frequency range of the modulating source can now be swept over the desired frequency range. When coupled with a source in nonionizing spectral range (e.g., IR region), optoacoustic is a non-invasive and volumetric modality capable of *in-vivo* measurement of optical absorbers at that the wavelength ranges used during illumination.

Even though Alexander Graham Bell discovered the optoacoustic effect in 1881 [44], it was not until 1978 that the optoacoustic effect was used for biomedical purposes. Theodore Bowen offered the usage of high energy pulses of microwave radiation for bone imaging [45]. Modulated continuous-wave or pulsed excitation can be used to produce optoacoustic waves. In contrast to pure optical spectroscopy techniques like transmission FTIR spectroscopy, optoacoustic spectroscopy does not require the light to cross the entire path to reach the detector. Instead, the light can penetrate as deep as it can in the tissue and consequently generate acoustic waves, which can be measured from opaque samples at depths previously not attainable by purely optical technics. Combining both optical absorption contrast and high ultrasound resolution, OAS is insensitive to photon scatter and could improve the detection sensitivity over conventional optical methods [30]. The increased resolution is possible because acoustic waves scatter much lesser in biological samples compared to light scattering [46]. Accordingly, acoustic waves can propagate much deeper in the tissue than photons and maintain their initial propagation direction, leading to high resolution and sensitivity at depth.

Furthermore, explicitly speaking, optoacoustic glucose-sensing relies on detecting a change in the tissue interrogated optical property as a function of glucose concentration. Spectroscopic techniques have been proposed in the near-infrared (NIR, 750 – 1300 nm), short-wave infrared (SWIR, 1300 – 2500 nm), or mid-infrared (MIR, 2500 – 10000 nm) [15]–[17] for detecting wavelength-specific changes in the optical absorption due to glucose concentration [47],[18]. However, optical detection of glucose is complicated due to strong background signals from other tissue chromophores. Moreover, due to the strong photon scattering in tissue, optical sensing interrogates bulk tissue measurements, diluting the glucose signal contribution and reducing sensitivity. Besides, the varying optical properties from different skin types and tissues [19], [20] further affect the recorded signal and, consequently, affect the purely optical measurements' accuracy.

2.2 Governing equations of the optoacoustic effect

2.2.1 Initial pressure elevation following the illumination with pulsed laser

The generation of the optoacoustic signal requires stress and thermal confinement criteria to be satisfied [37]. In optoacoustic spectroscopy (OAS), a short nanosecond-pulsed light source is commonly utilized to irradiate the sample, leading to broadband optoacoustic (OA) waves with a frequency content extending from few hundreds of kilohertz to tens of megahertz for acoustic detection. Following absorption of the light, an initial temperature rise triggers a pressure elevation that propagates as an OA wave and is finally detected using a single-element ultrasonic transducer or a transducer array. Thermal relaxation time (τ_{th}) and the stress relaxation time (τ_s) are two critical factors in the generation of OA waves. Thermal relaxation time or, in other words, thermal diffusion (τ_{th}) can be defined as [37],

$$\tau_{th} = \frac{d_c^2}{\alpha_{th}} \tag{2.1}$$

where d_c is the spatial dimension of the heated region (m), and α_{th} is the thermal diffusivity ($\frac{m^2}{s}$). The stress relaxation time of the medium (τ_S) is also given by [37],

$$\tau_S = \frac{d_c}{v_S} \tag{2.2}$$

in which v_S is the speed of sound ($\frac{m^2}{s}$) of the medium. Typically the stress and thermal relaxation times are satisfied while using a nanosecond pulsed laser. Following the laser excitation, the fractional volume expansion of the exciting medium can be written as [37],

$$\frac{dV}{V} = -kp + \beta T \tag{2.3}$$

in which p is pressure rise (Pa), k represents the isothermal compressibility ($\sim 5\,x\,10^{-10} Pa^{-1}$ for water or soft tissue), β is the volume expansion coefficient ($\sim 4\,x\,10^{-4} K^{-1}$), and T is the temperature change (k). Considering short-pulsed illumination of the laser in OA, which is much less than τ_{th} and τ_S, we can neglect fractional volume change ($\frac{dV}{V} = 0$) and write the initial pressure as [37],

$$p_0 = \frac{\beta T}{k} \tag{2.4}$$

where the local temperature defined as,

$$T = \frac{\eta_{th} A_a}{\rho C_v} \tag{2.5}$$

where A_a is specific optical absorption (J/m^3), ρ denotes the density (~ 1000 kg/m^3 for water and soft tissue), C_v denotes heat specific capacity (~ 4000 $J/(kgK)$) and η_{th} is the percentage of absorbed light converted to heat. Using equations (2.4) and (2.5), we can rewrite the initial pressure rise as,

$$p_0 = \Gamma \eta_{th} A_a \tag{2.6}$$

In which Γ is a dimensionless Grüneisen parameter given as,

$$\Gamma = \frac{\beta}{k \rho C_V} \tag{2.7}$$

For a single photon, A_a is proportional to the local optical fluence, and equation (2.6) can be defined as,

$$p_0 = \Gamma \eta_{th} \mu_a F \tag{2.8}$$

where F is fluence (J/cm^2) and μ_a is the absorption coefficient. Usually, Γ and η_{th} are considered to be constants, and the initial pressure elevation is mostly determined by the absorption coefficient (μ_a) and Fluence (F). Accordingly, by knowing Γ, η_{th}, depending on the sample type, and F depending on the energy of the laser pulse, and measuring the p_0 (an acoustic wave generated in the sample with a sample dependent speed of sound), the problem would be to compute the absorption coefficient μ_a.

2.2.1. Optoacoustic wave propagation

The propagation of OA pressure $p(r,t)$ in an inviscid and isotropic medium can be described as [37],

$$\left({v_s}^2 \nabla^2 - \frac{\partial^2}{\partial t^2} \right) p(r,t) = -\frac{\beta}{k} \frac{\partial^2 T(r,t)}{\partial t^2} \tag{2.9}$$

in which p and T are the pressure and temperature rise above the initial value, respectively. In the case of nano-pulsed illumination and thermal confinement, we can neglect heat conduction and write the heat diffusion equation as [37],

$$\rho C_v \frac{\partial T(r,t)}{\partial t} = H(r,t) \tag{2.10}$$

where $H(r,t)$ denotes the thermal energy deposited per unit volume and per unit time and can be further defined as [37],

$$H(r,t) = \eta_{th} \frac{\partial A_e(r,t)}{\partial t} \tag{2.11}$$

By placing equation (2.10) in equation (2.9), we have [37],

$$\left(\nabla^2 - \frac{1}{v_s^2}\frac{\partial^2}{\partial t^2}\right)p(r,t) = -\frac{\beta}{C_P}\frac{\partial H(r,t)}{\partial t} \tag{2.12}$$

where C_P denotes specific heat capacity at constant pressure. Considering finite heating pulse duration and solving equation (2.13) using Green's function, one obtains[37], [48],

$$p(r,t) = \frac{\beta}{k v_{s^2}}\int_{-\infty}^{t^+} dt' \int_v \; dr' G(r,t;r',t')\frac{\partial^2 T(r',t')}{\partial t'^2} \tag{2.13}$$

here G is Green's function and is defined as,

$$G(r,t;r',t') = \frac{\partial(r-r',t-t')}{4\pi|r-r'|} \tag{2.14}$$

which is interpreted as a point source emitting a spherical wave. Consequently, for $t' = t - \frac{|r-r'|}{v_s}$, equation (2.14) can be rewritten as [37],

$$p(r,t) = \frac{\beta}{4\pi k v_s^2}\int_v \; dr' \frac{1}{|r-r'|}\frac{\partial^2 T(r',t-\frac{|r-r'|}{v_s})}{\partial t'^2} \tag{2.15}$$

This is the forward solution of the optoacoustic wave equation and describes the pressure wave propagation as a function of temperature. As an example of a simplified case of the pressure rise by an absorber, the wave propagation by a spherical point-like absorber can be described by applying a spherical absorber of radius R in equation (2.16) [37],

$$p(r,t) = \frac{r+v_s t}{2r}p_0(r+v_s t) + \frac{r-v_s t}{2r}p_0(-r+v_s t) + \frac{r-v_s t}{2r}p_0(r-v_s t) \tag{2.16}$$

As the pressure rise is radially symmetric, we only take the radial propagation along the r-direction in our computations. Figure 2.2 shows the optoacoustic signals of three spherical absorbers having a diameter of 10, 50, and 100 µm, respectively. As depicted, a smaller sphere absorbs less energy and generates shorter and weaker optoacoustic signals. The main lobe of the frequency spectrum of spherical absorbers is symmetric around their central frequency (see Figure 2.2). Accordingly, the smaller the sphere, the shorter is the generated pulse, which increases the generated central frequency and the frequency bandwidth.

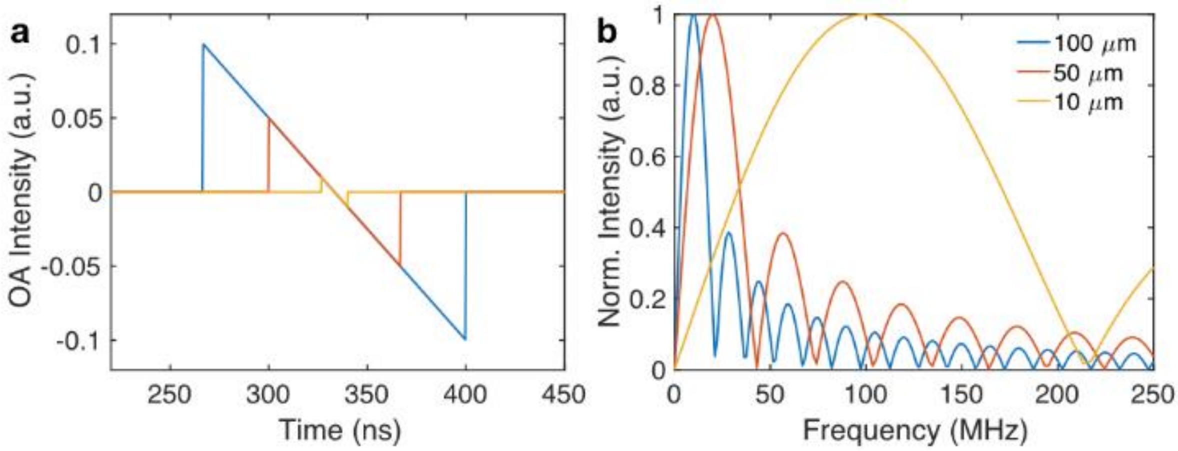

Figure 2.2 Simulated OA signal generated by spherical absorber with different diameters measured at 500 µm from a sphere and using equation (2.16). a) Time-domain signals, b) Frequency-domain signals [37], [49].

2.2.3. Sound propagation in a biological sample

Optoacoustic spectroscopy's primary advantage over purely optical spectroscopy is the weak acoustic scattering compared to light scattering. The acoustic scattering is weaker by 2-3 orders of magnitude [50]. Accordingly, the speed of the sound is a vital criterion to define acoustic wave propagation. On average, 80% of all biological samples consist of water, and it is reasonable to assume the speed of sound in the water (~ 1500 m/s) as an approximate speed in many biological samples. However, in general speed of sound is defined as [51],

$$v_s = \sqrt{\frac{1}{\rho k}} \tag{2.17}$$

where ρ is the density of the tissue, and k is the compressibility coefficient [51].

Acoustic impedance is another criterion, which defines the amount of reflection, or transmission when sound propagates from one medium to another medium and can be defined as [52],

$$Z = \rho v_s \tag{2.18}$$

Using acoustic impedance differences between two medium, the reflection (R) and transmission (T) coefficients can also be defined as [52],

$$R = \left(\frac{Z_2 - Z_1}{Z_2 + Z_1}\right)^2, \qquad T = \frac{4Z_2Z_1}{(Z_2 + Z_1)^2}, \tag{2.19}$$

Equation. (2.19)shows that small differences in the impedance of two mediums lead to high acoustic transmission, and in contrast, large differences lead to higher acoustic reflection. Thus, these differences in different medium impedances are used as a contrast mechanism in acoustic spectroscopy and imaging. Analogously, refraction between layers with different acoustic impedances can be defined using Snell’s law [51],

$$\frac{sin(\theta_1)}{sin(\theta_2)} = \frac{v_{s_1}}{v_{s_2}} = n, \tag{2.20}$$

where $\theta_1$and θ_2 are the angle of incidence and the angle of refraction with respect to the perpendicular axis of reference. n is typically equal to 1 for most biological tissues, and acoustic refraction can be neglected for optoacoustic spectroscopy.

2.2.4. Optoacoustic signal attenuation

Optoacoustic pressure wave attenuation as a function of depth *r*, can be written as [53],

$$p(r) = p_0 e^{\alpha(f)r} \tag{2.21}$$

where $\alpha(f) = |\alpha_0| f^m$, and depends on frequency dependant attenuation coefficient f and empirically determined exponent for the medium m. Generally, for biological tissue m is equal to one ($m \approx 1$) and the frequency dependency is a linear relation and can be written as [53],

$$\alpha_0 = 0.5\ dBMHz^{-1}cm^{-1} \tag{2.22}$$

However, in the case of water m is equal to 2 ($m \approx 2$), and the dependency is a quadratic relation given by [53],

$$\alpha_0 = 0.00217\ dBMHz^{-2}cm^{-1} \tag{2.23}$$

Accordingly, in biological samples, OA signals at a frequency of 15 MHz propagation through 1 cm of biological tissue are attenuated by 7.5 dB. This frequency is typically chosen as the central frequency of our ultrasound transducers used in this dissertation.

2.3. Ultrasound Detectors

Ultrasound detectors play an essential role in optoacoustic spectroscopy, as this is how optoacoustic signals are detected. In principle, any system that changes its state in response to mechanical stress could be used as a detector. Based on the mechanism and the detection technique, commonly transducers can be classified as; piezoelectric transducers, capacitive micro-machined ultrasound transducers, optical interferometry based transducers, and optical deflection transducers. However, as piezoelectric transducers are the most common detectors in optoacoustic spectroscopy (due to high detection sensitivity) [54] and used in this study, we only discuss piezoelectric transducers in this section.

Detectors based on piezoelectricity are most commonly used due to the abundance of piezoelectric materials in nature and ease of manufacturing. Furthermore, these detectors could be formed in almost any shape, which allows them to be suitable for different optoacoustic spectroscopy applications. Piezoelectric transducers are typically built from piezoelectric quartz [55] or poly-crystalline ferroelectric ceramic materials like lead zirconate titanate, known as PZT [54]. The piezoelectric transducers are based on the piezoelectric effect, wherein the mechanical perturbations are converted into an electrical signal and vice-versa. Figure 2.3 shows a typical piezoelectric single-element detector and its main components. Typically, the thickness of the transducer's active elements defines the central frequency and bandwidth of the ultrasonic detection. The backing material used in the transducer suppresses the reflection and back reflection of acoustic waves within the active area, which deteriorates axial resolution due to interference caused by the oscillations.

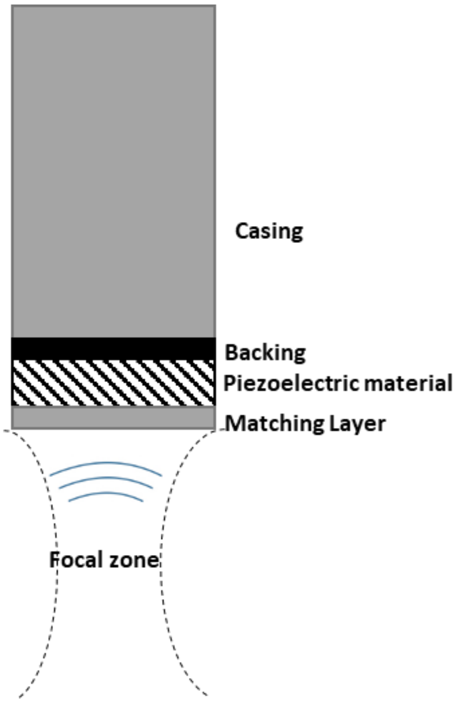

Figure 2.3 Cross-section view of a single element transducer. The main components are; the piezoelectric element, the backing, and matching layers.

Furthermore, the matching layer (i.e., matching acoustic glass, water, or gel) is introduced to achieve better coupling between the transducer material and the probed medium; this layer is used to overcome the mismatch between the detector's impedances and the surrounding medium. Lastly, the shape of the fabricated sensor defines the focusing area of the transducer. Based on the surface’s mechanical shape, the transducers can be classified as spherically focused, cylindrically focused, or unfocused. The transducer's focal zone is defined as the area of the spatial sensitivity field, where sensitivity is not less than -6 dB of the maximum sensitivity.

3 Layer-specific optoacoustic sensor for a non-invasive glucose detection sensitivity of the skin

3.1 Introduction

In this chapter, we sought to develop an optoacoustic spectroscopy (OAS) system capable of layer-specific detection of glucose in the skin. The development of such a device required us to overcome three major challenges. First, we had to develop a methodology that could identify skin layers using the one-dimensional optoacoustic signal detected by a sensor. Second, we had to create a system that can detect characteristic vibrations of glucose while also being insensitive to fluctuations of the illumination beam. Third, we had to identify the optimal spectral range for glucose detection by OAS.

We developed an optoacoustic device powered by a machine-learning algorithm to address the challenge of layer identification. This algorithm could use the sensor's raw data to selectively provide glucose concentration changes from different skin layers. To improve the SNR over conventional optoacoustic sensors, we developed a dual optical path design; one path was directed to the sample, and the second served as a reference to independently measure the fluctuations in light intensity fluctuations. The dual optical path design was used to perform sensor measurements in 16 mice over 36 wavelengths covering the range 1450-1800nm. We present the methodology and results herein.

3.2 Method

We developed a dual-path spectroscopic system (Figure 3.1) and evaluated its use as a glucose sensor. The system was built as a generalizable sensor and the studies that follow examined specific operational parameters that maximize sensitivity and eventually lead to a more portable setup.

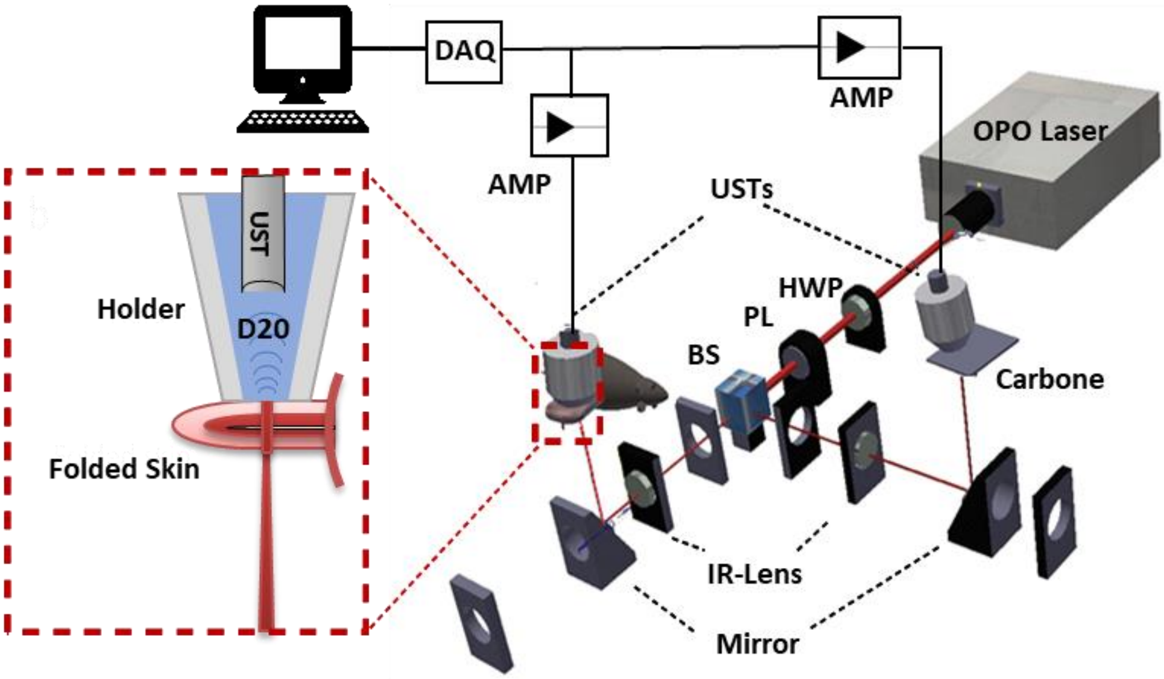

Figure 3.1 Schematic representation of LSOS; UST– ultrasound transducer; BS – beam splitter; AMP – Amplifier; DAQ – data acquisition card; L – lenses, PL – Polarizer, HWP – Half waveplate. The inset figure shows the skin's placement from the back of a mouse under the UST holder.

3.2.1 Experimental Setup

The optical beam was split into two, using a broadband beam splitter (BS; BSW23, Thorlabs) to simultaneously measure two optoacoustic signals, one from the sample and the other from an optoacoustic reference. The two OA signals were recorded to perform real-time correction of the laser emission profile of the laser source at different wavelengths and perform pulse-to-pulse correction to remove laser beam fluctuation and instability. To interrogate the optimal wavelengths to improve sensitivity during glucose sensing, we employed illumination from a tunable nanosecond OPO laser (SpitLight Single, Innolas, Krailling Germany) controlled by a personal computer (PC).

The reference path shins the beam onto a thin carbon layer, which is acoustically coupled via heavy water to a spherically focused ultrasound transducer (UST) with a central frequency of 15 MHz and a focal distance of 20 mm. The sample path shins the beam onto the sample, which was acoustically coupled to an identical UST. The USTs were placed inside the coupling chambers containing 400 ml of heavy water to keep USTs in focus. The chambers were covered with thin plastic transparent foils. Acquired signals from both arms were amplified using two low-noise amplifiers (AMP; AU-1291, Miteq Inc., USA), then digitized using a fast data acquisition card (DAQ) operating at 200 MS/s. In this setup, the illumination beam had a near-Gaussian profile with a spot size of approximately < 1 mm in diameter and was focused on the sample using achromatic lenses with a 10 cm focal length (N-BK7, Thorlabs). The laser repetition rate in all the experiments was 50 Hz, and the pulse width was ~7 ns.

The energy per pulse spectrum of the tunable OPO laser is not constant for different wavelengths. Accordingly, various pulse energy levels at different wavelengths might lead to inaccuracies in the spectrum morphology. More importantly, to avoid saturation in OA signal acquisition, we need to decrease the laser pulse energy using different filters to prevent saturation at wavelengths with higher pulse energy. However, on the other hand, the sensitivity and signal to noise ratio at wavelengths with low pulse energy will decrease. Therefore, we used a combination of a half-wave plate (HWP) and a polarizer to set the laser's power at constant output energy, as in the previous studies [49], [56], [57]. The HWP was rotated using a motorized stage (PRM1Z8, Thorlabs, Germany), from 0 to 90 degrees in 5 ° steps, changing the beam's polarization. The polarizer then controls the output energy by allowing only parallel light to pass through. This makes the amount of parallel polarization a function of HWP rotation. A lookup table was created by measuring the laser energy at the entire wavelength range used and rotational angles using a powermeter (Vega, Ophir, Israel). The lookup table was built at the beginning of the experiment for all measured wavelengths (row of the lookup table) as a function of the half-wave plate rotation angle (columns in the lookup table). The resolution for the wavelengths (400-720 nm, 875-2200 nm) and rotational angles are 10 nm and 5°, respectively. The fitted lookup table enables us to find the rotational angle of the HWP to produce the desired power at all wavelengths. In this study, pulse energy of 0.2 mJ was fixed as an output energy per pulse of the beam. Figure 3.2a shows that the pulse energies at five typical wavelengths have different values with a mean value of 0.38 and a standard deviation (SD) of 0.12 (Figure 3.2a). However, after performing the lookup table and setting the output pulse energy to 0.2 mJ, the output energy is set in our desired pulse energy with a mean of 0.198 mJ and a standard deviation of only 0.01.

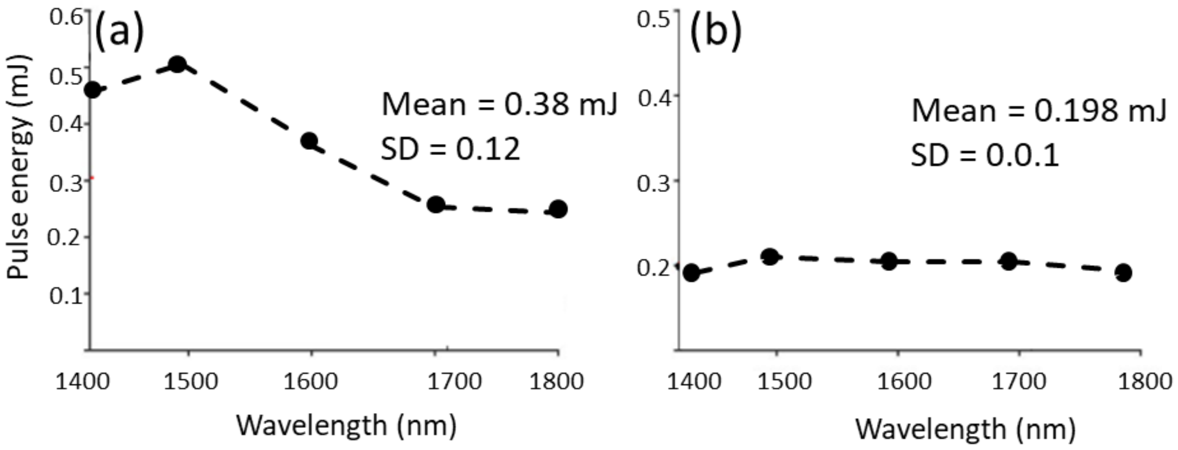

Figure 3.2 Pulse energy spectrum of the OPO laser at five wavelengths. a) Pulse energy without applying HWP and polarizer to control the pulse energy, b) pulse energy using a combination of HWP and polarizer, and setting the output pulse energy at 0.2 mJ at all wavelengths.

3.2.2 Data analysis – Algorithm

Figure 3.3 depicts the LSOS algorithm for *in vivo* absorption spectra measurements. Above all, the raw optoacoustic signal was first acquired continuously from dual-paths: reference and sample paths collecting OA signal in the range 1450-1800 nm with 10 nm step sizes (number 1 in Figure 3.3). The collected OA signals at the sample path were sorted into four classes corresponding to the dermis, hypodermis, muscle layers, and bulk skin (number 2 in Figure 3.3). Then, the OA intensities were calculated by estimating the area under the curve of Hilbert transformation of the acquired OA raw signals at different wavelengths (number 3 in Figure 3.3). However, just like previous studies, the OA signal intensity in the bulk skin analysis was calculated by getting the OA raw signals peak-to-peak value at different wavelengths. The fourth step was to perform pulse-to-pulse correction of the OA raw signals by dividing the OA signal corresponding to different skin layers with the OA raw signal at the reference arm to remove the laser fluctuation and noise (number 4 in Figure 3.3). As the next step, the output after the pulse-to-pulse correction was subtracted and then divided by the OA intensity at the reference wavelength of 1710 nm (number 5 in Figure 3.3). Leave one out cross-validation (LOOC) was finally applied to predict glucose concentration levels from the acquired OA intensity (number 6 in Figure 3.3).

On the other hand, invasive measurement using a glucometer was obtained from the mice's tail every 4-5 minutes (number 7 in Figure 3.3). For better comparison, the invasive data was interpolated to find the corresponding glucometer reference value (invasive measurement) when OA measurement was done at different wavelengths (number 8 in Figure 3.3). Finally, the output from both invasive and non-invasive measurements was then smoothed and then compared to find the most informative skin layer and the wavelength to sense glucose.

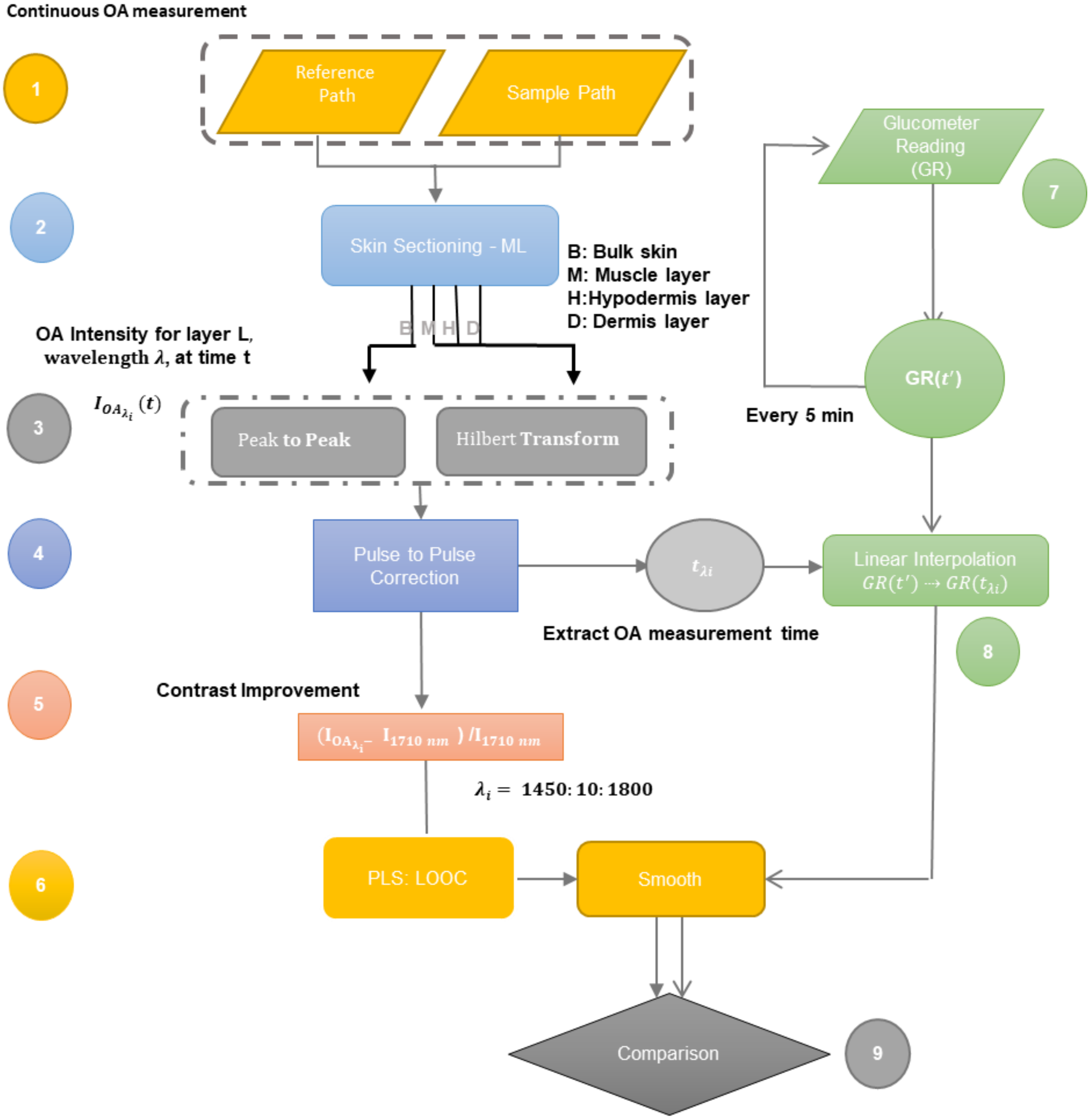
Continuous OA measurement
1
Reference Path
Sample Path
2
Skin Sectioning - ML
B: Bulk skin
M: Muscle layer
H:Hypodermis layer
D: Dermis layer
B M H D
OA Intensity for layer L, wavelength λ, at time t
3
$I_{OA_{\lambda_i}}(t)$
Peak to Peak
Hilbert Transform
4
Pulse to Pulse Correction
$t_{\lambda i}$
Extract OA measurement time
5
Contrast Improvement
$(I_{OA_{\lambda_i}} - I_{1710\ nm})/I_{1710\ nm}$
$\lambda_i = 1450{:}10{:}1800$
6
PLS: LOOC
Smooth
Comparison
9
Glucometer Reading (GR)
7
$GR(t')$
Every 5 min
Linear Interpolation $GR(t') \rightarrow GR(t_{\lambda i})$
8

Figure 3.3 LSOS Algorithm for in vivo measurements: 1) collecting OA signals in dual-path in the range 1450-1800 nm, 2) skin sectioning, 3) OA Intensity calculation, 4) Pulse-to-pulse correction, 5) glucose signal's contrast improvement, 6) LOOC, 7) invasive measurement every 5 minutes using a glucometer (to have one invasive measurement for each cycle of OA measurements from 1450-1800 nm), 8) interpolation to find corresponding reference value (invasive measurement) at the time OA measurement was done, 9) comparison of invasive and non-invasive results.

3.2.2.1 Signal to noise improvement - Pulse-to-Pulse correction.

The scanning was performed continuously between 1450 nm to 1800 nm with a 10 nm step size. One hundred measurements at each wavelength were recorded simultaneously at the two measurement arms (Figure 3.1). The OA intensity (OAI) for skin sublayers were measured by transforming OA raw data, using Hilbert transformation, and integrating the area of interest under the envelope as follows [57], [58];

$$OAI = \int_{s_l} H(OA)(t)\, dt \tag{3.1}$$

where $H(OA)$ is the Hilbert transform at assigned segments of the OA raw signal s_l (skin layer) and was performed using a signal processing toolbox in MATLAB 9.1.0.441655 (R2016b).

Measurements obtained from the reference arm were employed to perform real-time pulse-to-pulse correction to remove laser beam fluctuations (at different wavelengths) and improve the signal-to-noise ratio (SNR) of the optoacoustic measurements from the sample. SNR is defined as a linear ratio of the average to a standard deviation of one hundred collected OA intensities. The final corrected OA signal was the average of one hundred normalized measurements at each wavelength using the following equation:

$$I_{OA} = Mean\left(\frac{[I_{SA}]_{1X100}}{[I_{RA}]_{1X100}}\right) \tag{3.2}$$

where I_{OA} is the corrected signal, $[I_{SA}]_{1X100}$ is the vector of 100 measured OA intensities at each wavelength in the sample path, and $[I_{RA}]_{1X100}$ is the vector of 100 measured intensities at each wavelength in the reference path. We repeated this procedure for each wavelength. One complete measurement cycle, in which all wavelengths from 1450 to 1800 nm were scanned in 10-nm steps, took about 3 minutes.

Figure 3.4 depicts the SNR improvements in distilled water before and after pulse-to-pulse correction. SNR improvements at water spectral signature (i.e., peaks at 1440 and 1920 nm) were between 30 and 80. Figure 3.4 inset shows a plot of fifty consecutive OA intensities of distilled water at 1920 nm before and after the pulse-to-pulse correction. The deviations of these intensities decreased significantly after point-to-point correction, which led to higher SNR and sensitivity.

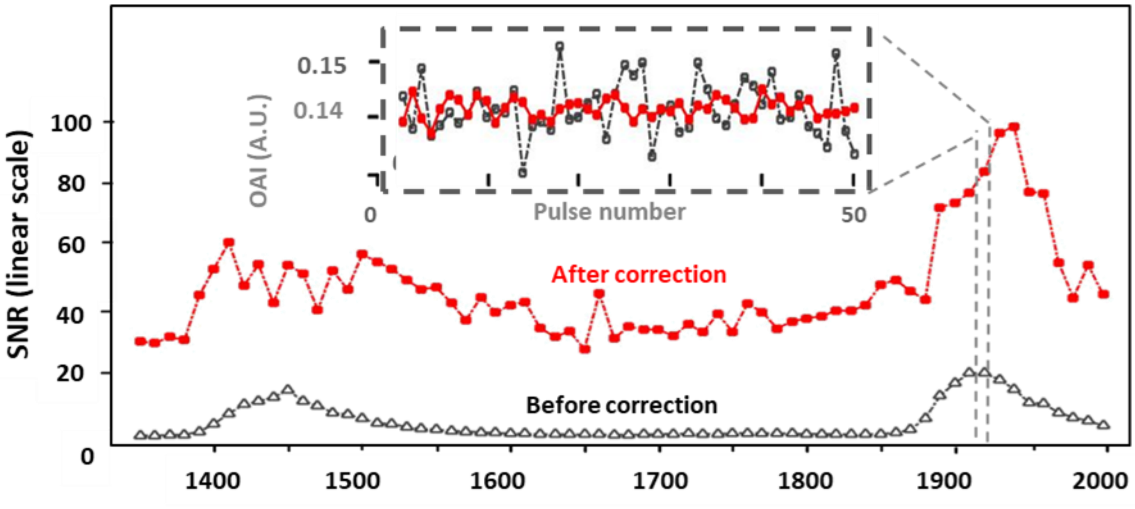

Figure 3.4 LSOS system characterization; fifty pulses were measured at each wavelength, with the final OA intensity value being the mean of the fifty measurements. The figure exhibits the SNR improvement of water spectra in the range of 1350 - 2000 nm before (black) and after (red) performing pulse-to-pulse correction, and the inset figure depicts fifty measured pulses at 1920 nm before (black) and after (red) performing pulse-to-pulse correction.

3.2.2.2 Data analysis – Machine Learning for layer separation

A key feature of the method presented is the depth-dependent observation of biochemical parameters in tissue. Accurate separation of the skin layers with one-dimensional signals represents a unique challenge. To allow depth-dependent observation of glucose throughout the skin, we developed a machine-learning algorithm that could accurately segment one-dimensional acoustic signals according to skin layers.

First, we sought to segment the 1D OA signal into the corresponding skin layers using a machine learning (ML) algorithm (Figure 3.5). Figure 3.5b shows OA raw signals as a function of time and depth, acquired in vivo from the skin shown in Figure 3.5a. Different colors correspond to different wavelengths (1450 – 1800 nm), whereby the time (and depth) dimension corresponds to the distance that the ultrasound signal traveled into the skin fold, i.e., depth.

A ML algorithm based on bagged ensemble trees [59] was selected to partition the time-series of each OA raw signal into three shorter time-series corresponding to three different skin layers: (1) the dermis (including the epidermis), (2) the hypodermis, and (3) the muscle layers (including the fascia). The input of the ML algorithm comprised 340-500 spectra per mouse, which were generated by a moving average with a time window of 0.23 µs (corresponding to a thickness of 345 µm), moved in steps of 0.01 µs (15 µm), over the entire OA signal with an overall time window of ~1.65 µs (~ 2.5mm). For each step, the moving time window computes a spectrum comprising 36 different wavelengths (1450-1800 nm in steps of 10 nm). The intensity of each point of the spectrum is the average intensity of the optoacoustic signal over the 0.23 µs window at the corresponding wavelength. For training the machine learning algorithm, we selected 30 spectra, produced by the moving window. Each spectrum corresponding to the depth of each layer, as seen on the histology images (see Figure 3.5a & Figure 3.8), was assigned to belong to this layer. Figure 3.5c shows a sample output of the trained ML algorithm for the spectra computed for one mouse. The algorithm assigns a “layer” score for each spectrum. When these spectra are plotted sequentially for each step of the moving window, along the axis termed moving window index, the change of layer becomes evident by the different score assigned.

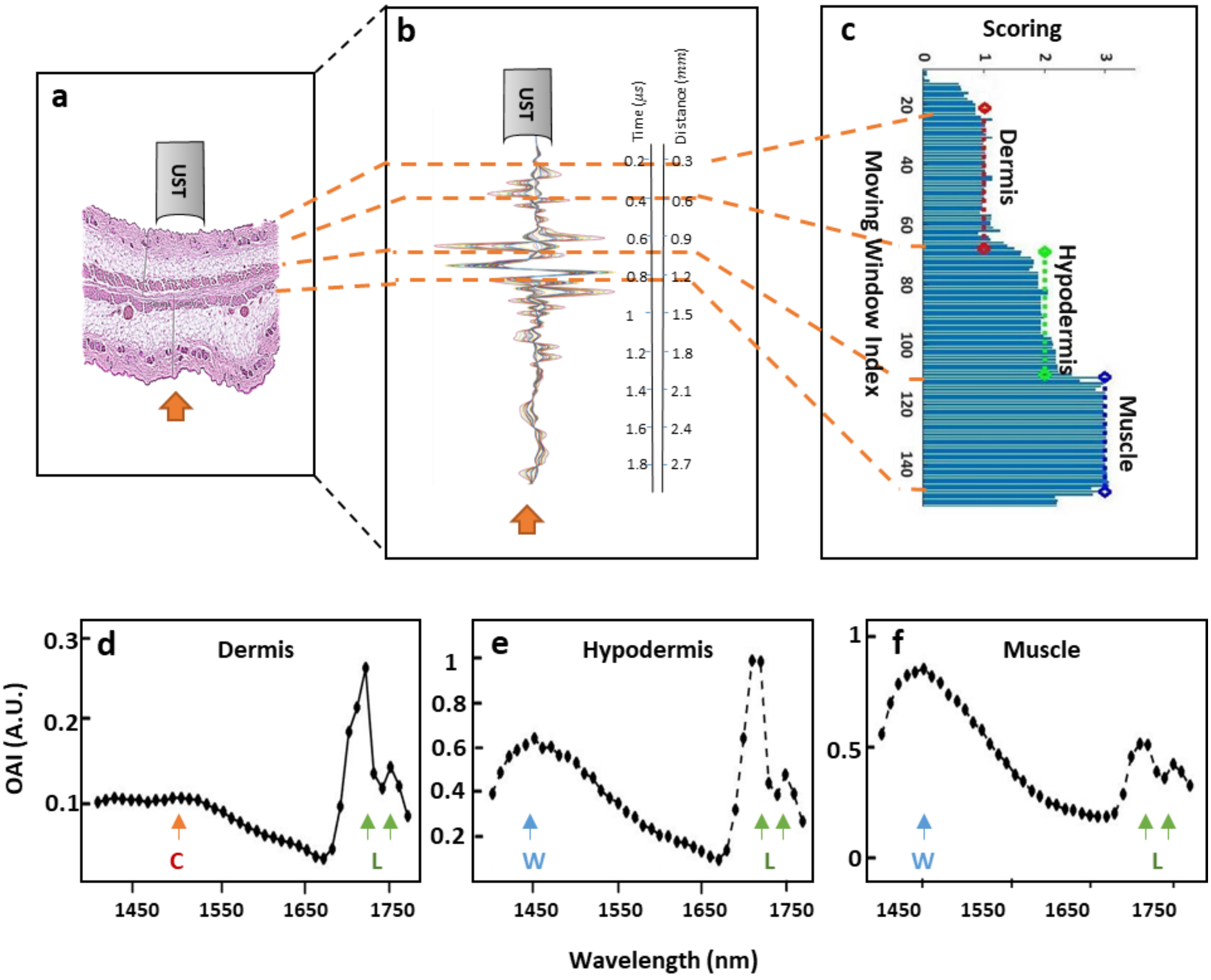

Figure 3.5 Sectioning of the OA signal according to skin sectioning using a ML algorithm. A window of ~130 ns in length was moved with ~10 ns step sizes along an acquired OA raw signal at all measured wavelengths, producing spectra using a Hilbert transformation and integral of the signal in the window. These spectra were sorted into three classes corresponding to the dermis, hypodermis, and muscle layers of the skin. a) Histology of the folded skin, b) a sample of a raw OA signal of a section of mouse skin. Each colored line corresponds to a different excitation wavelength. The dotted red lines delineate the skin layers estimated borders, c) classification of spectra corresponding to each time window movement into three skin layers using ML. d-f) Absorption spectra and characteristic absorption of collagen (C), lipid (L), and water (W) from the areas of the OA signal assigned to each skin layer by the ML algorithm as follows: d) the dermis (including the epidermis), e) the hypodermis, and f) the muscle (including fascia).

To further validate the ML algorithm’s output, we visually examined spectra that were assigned different scores. Figure 3.5d-f shows three representative spectra, each of a score that assigned them to the dermis, hypodermis, and muscle layers. The spectrum in Figure 3.5 has peaks at 1500, 1720, and 1750 nm, characteristic of collagen and lipids found in the dermis. Conversely, Figure 3.5e shows a 3-fold higher absorption at 1720 and 1750 nm, compared to the spectrum in Figure 3.5d, which corresponds to increased lipid concentration, consistent with the composition of the hypodermis. The spectrum in Figure 3.5f depicts absorption peaks at 1450, 1720, and 1750 nm, characteristic of water and lipids, typical of the muscle layer and fascia.

Collectively, the average calculated thicknesses for the dermis, hypodermis, and muscle layers in all measurements performed were approximately 200, 260, and 160 μm, respectively. These observations regarding both the content and thickness of the individual skin layers agree with the histology observations of the skins measured (Figure 3.8a, b) and to published figures from other studies [60]–[62]. Data analysis – glucose signal contrast improvement

3.2.2.3 Data analysis – glucose signal’s contrast improvement

The optoacoustic signal is a function of both irradiated laser beam intensity and the acoustic resonance condition, as shown in the following equation:

$$I'_{OA} \propto F\alpha I_B \tag{3.3}$$

where I'_{OA} is the OA intensity, α is the optical absorbance, I_B is the laser beam's intensity, and F is the Grüneisen parameter and related to the acoustic resonance mode due to pressure elevation following the temperature change after illumination of the biological sample. As we will discuss later, OA measurement's sensitivity can be influenced by the change in temperature. In the case of glucose sensing, a 1℃ difference in the temperature is comparable with the concentration change of glucose in the physiological range [63]. To overcome the instability caused by the change of acoustic resonance characteristics, we use the referenced wavelength technique (or dual-wavelength technique), in which equation (3.4) is used to choose the optimum acoustic resonance as previously suggested [63];

$$I_{OA_\lambda} = \frac{I'_{OA_\lambda} - I_{OA_{1710nm}}}{I_{OA_{1710nm}}} \tag{3.4}$$

Where I'_{OA_λ} is the optoacoustic intensity in the wavelength range of 1450-1800 nm after pulse-to-pulse correction, and $I_{OA_{1710nm}}$ is the OA intensity at 1710 nm. The technique is a two-step equation, (i) deferential step; the OA intensities are subtracted by the intensity of a reference wavelength (i.e., 1710 nm) to remove the influence of background noise due to change in the concentration of metabolites such as water, lipid, proteins in the skin, (ii) normalizing step: the differential signals from the first step is normalized to the same reference wavelength (i.e., 1710 nm) to eliminate the change in resonance mode due to interference such as temperature. In our case, 1710 nm was chosen as a reference wavelength. The wavelength has the least absorption to sense the glucose signal (Figure 3.6) *in-vitro*. Besides, 1710 nm is the wavelength where lipid has a featured absorption, and water shows comparable absorption to glucose [64]. To prove the effectiveness of 1710 nm wavelength for removing the background noise and acoustic resonance change in *in-vivo* mice experiments, all other measured spectral region wavelengths were also tested as the reference wavelength in equation (3.4). However, none of them was as effective as 1710 nm.

3.2.2.4 Data analysis – Leave one out cross-validation

In this study, the Leave-one-out method was used for rescaling the recorded optoacoustic signal to arrive at the values relative to glucometer measurements. This allows a comparison of OA measurements with glucometer measurements on the Clarke error grid. Clarke grid is an analysis tool widely used in diabetic research to show the technique's performance in estimating glucose value. If the results fall within regions A or B, the approach is considered clinically acceptable [65].

The scaling was performed on OA intensities at each wavelength (N = 12-20, the number of OA measurements for each wavelength at ~ 50 minutes of the experiment). In each case, we use a subset called the training set (with the size of N-1) to calculate the coefficient to fit the data between OA intensities (training set) and corresponding glucometer values (gold standard). The fitting coefficient will then be used to scale the left-out sample to get its estimated glucose concentration. We repeat the process N times, each time leaving out a different pair for rescaling the all OA intensities at each wavelength (with size N) in the mg/dl range.

Unscaled optoacoustic signals were compared to the glucometer readings using cross-correlation. The scales valued were compared using root means square error (RMSEcv).

3.2.3 Comparison of glucose versus water absorption spectra

This section aims to understand the true spectrum of glucose compared to water, which is the strongest absorption agent in the blood that impedes other molecules' detection. We expect a similar glucose spectrum in the *in-vivo* experimental situation, but not necessarily the same, as the Grüneisen parameter of glucose would not be the same in different mixtures. The pure spectrum of glucose (compared to regular distilled water spectrum) could provide us with a window where glucose is susceptible to strong optical absorption by the water spectrum.

Figure 3.6 shows a comparison of the absorption spectra of distilled water (blue squares) with that of glucose (green squares). The absorption spectra were recorded to determine the best spectral window in the SWIR region for the study. The glucose solution was prepared by dissolving glucose powder in heavy water (D_2O) to a concentration of 2000 mg/dl. Heavy water was chosen as its absorption is almost negligible when compared to regular water. Furthermore, the high concentration of 2000 mg/dl glucose ensures that glucose absorption exceeds heavy water absorption in the SWIR spectral window. The glucose signal was then calculated by subtracting the spectrum of heavy water from the spectrum of heavy water and glucose. The glucose spectrum agrees with previous measurements [57], exhibiting absorption maxima at ~1650 and ~1800 nm. Figure 3.6 shows that the glucose spectrum agrees with previous measurements [57], exhibiting absorption maxima at ~1650. A simple visual inspection of the spectrum shows that the 1550 to 1700 nm spectral region offers an ideal window for glucose detection in the SWIR wavelengths due to the low absorption of water and high absorption of glucose in this spectral range. Therefore, in this study, the spectral region of 1450 to 1800 nm (expanded region of the ideal window) was employed.

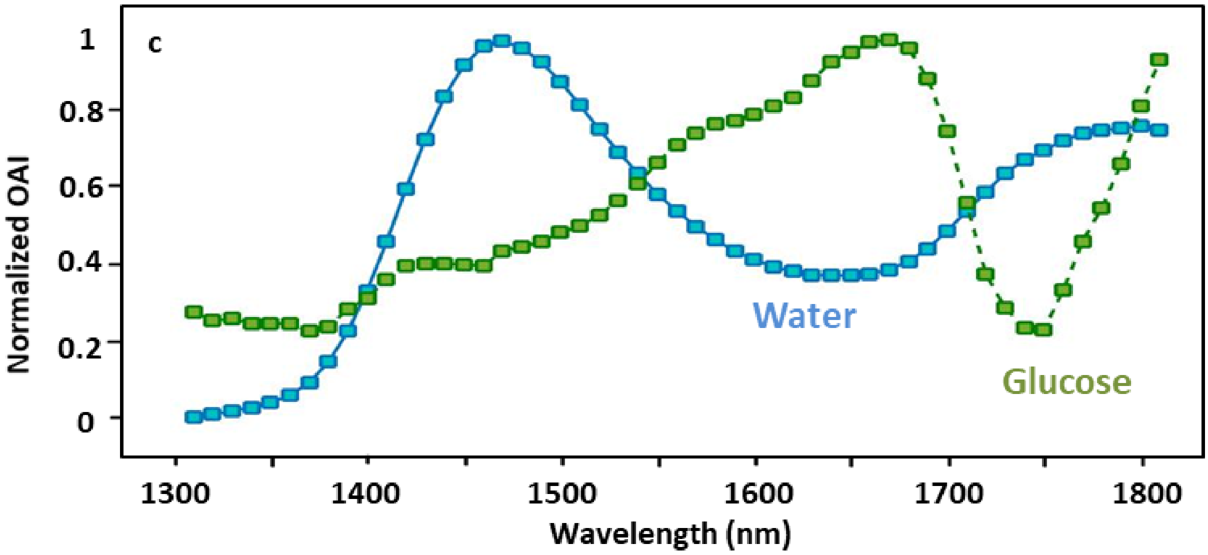

Figure 3.6 Water spectrum versus glucose spectrum; A comparison of the OA intensities (OAI) of glucose that of water (blue squares). The glucose solution was prepared by dissolving glucose powder in heavy water. The glucose signal was calculated by subtracting the heavy water spectrum from the spectrum of the glucose+D2O solution.

3.2.4 In-vivo measurements

Animal procedures were carried out with the approval of the Government of Upper Bavaria. Sample sizes for animal studies were chosen based on institutional recommendations with guidance from the literature. Investigators were not blinded to animal group allocations. The workflow of the animal procedure is shown in Figure 3.7.

Sixteen CD1 adult female mice less than 1-year-old weighing ~40 g were randomly divided into two groups: glucose-injected mice (n = 10) were injected intraperitoneally with glucose (20%, B.Braun, Germany), such that each animal received 2 mg per gram of body weight; and control mice (n=6) were intraperitoneally injected with phosphate-buffered saline (PBS). Before acquiring optoacoustic measurements, animals were fasted overnight (~ 16 h), and skin hair was removed to avoid hair interference with optoacoustic measurements. Glucose testing and OA measurements were performed for 50 minutes duration. Blood sampling via tail was done by cutting the tail tip up to 1 mm.

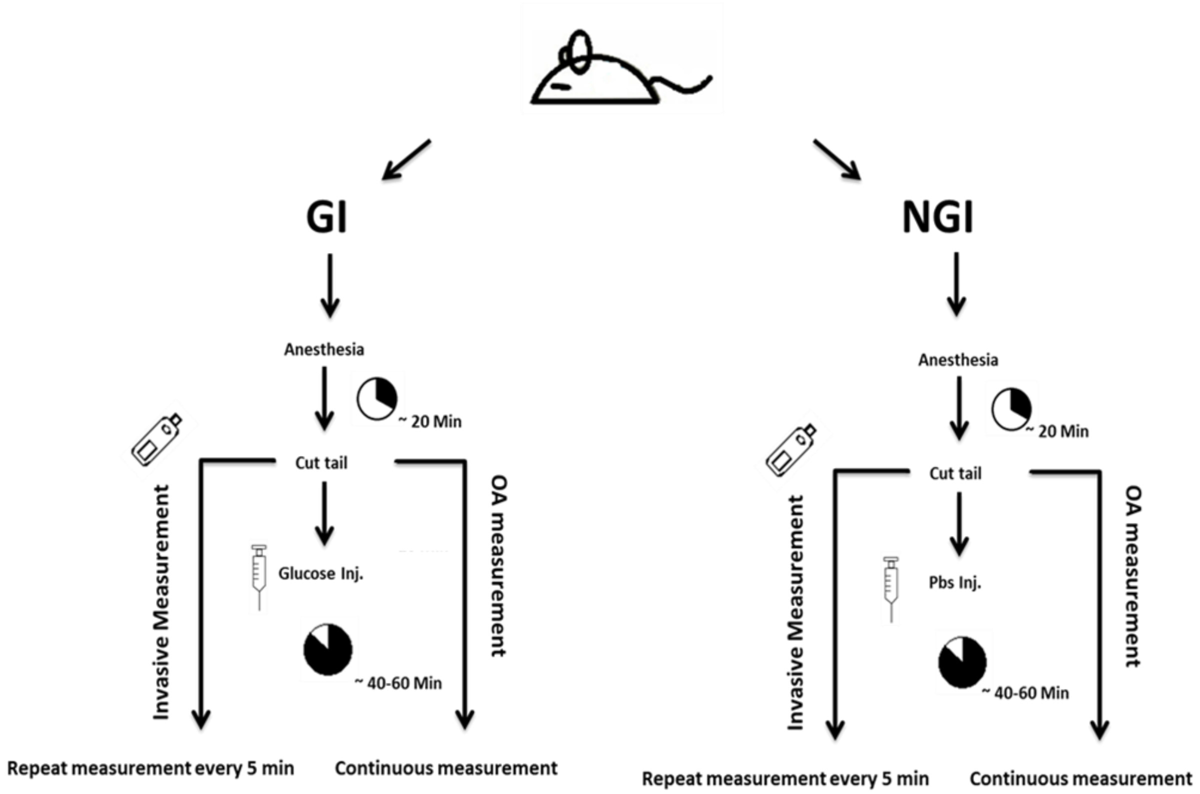
GI
NGI
Anesthesia
~ 20 Min
Cut tail
Glucose Inj.
Pbs Inj.
~ 40-60 Min
Invasive Measurement
OA measurement
Repeat measurement every 5 min
Continuous measurement

Figure 3.7 Workflow is showing different stages of the experiment with glucose injected group (N=10) and control group (N=6).

Measurements were stopped earlier if the deterioration in health conditions was observed. Factors related to anesthesia effects such as respiration, heart rate, and glucose level drop were monitored closely. After completing the optoacoustic measurements, animals were sacrificed, and skin samples were collected for histological analysis (Figure 3.8).

As shown in the work flow chart (Figure 3.7), at the beginning of each measurement cycle, mice in both groups were anesthetized and left for 20 min to recover from anesthesia-associated stress [66]. The body temperature was carefully stabilized at 34 $\pm 0.3\ C^o$ using body temperature optimizer (PhysioSuite, US) and 1 mm tail tip was cut to allow blood sampling every ~3-5 min and glucose testing using a standard enzymatic test strip glucometer (Counter Next One, Bayer, Germany). Then, OA raw signals were collected continuously through a folded skin on the animal’s back. Animals were positioned carefully to allow the collection of OA signal from the skin tissue. The illumination was performed with a non-ionizing beam with controlled energy of 0.2 mJ/pulse (0.1 mJ in each path). The OA measurements were done through transmission mode, and each measurement cycle took approximately 3 min (from 1450 nm to 1800 nm in 10-nm steps). After the blood glucose had been measured twice at each wavelength (between 4-10 minutes after cutting the tail tip), the animal was injected intraperitoneally (i.p.) with either glucose (glucose injected mice) or PBS (control group), and blood glucose measurement was continued for 50 min.

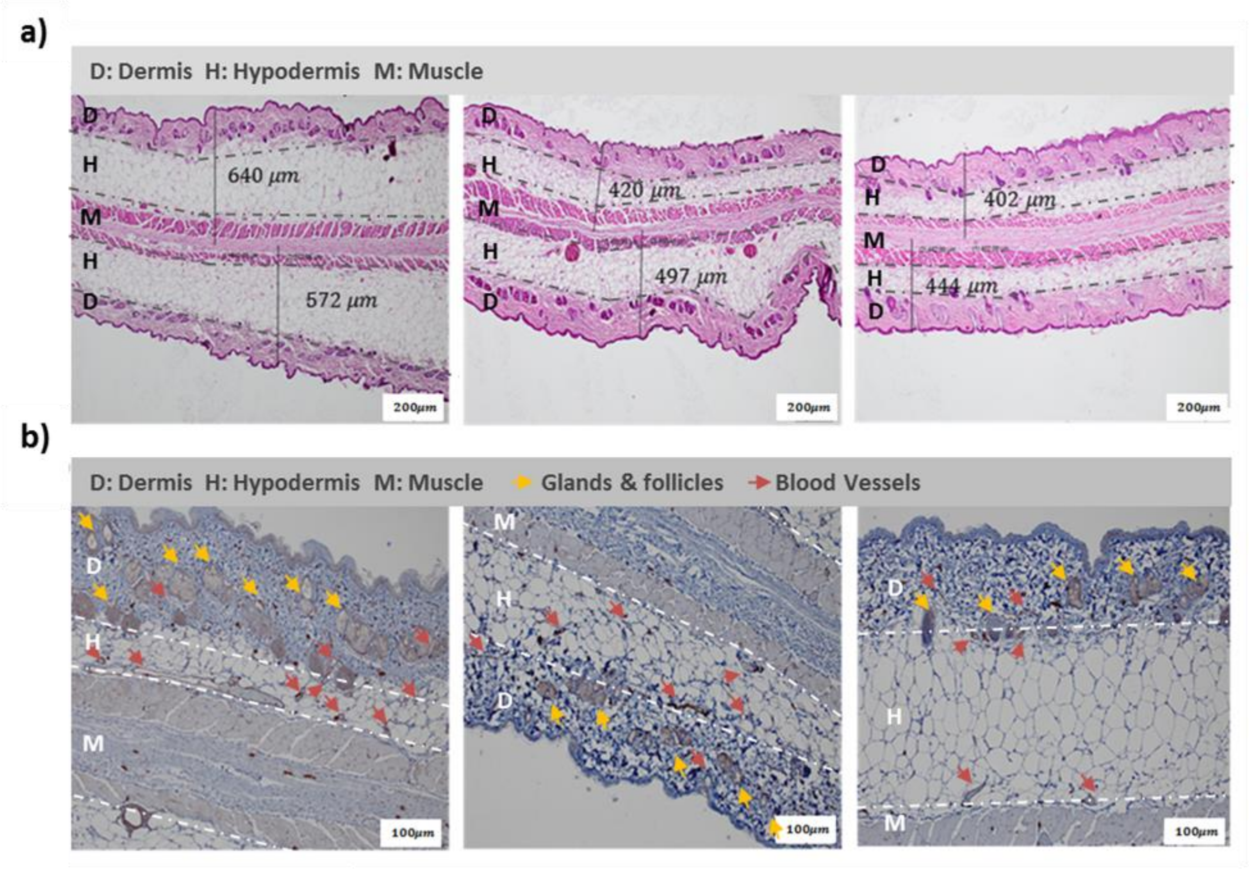
a)
D: Dermis H: Hypodermis M: Muscle
D
H
M
H
D
640 μm
572 μm
420 μm
497 μm
402 μm
444 μm
200μm
200μm
200μm
b)
D: Dermis H: Hypodermis M: Muscle
Glands & follicles
Blood Vessels
D
H
M
M
H
D
D
H
M
100μm
100μm
100μm

Figure 3.8 Skin histology and changes in thickness and homogeneity of each layer. Here D stands for dermis layer (including epidermis), H stands for hypodermis, and M stands for muscle layer (including fascia). a) Histology of folded skin of three different mice represents how the thickness of skin layers changes in different mice. b) CD31 histology of three different mice to depict blood vessels (red arrow) and follicles/glands (yellow arrow) more clearly and representing the most informative (due to the presence of blood vessels) and the most heterogeneous (change in the structure of the layer through optical paths due to presence of glands) region to sense glucose directly from blood.

As shown in Figure 3.8, three main layers of the skin can be clearly discerned. The epidermis is the outermost layer of the skin, and it does not have blood vessels within it. Beneath the epidermis, there is the papillary layer of the dermis with collagen structure, a small number of fat cells (adipocytes), and an abundance of small blood vessels. Beneath the dermis layer, hypodermis exists, which stores fat and provides insulation. Finally, there is the muscle layer and fascia, which are not skin layers but can be considered as the layer that covers and permeates the skin from below. This fibrous tissue layer does not have blood vessels and contains high water concentration.

Despite the presence of numerous microvessels in the dermis layer of the skin, the dermis layer is the most heterogeneous part of the skin due to the presence of different follicles and glands. Therefore, the OA signal produced in this layer can vary with different measurements depending on the laser beam path. Obviously, the hypodermis layer (including the junction of dermis and hypodermis) is most homogeneous and vascularized of the three layers of the skin [60], [67]; the larger vessels and microvessels can be clearly seen in these sections.

3.3 Results and analysis

The driving premise of this study has been that skin layer-specific detection of blood vasculature can improve sensitivity for sensing glucose. In particular, we hypothesized that targeting the vasculature-rich layers below the epidermis would provide the highest glucose contrast, as the OA measurements would directly reflect the blood glucose concentration, and the background noise would be minimized. The OA measurements have a stark contrast to optical sensors, which only provide bulk volumetric measurements of the skin volume, or MIR spectroscopy, which only measures the superficial epidermal layer. Therefore, a remaining challenge was to confirm this hypothesis and identify the optimal skin layer and excitation wavelength for glucose measurements.

To accomplish the layer and wavelength selection, we segmented the longitudinal OA measurements from all sixteen mice according to skin layers using the ML algorithm, as described above (Figure 3.3). Then, the OA intensity changes at different wavelengths (spectra) for each of the assigned segments of the OA signals (resembling skin layers) were compared to the gold standard glucometer readings recorded for each mouse. The OA intensity at a specific wavelength is defined as the area under the absolute envelope of the OA raw signal at that wavelength (see methods). To improve the glucose signal contrast over the background, we employed the referenced wavelength technique, (i) reducing the background signal; OA intensity at all wavelengths was subtracted by the reference OA intensity at 1710 nm, (ii) removing OA interference such as a change in temperature; the subtracted OA intensities were then normalized to the OA intensity at a reference wavelength (see methods). 1710 nm was chosen as the reference wavelength because glucose has the least absorption at 1710 nm in the SWIR wavelength range considered (Figure 3.6). The mice were kept at a constant temperature of 34±0.4 ℃, and the skin was fixed to minimize external influences on the correlation between OA intensity and changes in glucose concentrations (and avoid any motion artifacts).

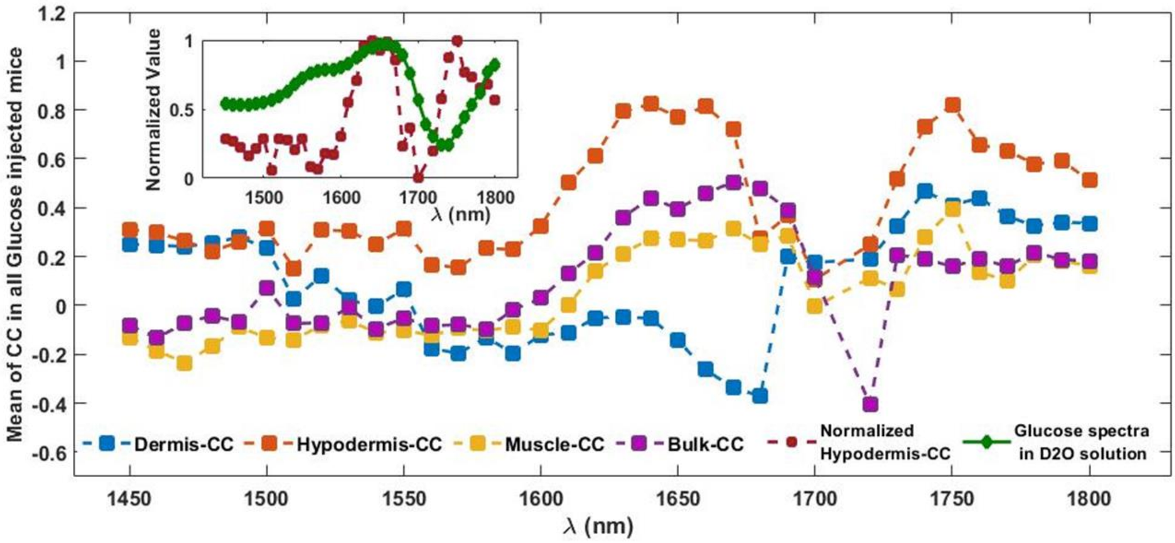

Figure 3.9 Importance of skin layers and illumination wavelength to glucose sensing. The average correlation coefficient between the OA intensities and test-strip measurements is indicated for the data pooled from all ten animals. Coefficients are shown for specific skin layers, as assigned by the ML algorithm, and for bulk skin, defined as everything from the epidermis to the muscle and fascia. The inset figure shows a comparison of normalized pure glucose spectra with normalized mean of correlation coefficients (CC) in the hypodermis layer, averaged for all ten mice.

Figure 3.9 shows how skin layer-specific detection allows the delineation of various skin layers where glucose can be measured most accurately. The mean correlation coefficient between OA intensities and glucometer readings for measurements obtained from different skin layers over a broad range of wavelengths for ten mice that were injected with a glucose solution. The correlation curves versus wavelength show the same change in pattern for all the different layers. However, the highest correlation was observed for glucose signals in the hypodermis layer at a wavelength of approximately 1650 nm, where the correlation coefficient was 0.82 (by taking an average for the ten mice (see also Table 3.1)). At nearly all wavelengths where glucose absorbs heavily (1600-1680 nm), signals from the hypodermis correlated better with the test-strip reference than those obtained from the dermis, muscle, or overall bulk-skin measurements. Figure 3.9 inset, shows the similarity of the normalized mean correlation coefficient values in the hypodermis layer and the normalized pure glucose spectra obtained in heavy water (see Figure 3.6). The curves' overall pattern is very similar, in particular between 1600-1700 nm, where glucose has a distinct fingerprint that is not affected by water contributions (see Figure 3.6). However, there are some differences between the two patterns at 1450-1500 nm and 1750-1800 nm wavelengths, where water contribution is significant. Table 3.1 shows a comparison of correlation coefficients between OA intensities at 1650 nm (after normalizing with reference OA intensity at 1710 nm) at different skin layers and gold standard glucometer readings in all glucose injected and control mice groups. On average, it is evident that the mean of the correlation coefficient is higher for the hypodermis layer for ten glucose injected mice ($R = 0.82$) and six control mice group ($R = 0.59$), showing higher sensitivity at this layer. More importantly, the standard deviation of the correlation coefficients at the hypodermis layer is on average 0.38 (0.19 for glucose injected mice and 0.54 for control mice groups), showing more reliability of measurement at this layer when compared to other skin layers and bulk skin measurement.

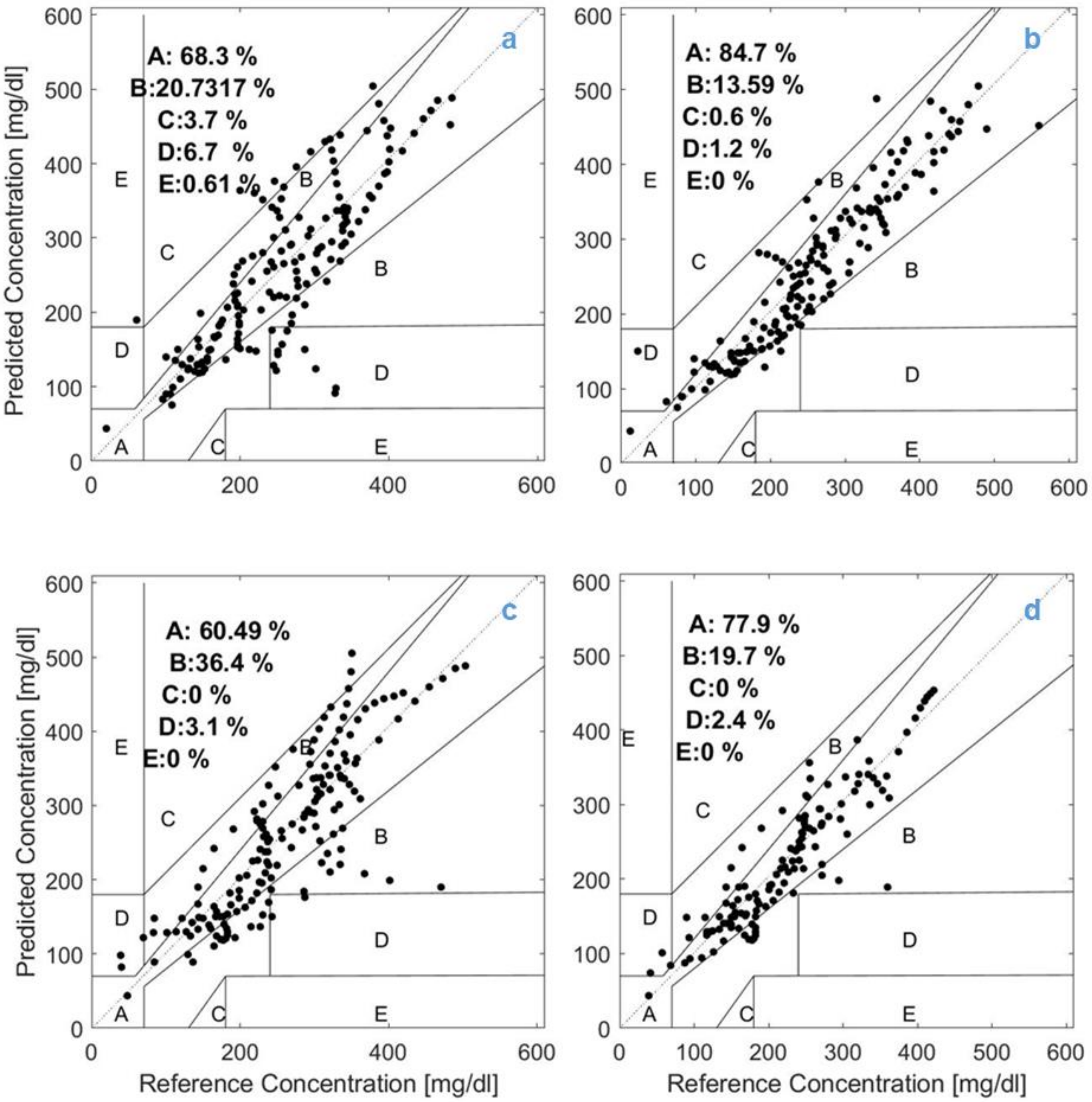

Figure 3.10 The Clark Error Grid displays the accuracy of the glucose-sensing using OA intensities at 1650 nm wavelength at the (a) dermis, (b) hypodermis, (c) muscle and fascia, and bulk skin (e) in 10 mice after glucose injection. LOOC method was used to predict glucose levels from OA intensities at 1650 nm.

Figure 3.10 shows Clark's display of the predicted glucose level at 1650 nm (after normalizing with 1710 nm reference wavelength OA signal) compared to the glucometer readings in all glucose injected mice (see also Table 3.2). The leave-one-out-cross-validation method was used to predict measured glucose levels from OA intensity at the wavelength of interest (see method). It was evident that the hypodermis layer with ~85% of the predictions at A region is the most informative skin layer to measure glucose concentration. Table 3.3 represents the root-mean-square-error (RMSEcv) between predicted glucose values at 1650 nm (after referencing to 1710 nm) and the gold standard. On average, we can see ~31 mg/dl of prediction error in all glucose injected (~45 mg/dl) and control mice groups (~ 8 mg/dl) in the hypodermis layer, which is the least prediction error among all skin layers. Similar to the observations in correlation-coefficients (see Table 3.1), the hypodermis layer results show the least standard deviation in results, not only representing the better accuracy but also higher reliability of results. These results suggest that the accuracy of glucose measurements *in-vivo* depends strongly on location. This may help explain the relatively low accuracy of previous OA and purely optical techniques that measured the glucose signal from bulk skin.

The above results imply that OA measurements using 1650 nm excitation and machine learning to target the hypodermis layer would provide optimal correlation with changes in actual blood glucose concentrations. Figure 3.11 shows a comparison between glucometer readings and OA measurements at 1650 nm in the skin's hypodermis layer for all sixteen mice, ten of which were injected with a glucose solution and six of which were injected with a PBS as a control. The measurements were taken for ~50 minutes. Figure 3.11a and b show the result for three typical mice. The first two mice were injected with glucose at two different time points, i.e., 4, and 30 minutes after starting the measurement, to see if the increase of the optoacoustic signal increase correlates with the glucose injection time. The last mouse was injected with PBS instead of glucose to ensure that the OA signal increase is not due to the injection and water concentration increase. From Figure 3.11, it is obvious that the OA intensities in the hypodermis tracked well with the glucose concentrations measured invasively from blood in both groups of mice. There was some deviation in the shape of the curves, particularly in the control mice group; however, the OA measurements in these cases still indicated an increase or decrease in glucose levels that corresponded with the changes seen in the blood measurements. Discrepancies in the measured glucose concentrations that change more than 40 mg/dl during the experiment in the glucose injected mice and the control mice are likely due to the measurements being made at two different locations (back and tail), which differed in their distance from the injection site. In addition, the test strip manufacturer indicates an error of 10-20%. In two control mice, glucose concentrations calculated from OA measurements did not correlate well with the reference measurements, but this may be due to the overall low change in the glucose concentration during the entire experiment in the mice (e.g., in control mice 4 and 6 in Figure 3.11, glucose concentration changes 15 mg/dl and 30 mg/dl, respectively).

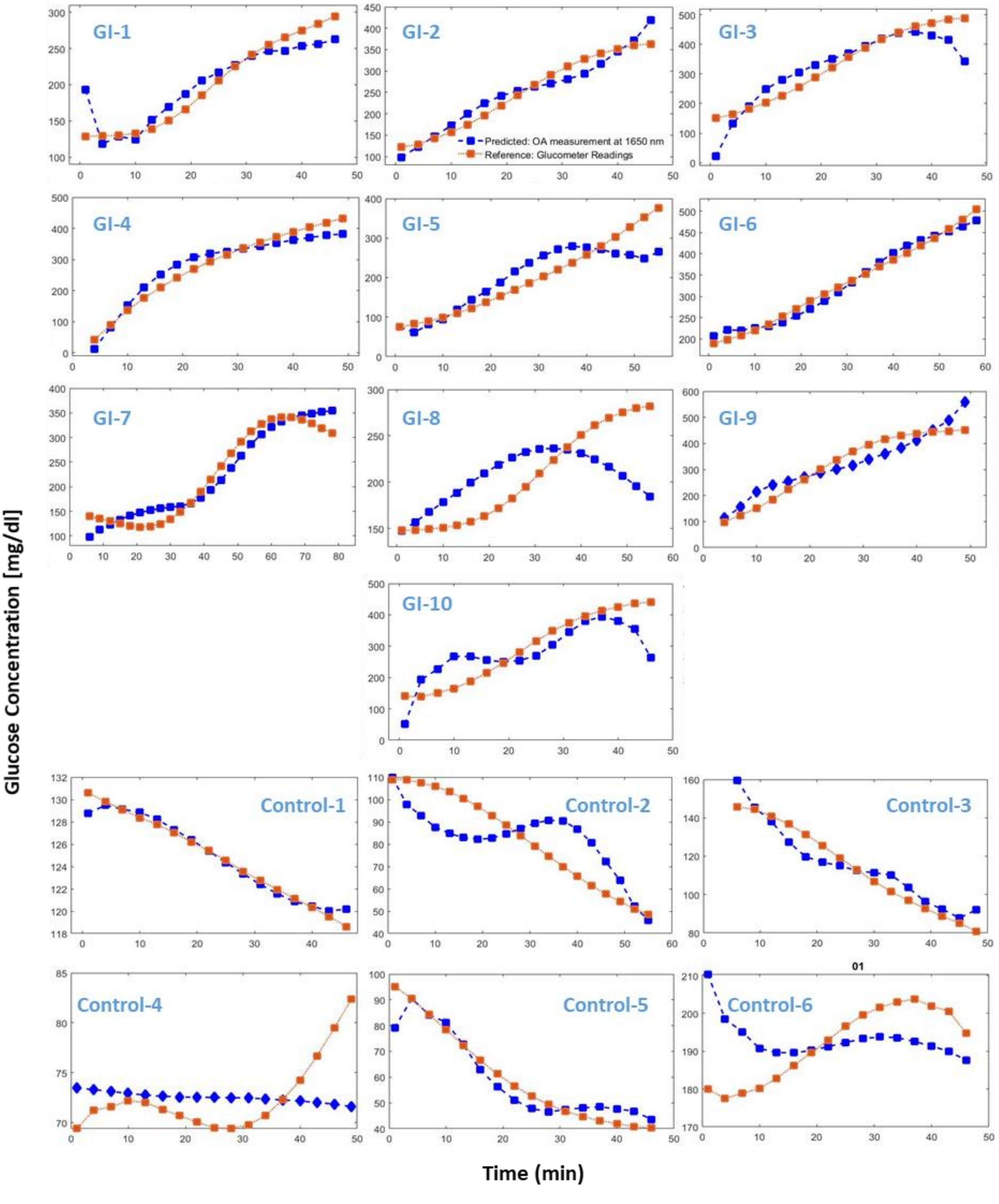

Figure 3.11 A comparison of OA measurements in the skin's hypodermis layer at 1650 nm to reference glucometer readings in ten mice after glucose injection (GI group) and six mice after PBS injection (Control group). Sixteen mice that received glucose injections or PBS were scanned for approximately 50 minutes after injection over the same skin region. The blue square represents OA measurements, and the orange square represents glucometer readings.

Table 3.1 The correlation coefficient between OAI at 1650 nm (after referencing to 1710 nm) at different skin layers and glucometer measurements. The last six rows are showing the mean and standard deviation of results for all mice (Mean, SD), glucose injected mice group (Mean-GI, SD-GI), and control mice group (Mean-Control, SD-Control), respectively. The green color represents the best results (top 10% at each category), the yellow color showing the results in the first percentile (between top 25 to 10%), and the red color are the worst results.

	Dermis	**Hypodermis**	**Muscle**	**Bulk**
GI-1	0.94	0.84	-0.96	-0.96
GI-2	-0.09	0.94	0.96	0.97
GI-3	-0.99	0.83	0.99	0.93
GI-4	-0.90	0.97	0.80	1.00
GI-5	0.85	0.85	0.77	0.88
GI-6	-0.84	0.99	0.38	0.53
GI-7	0.97	0.96	-0.84	-0.84
GI-8	-0.40	0.48	0.72	0.87
GI-9	0.44	0.90	0.84	0.95
GI-10	-0.53	0.47	-0.92	0.08
Control-1	0.96	0.95	0.98	0.98
Control-2	0.99	0.73	-0.02	0.80
Control-3	-0.13	0.88	0.90	0.56
Control-4	-0.09	-0.03	-0.06	-0.63
Control-5	0.99	0.93	-0.97	0.38
Control-6	-0.27	-0.29	0.24	0.68
Mean	✗ **0.12**	✓ **0.71**	✗ **0.24**	✗ **0.45**
SD	✗ **0.75**	✓ **0.38**	✗ **0.77**	✗ **0.68**
Mean-GI	✗ **-0.05**	✓ **0.82**	✗ **0.27**	✗ **0.44**
SD-GI	✗ **0.79**	✓ **0.19**	✗ **0.83**	✗ **0.76**
Mean-Control	✗ **0.41**	✓ **0.53**	✗ **0.18**	! **0.46**
SD-Control	✗ **0.63**	✓ **0.54**	✗ **0.72**	! **0.57**

Table 3.2 Comparing the data located in A region of Clark grid error (∓20% of glucosemeter measurements): the predicted glucose levels are calculated after applying OA measurement at 1650 nm (after referencing to 1710 nm and performing LOOCV) at different skin layers. The percentage of the data located in the A region of the Clark grid error display is shown as a bar plot, where longer bars show the best results, and shorter bars show the worst results.

	Dermis (%)	**Hypodermis (%)**	**Muscle (%)**	**Bulk (%)**
GI-1	100	94	94	100
GI-2	25	94	88	90
GI-3	94	81	100	90
GI-4	56	100	25	100
GI-5	84	63	28	82
GI-6	80	100	45	45
GI-7	96	84	44	44
GI-8	37	63	63	89
GI-9	29	88	75	88
GI-10	25	56	81	18
Control-1	100	100	100	100
Control-2	100	63	37	95
Control-3	60	100	100	80
Control-4	100	100	100	100
Control-5	100	94	100	75
Control-6	100	100	100	100

Table 3.3 Comparison of RMSE_{CV} between predicted glucose measurement at 1650 nm (after referencing to 1710 nm and performing LOOCV) at different skin layers and glucometer measurements. The last six rows are showing the mean and standard deviation of results for all mice (Mean, SD), glucose injected mice group (Mean-GI, SD-GI), and control mice group (Mean-Control, SD-Control), respectively. The green color represents the best results (top 10 % at each category), the yellow color showing the results in the first percentile (between top 25 to10 %), and the red color are the worst results.

	Dermis (mg/dL)	**Hypodermis (mg/dL)**	**Muscle (mg/dL)**	**Bulk (mg/dL)**
GI-1	22	32	21	19
GI-2	97	30	26	17
GI-3	20	62	14	37
GI-4	66	36	89	5
GI-5	51	54	69	27
GI-6	57	17	108	73
GI-7	22	27	52	52
GI-8	53	46	39	28
GI-9	130	63	100	50
GI-10	114	85	50	161
Control-1	1	1	1	1
Control-2	3	16	24	13
Control-3	26	10	12	20
Control-4	4	4	4	3
Control-5	3	7	5	19
Control-6	10	12	11	7
Mean	✗ **42.44**	✓ **31.37**	✗ **39.07**	! **33.37**
SD	✗ **41.30**	✓ **24.68**	✗ **35.61**	✗ **39.29**
Mean-GI	✗ **63.18**	✓ **45.19**	✗ **56.91**	✓ **46.99**
SD-GI	✗ **38.99**	✓ **20.78**	✗ **33.67**	✗ **44.59**
Mean-Control	! **8.90**	✓ **8.34**	✗ **9.34**	✗ **10.68**
SD-Control	✗ **9.25**	✓ **4.32**	✓ **4.36**	✗ **7.55**

3.4 Conclusion and Discussion

The correlation of the measured optoacoustic signals to changes in blood glucose concentrations is confounded by the imprecise nature of bulk skin measurements. This study combined an optoacoustic spectrometer utilizing light in the SWIR wavelength region with a machine-learning algorithm to measure glucose concentrations at different skin depths in live mice. The resulting layer-specific optoacoustic spectroscopic sensor, or LSOS, showed excellent correlation with gold standard glucose readings from blood samples in both control mice and mice injected with glucose. Our results greatly improve the accuracy of previous efforts to measure glucose using OA or purely optical methods, providing a viable route to develop non-invasive, optical-based devices for glucose monitoring, much needed for diabetes patients.

We showed for the first time that a 1D OA signal could be segmented into the corresponding skin layers using a simple machine learning algorithm. Specifically, this algorithm employed a Hilbert transformation rather than a peak-to-peak of the signal to gain comprehensive information that is less affected by water, metabolites, and other absorbers. Spectra taken from the segmented areas of the signal corresponded to the expected compositions of the respective skin layers, validating the efficacy of the algorithm. Furthermore, taking advantage of multispectral measurement and using the OA intensity at 1710 nm as a reference, we have minimized the background signal and some interferences such as the temperature change effect, to maximize the glucose signal contrast above the background signal. Finally, the calculated skin-layer thicknesses compare qualitatively to histological results. Note that the segmentation of different skin-layers accurately would be challenging with purely optical methods due to scattering of the reflected signal.

Having shown that it is possible to segment the OA signal into skin layers using machine learning, we demonstrated in live mice that the signal from the hypodermis correlated accurately to variations in the blood glucose readings from the reference glucometer (Figure 3.9). This correlation was better than in individual layers (i.e., the epidermal layer) or in bulk skin, used in all previous optical and OA studies on glucose sensing. Besides, we determined the optimal excitation wavelength for the measurement of glucose to be approximately 1650 nm. This wavelength aligns with findings from our previous *in vitro* studies [56], [68], [69], with our measurements of glucose in heavy water (Figure 3.6), and with purely optical and simulation studies [70]. Both the dermis and hypodermis layers of the skin are highly vascularized; however, the hypodermis contains larger vessels compared to the ones present in the dermis layer, possibly explaining the better correlation of the hypodermis signal with changes in blood glucose [71]. In addition, the hypodermis is more homogeneous than the dermis (Figure 3.8), which contains more glands and hair follicles that may interfere with the reproducibility of the individual OA measurements. The hypodermis also includes a lower proportion of water than the dermis, which could contribute to background noise in OA measurements at SWIR wavelengths [61], [62].

Our measurements indicate that LSOS enables non-invasive OA detection of glucose *in vivo* with excellent accuracy. We further found that specifically targeting the hypodermis improves the correlation of the OA signal with changes in blood glucose levels more accurately, and the use of SWIR radiation allows for deeper penetration than MIR, enabling direct measurements from the blood (i.e., present in hypodermis). LSOS uses a new two-path design to reduce the effects of inevitable fluctuations in laser energy during spectral measurements, enabling real-time correction of the laser emission profile at different wavelengths. Despite the advantages of LSOS over existing optical techniques, there are still challenges to be overcome. The layer segmentation method is based on supervised learning a limited dataset, requiring one to acquire large amounts of annotated data to train the models. Furthermore, like all existing glucose monitoring techniques, LSOS must be calibrated before each experiment.

In conclusion, we show that LSOS enables the first-time skin-layer-based, non-invasive analysis of blood glucose content. This approach provides improved sensitivity to changes in glucose concentrations over other optical techniques. In a sense, our combination of LSOS and machine learning allowed us to "isolate" the glucose signal in two ways. Firstly, by focusing on the hypodermis, we could reduce errors due to the heterogeneity, i.e., by the presence of abundant water and fat in the dermis. Secondly, using the SWIR spectral range, allowed for deeper light penetration and specific spectral region for glucose sensing avoiding interference from other chromophores like lipids, proteins, collagen, etc. Our results suggest that *in-vivo* glucose measurements are likely to be more accurate if we focus on glucose signal in the hypodermis layer rather than bulk skin.

4 Short wavelength optoacoustic spectroscopy based on water muting

Content in this chapter is based on (at parts verbatim) the following journal paper:

Prakash, J.*, Seyedebrahimi, M. M.*, Ghazaryan, A.*, Malekzadeh-Najafabadi, J., Gujrati, V., & Ntziachristos, V. (2020). Short-wavelength optoacoustic spectroscopy based on water muting. *Proceedings of the National Academy of Sciences*, *117*(8), 4007-4014.

4.1 Literature and theoretical background

Estimating changes in the concentration of glucose, proteins, lipids, and collagen is essential in biomedical examination and diagnostics or therapeutics [72]–[78] and can prompt separating healthy from ailing tissues [79]–[82]. Since many biomolecules show absorption of light in the ultraviolet (UV), visible, and infrared (IR) spectral regions, consequently, can be distinguished by optical spectroscopy [83], [84] (OS). Yet, regardless of OS's wide use, sensing of various chromophores accompanies different drawbacks that rely upon the wavelength and frequency utilized. UV wavelengths cause photodamage in organic samples, while visible and near-infrared wavelengths generally provide low sensitivity for lipids, sugars, and proteins [85], [86]. For example, longer wavelengths, i.e., those in the short-wave IR (900-1800 nm), can detect endogenous particles like proteins, lipids, and sugars with higher contrast, yet the efficacy of the procedure is restricted by the absorption of water [83]–[86].

One way to avoid water absorption is to label target biomolecules with fluorescent dyes to increase detection sensitivity [87]. Raman spectroscopy is also considered to detect nonpolar molecule’s symmetric vibrations and is not influenced by water absorption. Even though Raman spectroscopy can be performed at the UV, visible, and IR frequencies, the UV and visible ranges are heavily impacted by background auto-fluorescence in tissues [76], [88]. Even weak fluorescence is much stronger than the generated Raman signal [88], which is why ultrasensitive trace detection is typically performed based on fluorescence (requires 10^{-16} cm^2/molecule) rather than Raman spectroscopy (requires 10^{-30} - 10^{-25} cm^2/molecule) [88], [89]. Therefore, longer wavelengths are preferred for Raman sensing. Nevertheless, Raman scattering by biological samples generally leads to low signal-to-noise ratios (SNRs) for detailed studies, reflecting the fact that usually only 1 in 10^{10} photons undergo a Stokes or anti-Stokes shift [81], [88], [89]. The Raman signal can be strengthened by increasing light intensity, but this leads to photo-damage. Alternatively, significant detection improvement can be achieved by bringing molecules close to metallic nanostructures in so-called surface-enhanced Raman spectroscopy [89].

Optoacoustic spectroscopy has also been considered for sensing biologically important chromophores in an aqueous medium, including hemoglobin, melanin, or contrast agents such as gold nanoparticles and organic dyes [90]–[94] and in analytical chemistry and nanomedicine applications [95], [96]. Synonymous to optical techniques, optoacoustic detecting is restricted by water absorption at longer wavelengths. Water contributes negligibly to optoacoustic measurements in the visible range (450-650 nm) and near-infrared range (650-900 nm) [85]. However, it contributes immensely to measurements at wavelengths longer than 900 nm, restricting the efficacy of the method for distinguishing proteins, lipids, collagen, and sugars [85], [97], [98]. Measurements of the optical absorption spectrum of glucose and lipids have been recently performed [85], [99] with low sensitivity because of the heavy absorption by water.

4.2 Introduction

In this work, we investigated the reliance of optoacoustic signals on the examined mediums temperature and presented cooled IR optoacoustic spectroscopy (CIROAS) to mute water contribution while performing optoacoustic spectroscopy. We show that estimations of proteins, lipids, and glucose in the short-frequency infrared (SWIR) spectral range, performed at 4 °C, lead to improvements over ordinary optoacoustic or IR spectroscopy. CIROAS can empower another spectroscopic methodology with remarkable potential suggesting a straightforward method to improve the sensitivity of detecting different metabolites in biological samples.

We hypothesize that we can improve the sensitivity of optoacoustic spectroscopy by limiting the OA signal generated by water by adjusting the temperature of the sample being analyzed. Our hypothesis relies on the fact that water's thermal expansion coefficient becomes zero at 4 °C [100]. Optoacoustic signals reliance on temperature has been experimentally demonstrated in the NIR regime (700-900 nm) [51], [93], [101], [102].

To examine our theory's legitimacy, we developed the first Cooled IR Optoacoustic Spectroscopy (CIROAS) and applied it to record optoacoustic spectra of lipids, bovine serum albumin (BSA), and glucose in aqueous solutions at various temperatures. For the first time, we muted water contribution at the NIR-II wavelengths (900-1900 nm), where sugars, lipids, and proteins emanate strong optoacoustic signals, compared to the NIR region where the generated OA signals through these chromophores are much weaker. Accordingly, we planned to eliminate the high contribution from water on the OA signals acquired in the NIR-II window and sense these moieties with higher efficacy.

Experiments were performed over several wavelengths in the NIR-II region and contrasted the detection sensitivity achieved using CIROAS with regular optoacoustic NIR-II spectroscopy at room temperature. The principles used in CIROAS concentrated on how solute concentration influences (a) the muting point of an aqueous solution (the temperature at which water signal is muted) and (b) the rate of change of optoacoustic signal with temperature. We further used the rate of change of the OA signal as a function of temperature to define the solute concentration quantitatively. Lastly, we elaborated on how CIROAS may considerably stretch out the capabilities of optoacoustic spectroscopy to detect biological molecules in cells and tissues.

4.3 Method

4.3.1 Theory

As briefly explained in chapter 1, the generation of optoacoustic signals requires pressure and thermal confinement criteria to be fulfilled [93], [103], [104]. Thermal and stress confinement conditions can be fulfilled by having the pulse width of light excitation shorter than heat and stress relaxation times, respectively [103]. When these rules are fulfilled, the fractional volume expansion (dV/V) created by the pulsed laser is defined as [103],

$$\frac{dV}{V} = -\kappa p + \beta T \tag{4.1}$$

where κ is the isothermal compressibility, β is the thermal expansion coefficient, and p and T represent the changes in measured pressure and temperature, respectively.

When light pulses used have pulse width in nanosecond range, the heating is rapid, and we can neglect fractional expansion (i.e. $\frac{dV}{V} = 0$). Accordingly, the pressure elevation after laser excitation can be written as [33],

$$p = \frac{\beta \Delta T}{\kappa} = \frac{\beta}{\kappa \rho C_v} H = \Gamma H \tag{4.2}$$

where Δp is local pressure rise, ρ is the mass density, C_v is the specific heat capacity, and H represents absorbed energy density after excitation. The light to sound conversion is heavily influenced by the dimensionless Grueneisen parameter (Γ) and can be rewritten as below [33],

$$\Gamma = \frac{\beta}{\kappa \rho C_v} = \frac{\beta v^2}{C_p} = g(T) \tag{4.3}$$

where v is the speed of sound, C_p is the specific heat capacity at constant pressure, and T represents the temperature of the medium being probed. Accordingly, the pressure elevation in the medium or optoacoustic signal is a function of temperature ($\Delta p = g(T)H$). The thermal expansion coefficient β is related to the temperature of the medium through the following equation [101],

$$\beta = \beta_1 + \beta_2 T \tag{4.4}$$

where β_1 and β_2 are the first two coefficients in a Taylor expansion of β. Therefore, the pressure elevation (optoacoustic signal) can be rewritten as follow,

$$\Delta p = \frac{(\beta_1 + \beta_2 T) v_s^2}{C_p} H \tag{4.5}$$

On the other hand, we know that the thermal expansion for the water at 4 °C is zero ($\beta_{water} = 0$) [100], [105], resulting in a muted optoacoustic signal at this temperature.

As we reduce the temperature further, we can see that the polarization of the optoacoustic signal changes from positive polarization (i.e., positive peak followed by negative peak) at the higher temperature to negative polarization (i.e., negative peak followed by positive peak).

This theory's underlying premise is that presence of any solute such as glucose, lipid, and proteins in the water will change the thermal expansion coefficient of the aqueous medium and alter the temperature dependency of the optoacoustic signal muting point when compared to water. The thermal expansion of the aqueous can be written as,

$$\beta_{aqueous} = \beta_{water} + \Delta\beta \tag{4.6}$$

and the generated optoacoustic signal can be written as,

$$\Delta p = \beta_{aqueous} \frac{v_s^2}{C_p} H = (\beta_{water} + \Delta\beta) \frac{v_s^2}{C_p} H \tag{4.7}$$

Assuming the first two coefficients of Taylor series expansion coefficients in the equation (4.4) are similar in water and aqueous solution, then the variation in muting point (T_{mute}) could be potentially used to measure the concentration of the solutes more accurately. We use long known Despretz equation, in which shift in the muting temperature of a solute vs. the muting temperature of water (i.e., 4 °C) as a function of solute concentration is given by the Despretz law, i.e., $\Delta T = Kc$, where K is the Despretz constant and c is the solute concentration [102], [106]. Rewriting equation (4.6) at the muting point, we get,

$$\beta_{aqueous} = \beta_1 + \beta_2 T = \beta_1 + \beta_2(T_{mute} + \mathit{\Delta} T) = \beta_{water} + \beta_2(\mathit{\Delta} T) \tag{4.8}$$

Therefore at 4 °C, the optoacoustic signal of the aqueous can be written as,

$$\Delta p = \beta_{aqueous} \frac{v_s^2}{C_p} H = \beta_2 \Delta T \frac{v_s^2}{C_p} H \tag{4.9}$$

and then using the Despretz equation, we can rewrite equation (4.9) as,

$$\Delta p = \beta_2 K c \frac{v_s^2}{C_p} H \tag{4.10}$$

Equation (4.10) indicates that the optoacoustic pressure detected at water muting temperature is proportional to the solute concentration and therefore can be used for quantitative spectroscopy purposes. We were particularly interested herein in identifying the use of equation (4.10) in the SWIR spectral region. Quantifying the changes in the optoacoustic signal intensity at SWIR excitation wavelengths at which the target solute strongly absorbs, under water muting conditions, could allow an accurate determination of target concentration with higher sensitivity than in the NIR.

4.3.2 Cooled IR Optoacoustic Spectroscopy

We developed a Cooled IR Optoacoustic Spectroscopy (CIROAS, Figure 4.1) and evaluated its use to detect metabolites such as glucose, lipid, and BSA. The system was built as a generalizable sensor and the studies that follow examined specific operational parameters that maximize sensitivity and eventually lead to a more portable setup. A tunable nanosecond SpitLight Single OPO laser (Innolas, Krailling, Germany) was employed to excite the sample in the entire NIR-II regime. The laser's output power was set to 0.5 mJ across the whole spectral region of 900 – 1900 nm, and scanning was performed with 10 nm step size. A cylindrically focused ultrasound transducer (UST) with a central frequency of 7.5 MHz (V319, Olympus Panametrics-NDT, Tokyo, Japan) adjusted in its focus to detect optoacoustic signal from the medium. The acquired optoacoustic signal was then amplified using a low-noise amplifier, AMP

(AU-1291, Miteq Inc., USA), and digitized using a data acquisition card (DAQ) with a sampling rate of 200 MS/s. A power meter was used to register the intensity of the light in the medium simultaneously. The measured intensities in the power meter were used to correct the laser intensity fluctuation during the scanning. The trigger signal from a photodiode (PD) was used to synchronize the signal acquisition in DAQ. The aqueous solution was located in a chamber, where the temperature was controlled accurately using Peltier elements and thermocouples (Figure 4.1). Six temperature sensors (thermocouple-based) were placed inside the chamber in a closed-loop configuration to measure the entire chamber's average temperature. Four Peltier elements were employed to control the temperature in the medium and maintaining the desired temperature. A mechanical stirrer was used continuously to mix the chamber's solution to ensure a medium homogeneous temperature while acquiring all the optoacoustic measurements reported here.

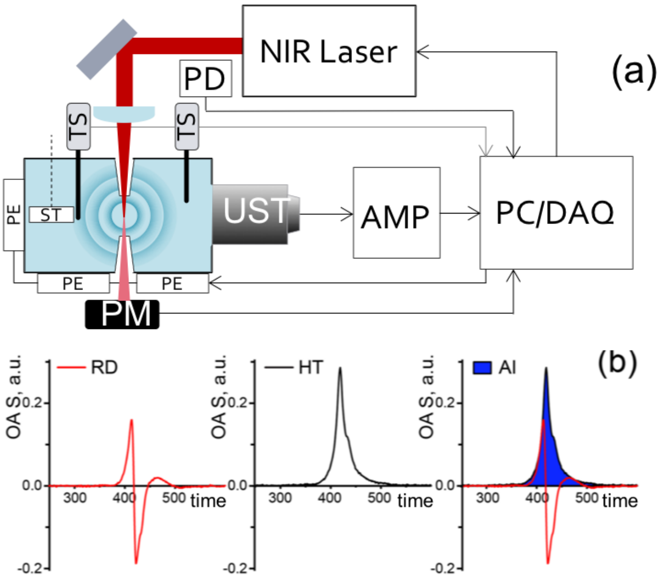

Figure 4.1 a) Schematic representation of the experimental setup for CIROAS. UST – ultrasound transducer; PD – photodiode; AMP – amplifier; TS – temperature sensor; PM – power meter; ST – stirrer; PE – Peltier Element; PC/ DAQ – personal computer with data acquisition card b) Data processing and analysis steps. OAS raw data (RD, left) was transformed by Hilbert transformation (HT, middle), and the area of interest (AI, right – in blue) under curves was taken as the intensity of the OAS signal (I_{OA}).

4.3.3 Data collection and processing

Data acquisition and processing were performed in MATLAB (Mathworks, Natick, MA). Obtained raw OA signal intensities were normalized per laser energy as registered by the power meter. The strength of the optoacoustic signal (I_{OA}) was estimated by computing the Hilbert transform of the recorded acoustic signal and integrating the area under the curve (Figure 4.1b) as previously suggested [98] and explained in chapter 3. For each wavelength, 40 optoacoustic measurements were recorded and averaged to increase SNR.

4.3.4 Experimental Measurements.

To investigate the advantages of cooled infrared optoacoustic spectroscopy (CIROAS), we examined different measurement of an aqueous solution at various temperatures from 1.4 to 25.8 °C using illumination at 1440 nm. In these examinations, the raw optoacoustic signal and muting temperatures were recorded. Next, we test the capability of CIROAS, for instance, to detect glucose in the NIR-II regime as an application. We tried to investigate whether glucose detection could be improved over traditional SWIR spectroscopy by cooling the medium's temperature. Hence, we set up a supply of D(+) glucose ($C_6H_{12}O_6$, Merck, Darmstadt, Germany) and add it to distilled water in the test chamber in 5 titrations range of 0 to 452 mg/dl. The test chamber contained 14 ml of distilled water. At every titration stage, 1 ml of the solution was first dispensed into the chamber, and then 1 ml of concentrated glucose was added to the reservoir aqueous solution from the stock solution. As a second application, we also performed CIROAS measurements in bovine serum albumin (BSA), having various glucose concentrations in serum solution at 160, 120, 80, and 30 mg/dl. BSA was prepared by filtering with a 0.4-micron filter. The measurements using CIROAS are then compared to glucometer (Contour Next One, Basel, Switzerland) readings. We also measured lipid solution as a third application, prepared by mixing intralipid (20% emulsion, I141-100ML; Sigma) in distilled water [14]. Finally, we performed CIROAS measurements to investigate sensing of physically relevant protein concentration by preparing 50 g/L of BSA solution.

4.4. Results

Figure 4.2 shows the optoacoustic response, particularly the water's muting property, as a function of temperature at the SWIR spectral region using CIROAS. We aim to confirm the hypothesis that the muting point measurement increases the detection and offers a more accurate estimation of metabolites concentration in an aqueous medium. Figure 4.2a shows a decrease in optoacoustic signal following the excitation at 1440 nm by decreasing the temperature from the initial temperature at 25.8 °C. The optoacoustic signal becomes zero at 4 °C. As shown in Figure 4.2b, a further decrease in the temperature increases the optoacoustic signal amplitude again, but changes the polarization of the optoacoustic signal from positive polarization (i.e., positive peak followed by negative peak) to negative polarization (i.e., negative peak followed by positive peak). Figure 4.2d shows the change in the optoacoustic signal amplitude as a function of temperature in the whole measured spectral window. It is evident that the amplitude of the signal decreases until zero at 4 °C, indicating an optoacoustically muted point, and again the amplitude increases by further reducing of the temperature. These measurements report on the change of polarity of the optoacoustic signal for temperatures below 4 °C and the muting of the optoacoustic response at 4 °C for water in the SWIR.

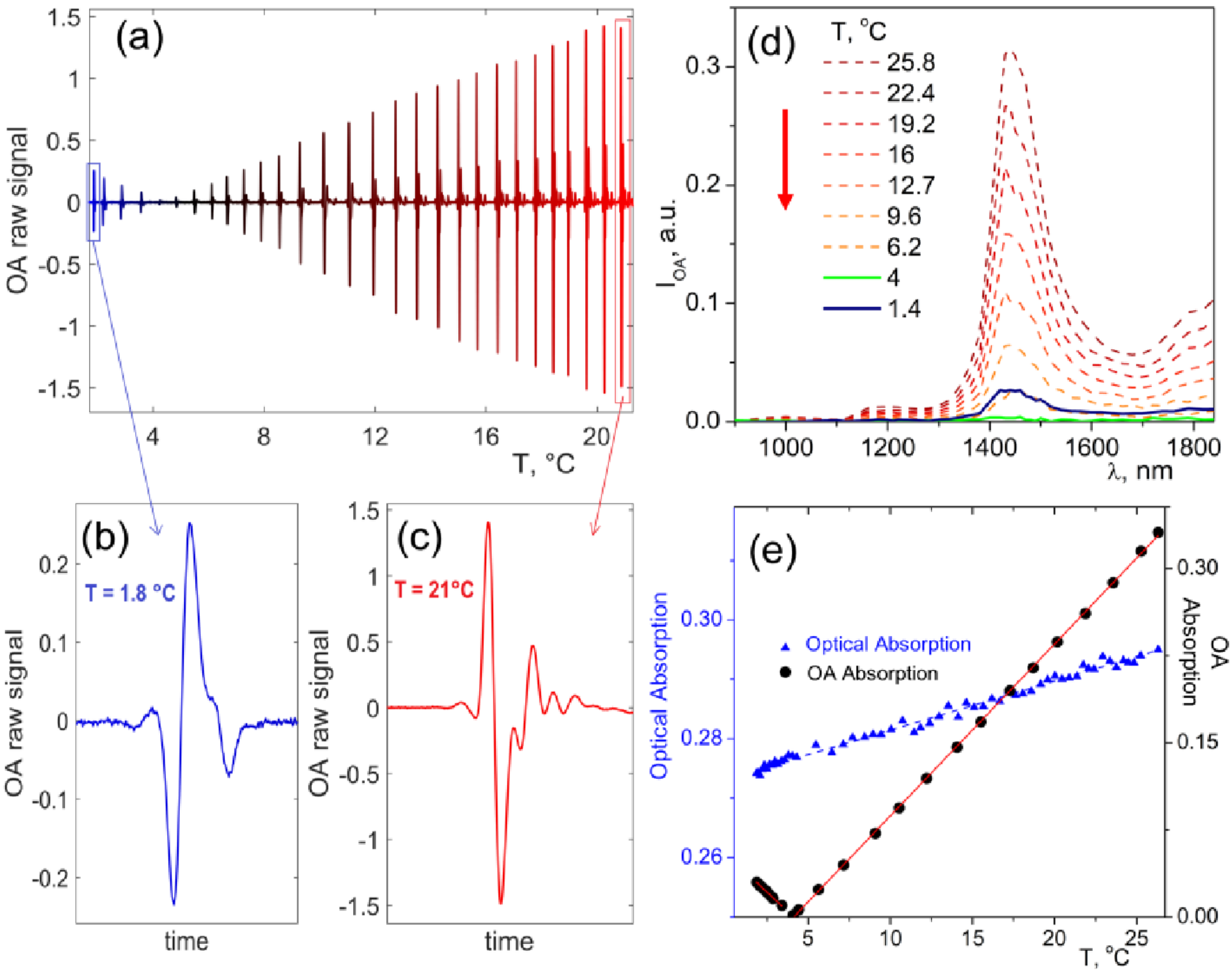

Figure 4.2 Optoacoustic signal of pure water at different temperatures after illumination in the SWIR range. (a) Raw optoacoustic signal of water at different temperatures after exposition at 1440 nm. (b) The temporal raw optoacoustic signal at 1.8 °C. (c) The temporal raw optoacoustic signal at 21 °C. (d) Optoacoustic spectra of water at different temperatures after illumination in the SWIR range. (e) Comparison of the signal obtained from pure water to varying temperatures after exposure at 1440 nm using optical and optoacoustic measurements.

Figure 4.2e delineates optical and optoacoustic signal recorded from distilled water at the temperature range of 1.4-25.8 °C following the excitation at 1440 nm. Beer-Lambert law was applied to the optical signal to calculate the absorption curve from the measured attenuated transmitted signals. The change in water absorption as a function of temperature, measured with the pure SWIR optical spectroscopy, showed only a minor incline of 0.001/°C. In contrast, the optoacoustic signal versus temperature showed a slope of at least 0.02/°C, indicating significant dependency of optoacoustic signal to temperature change. This affirms the potential advantage of utilizing optoacoustic spectroscopy over conventional optical spectroscopy at low temperature to decrease and even mute water contribution in the optoacoustic signal. This is important, as weaker absorption signal from other molecules are drowned in stronger water absorption signal at the SWIR wavelengths. Accordingly, we investigate the potential to boost the detection's sensitivity at lower temperatures in optoacoustic spectroscopy at SWIR spectral regime.

As an example application, we used CIROAS to detect glucose in the water (Figure 4.3). Conventional spectroscopies are relatively insensitive to detect the glucose spectrum, for instance, the absorption of glucose is around 1000 times smaller than that of water [63]; this is why different spectroscopy techniques are looking for the change of the acquired signal rather than measuring the glucose spectrum itself. Furthermore, sharing the same chemical bound (e.g., O-H bound) between glucose and water molecules leads to relatively the same optical fingerprints. It makes differentiation of the glucose spectrum even more complicated. Figure 4.3a exhibits an optoacoustic signal measured following the illumination at 1580 nm from an aqueous glucose solution with 452.2 mg/dl as a function of temperature ranging from 0.6 to 18.5 °C. Looking closely at optoacoustic signal change at 4°C (Figure 4.3a inset), we can see that the muting point is shifted to a lower temperature than 4 °C, the muting point of pure water. Figure 4.3b depicts the raw optoacoustic signal of pure water and the aqueous solution of glucose (452.2 mg/dl) at 1580 nm and 4°C. It is evident that the glucose signal shows a detectable optoacoustic signal with normal polarity (positive peak followed by a negative peak). In contrast, we can see that the optoacoustic signal is almost zero for water at this wavelength, revealing that the signal from aqueous glucose solution is only valid due to the presence of glucose molecules.

We also compared the spectrum of the pure water and aqueous solution of glucose with 452.2 mg/dl in the spectral range between 900 and 1900 nm. Figure 4.3c shows an almost zero optoacoustic signal for pure water, which yields a strong signal for glucose solution at 4 °C. Furthermore, comparing the optoacoustic signal from the same aqueous solution of glucose (452.2 mg/dl at 4 °C) with room temperature at 18 °C reveals differences in two spectra (Figure 4.3d). Figure 4.3d makes it evident that the water spectrum's morphology at 18 °C is very similar to the glucose spectrum at the same temperature due to the substantial contribution of water absorption, which shadows the glucose spectrum. However, by decreasing the glucose aqueous solution’s temperature to 4 °C, we can see that the spectrum is different, particularly at 1550-1700 nm. Figure 4.3e shows the spectrum of the aqueous solution of glucose at different temperatures. It is obvious that there is an appreciable amount of signal at 4 °C. Figure 4.3e also shows that the amount of optoacoustic signal decreases until 3.1 °C and again increases by further lowering the temperature (i.e., at 1.5 °C). Finally, Figure 4.3f compares the pure spectrum of glucose at different temperatures after subtracting by the water spectrum. All spectra are processed by removing the water spectrum at 18 °C. Note that as the water spectrum gives minimum optoacoustic contribution at the muting point (4 °C), the subtraction of all aqueous glucose solutions was performed by subtracting the normalized optoacoustic signal of aqueous at different temperature with the normalized spectrum of water at 18 °C. Figure 4.3f shows that the sensitivity to detect glucose increases by a factor of five-fold at 4 °C, specifically at wavelengths between 1500-1700 nm.

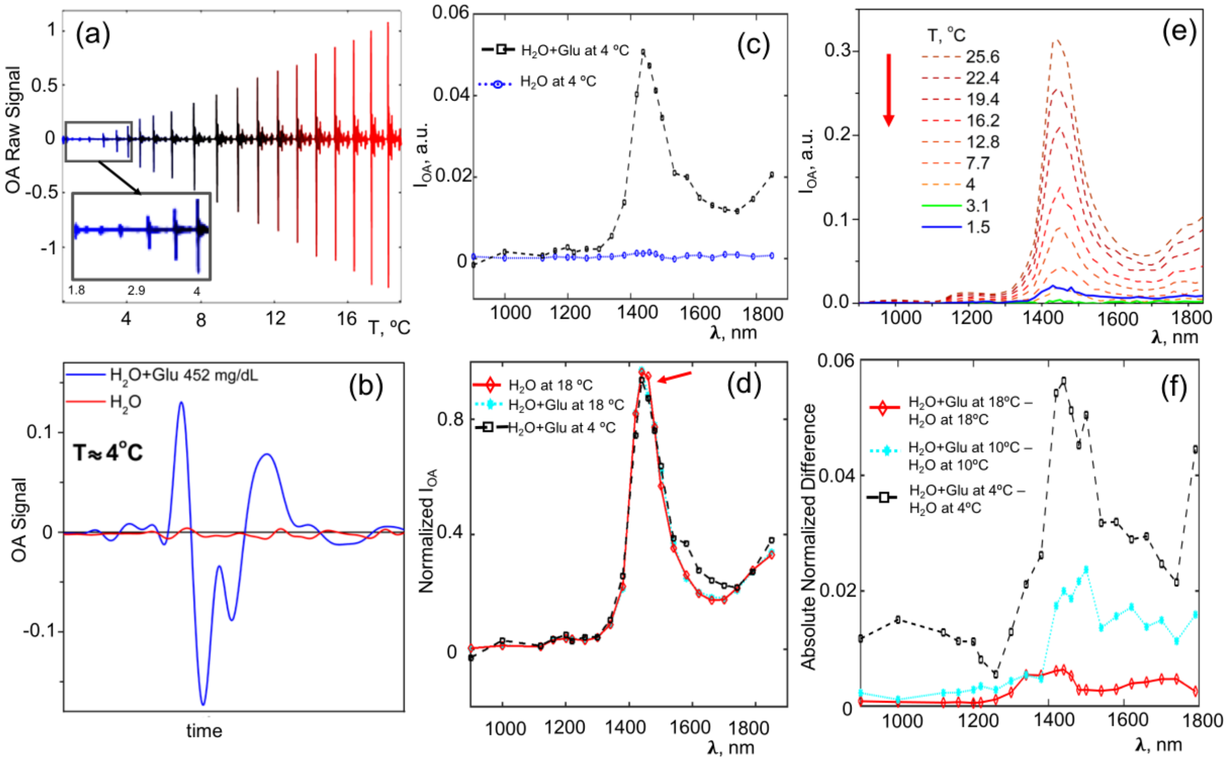

Figure 4.3 Optoacoustic signal of an aqueous solution of glucose (452.2 mg/dl) at different temperatures after illumination in the SWIR range. a) The raw optoacoustic signal at temperatures between 0.6 and 18.5 °C after illumination at 1580 nm. b) Superposition of the optoacoustic signals of pure water (red line) and the aqueous glucose (blue line) solution at 4 °C. c) Optoacoustic spectra of pure water at 4 °C (dotted blue line) and the aqueous glucose solution(dashed black line) at 4 °C. d) Normalized optoacoustic spectra of pure water (solid red), the aqueous solution of glucose at 18 °C (dotted cyan), and the aqueous solution of glucose at 4 °C (dash black). e) Optoacoustic spectra of the aqueous glucose solution at different temperatures after illumination in the SWIR range. f) The absolute normalized difference in OA signal was recorded from aqueous glucose and water solutions at 4 °C, 10 °C, and 18 °C.

To test the reproducibility of CIROAS, we repeated the measurement from an aqueous solution of glucose (Figure 4.4). The normalized optoacoustic signal of the water at 25 °C, aqueous glucose solution with a concentration of 400 mg/dl at 4 °C, and saturated glucose concentration at 25 °C are shown in Figure 4.4a. The saturated glucose solution was prepared by adding glucose to heated water until glucose could not dissolve anymore in the solution. It can be discerned that there is a clear difference in the spectral region ranging from 1550 to 1700 nm. The result is similar to our observation in the previous experiment for glucose (see Figure 4.4c & d). There are some differences in the spectra's morphology between water and aqueous glucose solution in Figure 4.3.c-d and Figure 4.4.a, possibly due to differences in water spectrum measured at 18 °C (Figure 4.3.c-d) and 25 °C (Figure 4.4).

Interestingly, we can also see that the normalized optoacoustic spectrum of saturated glucose is higher than its normal concentration at the physiological range at 400 mg/dl (Figure 4.4a) due to the nonlinearity effect. To study the nonlinearity effect as a function of glucose concentration, we measured optoacoustic signal at different wavelengths in an aqueous glucose solution with different concentrations (Figure 4.4b). Figure 4.4b shows the nonlinear behavior of the OA signal as a function of concentration. The nonlinearity effect increases exponentially at higher concentrations and is found to be wavelength dependent. As suggested before (Ref. [107]), the nonlinearity phenomena may further explain the differences in spectral morphology of saturated and physiological levels (i.e., 400 mg/dl) of glucose signal in Figure 4.4a.

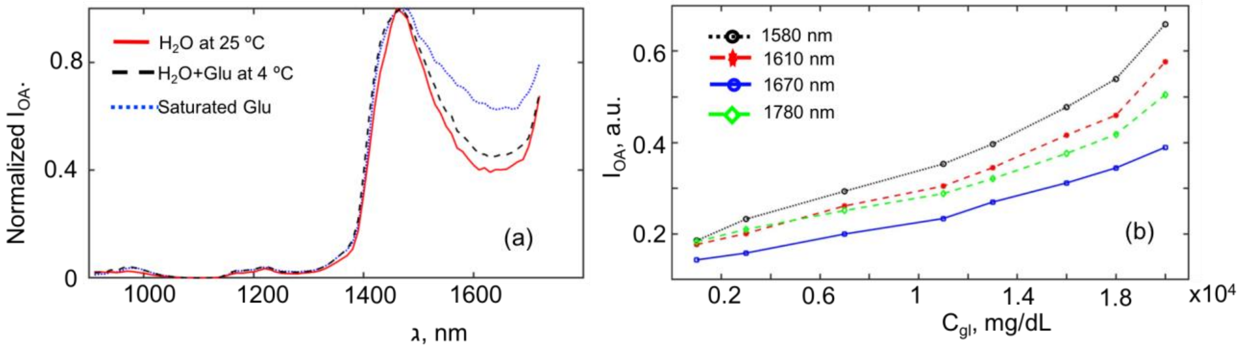

Figure 4.4 Optoacoustic signal of an aqueous solution of distilled water and saturated glucose at 25 °C and 400 mg/dl aqueous solution of glucose at 4 °C in the SWIR range. (a) Repeat optoacoustic spectra of pure water at 25 °C (solid red line), the aqueous solution of glucose (dashed black line) at 4 °C, and saturated glucose solution (dotted blue line). (b) OA measurements as a function of varying glucose concentration in water at different wavelengths to demonstrate non-linear behavior.

We also investigated how changing the glucose concentration alters the muting point and the OA signal dependence on temperature. This is similar to how solute concentration varies the boiling or the freezing points compared to the pure solvent's temperature. The experiment was perfumed with glucose solutions in distilled water with a concentration between 50 to 600 mg/dl. Figure 4.5 shows the optoacoustic signal from glucose concentration ranging from 149.6 to 452.2 mg/dl and exhibits a temperature dependence of the OA signal intensity at 1580 nm for pure water and aqueous glucose solutions. Overall, the range examined covers physiological and hyperglycemic levels reported in the brain and blood [74], [108], [109]. Linear fits to data show monotonic increases with temperature. The fitted lines intersect with the temperature axis at 4 °C for pure water, 3.7 °C for water containing glucose at 149.6 mg/dl, and 3.1 °C for water containing glucose at 452.2 mg/dl. The fitted lines corresponding slopes were 0.0582, 0.0538, and 0.0527 (change in OA signal/°C). These results indicate that both the temperature intercept and OA signal-temperature slope varied proportionally with glucose concentration. This dependence can be therefore employed for quantifying the concentration of biomolecules in solutions.

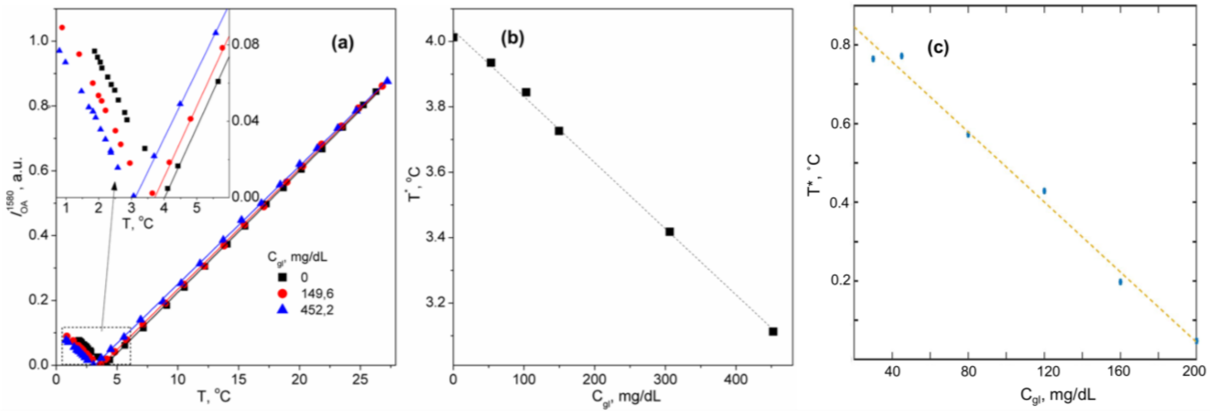

Figure 4.5 Temperature dependence of optoacoustic signal measured from water as a function of solute concentration. a) Temperature dependence of the optoacoustic signal intensity of pure water (black squares) and aqueous solutions of glucose at 149.6 mg/dl (red circles) or 452.2 mg/dl (blue triangles). Linear fitting of monotonically increasing signals is shown. (Inset) The muting point of each solution, defined as the intersection with the temperature axis. b) Variation in muting point (T*) with glucose concentration (C_{gl}). c) Variation in muting point (T*) with glucose concentration (C_{gl}) in serum solution.

We further studied the minimum detectable concentration of glucose at the muting point (Figure 4.6). The limit of detection (LOD) using CIROAS for glucose+H_2O was reliably observed at 50 mg/dl, and for glucose in serum was observed at 45 mg/dl. The precise controlling of the temperature with the current setup of CIROAS was not possible, and the temperature had ~0.4 °C fluctuation at the muting point. The smaller amount of concentration can also be detected by modifying the temperature regulation part of the CIROAS in the future. The sensitivity of the CIROAS was also investigated by adding a small amount of glucose concentration at a glucose level higher than the LOD of the device (i.e., 136 mg/dl). We found that adding 8 mg/dl of glucose at 136 mg/dl concentration of glucose+H_2O solution can be reliably detected (Figure 4.6). This means that CIROAS can reliably confirm the minimum of 50 mg/dl of glucose concentration (LOD) and 8 mg/dl change in glucose concentration (sensitivity). A comparison of the CIROAS glucose concentration measurements to glucometer measurements are summarized in Table-1. The comparison reveals that CIROAS outperformed the commercial glucometer device since it better predicted the known glucose concentration in the solution measured.

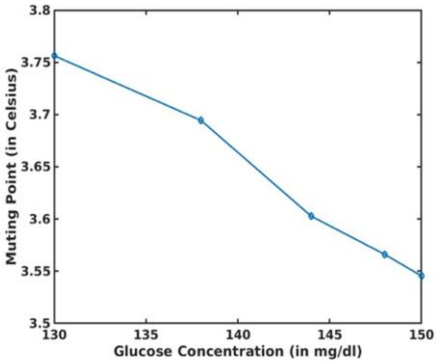

Figure 4.6 Variation in muting point with glucose concentration in water solution (for estimating the minimum distinguishable concentration).

Table 4.1 Indicates the actual concentration and the recovered values from CIROAS measurements and glucometer values.

Actual Concentration	CIROAS Measurement	Glucometer
30 mg/dl	39 mg/dl	14 mg/dl
45 mg/dl	42 mg/dl	40 mg/dl
80 mg/dl	79 mg/dl	77 mg/dl
120 mg/dl	123 mg/dl	124 mg/dl
160 mg/dl	157 mg/dl	185 mg/dl
200 mg/dl	202 mg/dl	235 mg/dl

We further examined CIROAS of lipid and protein detection compared to measurements at room temperature. Figure 4.7a shows measured OA spectra from 890 nm to 1000 nm for an aqueous solution of lipid at different temperatures. This spectral window was selected as lipid shows a distinct absorption peak at 930 nm, and water shows an absorption peak at 970 nm. We found that the 930 nm peak becomes visible at lower temperatures, but it is not prominent as we increase the temperature. We also observed that the OA signal continues to decrease as the temperature reduces below 4 °C. This signal decrease might be due to interference and OA signal cancellation between lipid (positive peak preceding negative peak below 4°C) and water (negative peak preceding the positive peak below 4 °C). Note that similar behavior was not observed while probing glucose solution. This may be because glucose is readily soluble in water than lipid molecules causing interference of the OA signals from lipid and water. Figure 4.7b indicates the normalized OA measurements (i.e. $\frac{x}{\max(x)}$, where x is the acquired OA spectrum) from lipid solution at 19 °C and 4 °C, showing the lipid solution's spectral difference at the two temperatures. It is evident that the real spectrum of lipid becomes more visible at lower wavelengths, where we cannot discern the same at higher temperatures. Figure 4.7c shows the ratio of the measured OA signal at 930 nm to that of 970 nm as a function of temperature for the measurements shown in Figure 4.7a. The curve shows that the relative signal obtained primarily due to lipid contributions at 930 nm becomes 4x stronger at lower temperatures than the signal obtained at 970 nm, attributed mainly to water absorption. This observation suggests a 4x lipid detection sensitivity improvement at lower temperatures.

Figure 4.7d indicates the measured OA spectra from 1000-1210 nm for an aqueous solution of BSA at different temperatures. BSA does not exhibit characteristic peaks in the measured wavelength range, but between 1000 and 1100 nm BSA shows a roughly constant absorption, whereas water decreases in absorption with increasing wavelength. Therefore, at lower temperatures, we clearly see a decrease in OA signal intensity and a flattening of the spectrum in the 1000 nm - 1100 nm range, reflecting the water muting effects. Figure 4.7e plots the normalized BSA solution measurements at 19 °C and 4 °C, showcasing the two temperatures' spectral differences. At 4 degree, the BSA solution shows a reduced signal compared to 18 degrees due to the reduction of water absorption contribution to the OA signal.

An analysis similar to the one performed in Figure 4.7c shows that the gradient of the optoacoustic signals obtained between 1000 nm and 1100 nm from the BSA solution decreases with reducing temperature. The gradient used in Figure 4.7f is calculated using $\frac{y_{1100}-y_{1000}}{100}$, where y_{1100} is the OA signal from BSA solution at 1100 nm, y_{1000} is the OA signal from the BSA solution at 1000 nm. We used a ratio of spectral peaks for the lipid measurement (Figure 4.7c) since the lipids have a distinct peak at 930 nm, whereby water at 970 nm. However, we used the gradient calculation in Figure 4.7f since the BSA spectrum does not have such distinct peaks in its spectrum. The gradient measure tends to be closer to 0 at lower temperatures, indicating that BSA spectral signature dominates at lower temperatures, but water contributions begin to appear with increasing temperature. The BSA detection sensitivity is 5 times greater at lower temperatures compared to higher temperatures.

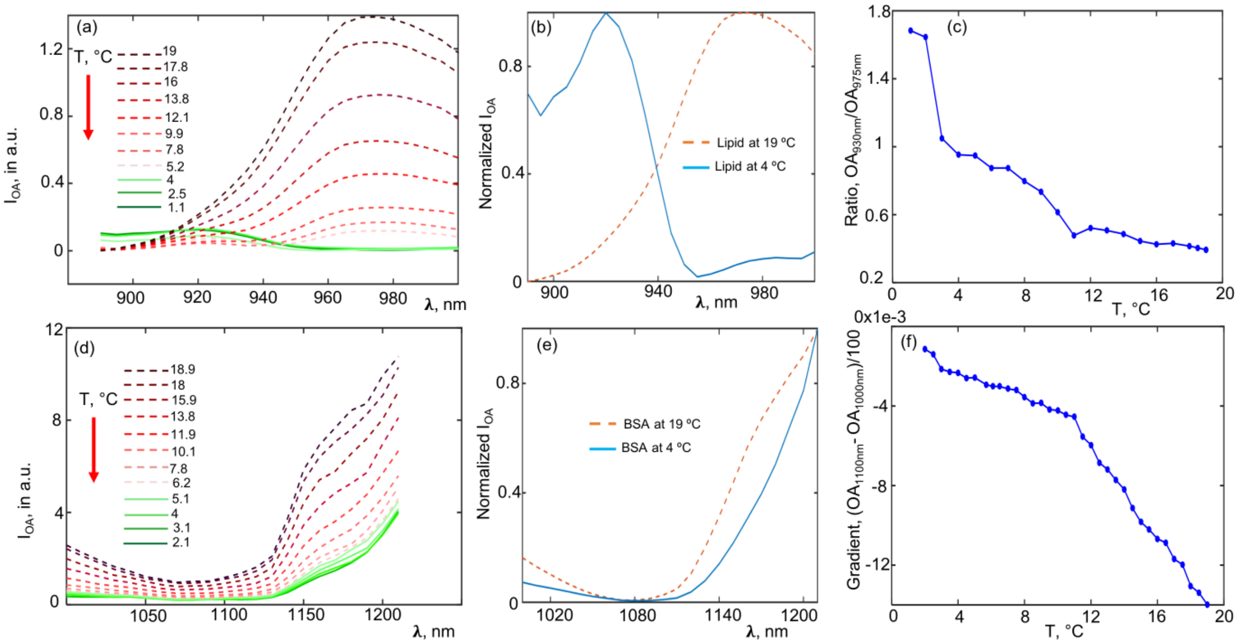

Figure 4.7 Optoacoustic signal of an aqueous solution of lipid (10%) and BSA (50 g/L) at different temperatures after illumination in the SWIR range. (A) Optoacoustic spectra of lipids in aqueous solution at different temperatures after illumination in the wavelength range of 890 to 1000 nm. (B) Comparison of normalized OA spectra of lipid solution at 19 °C (dotted orange line) and 4 °C (solid blue line). (C) The optoacoustic signal ratio from the lipid solution at 930 nm (lipid peak) signaled at 970 nm (water peak) at different temperatures. (D) Optoacoustic spectra of BSA in aqueous solution at different temperatures after illumination in the wavelength range of 1000 to 1210 nm. (E) Comparison of normalized OA spectra of BSA solution at 19 °C (dotted orange line) and 4 °C (solid blue line). (F) The gradient in the measured optoacoustic signal from the BSA solution between 1000 and 1100 nm at different temperatures.

We also examined the muting points for lipid and protein. In contrast to the glucose measurements, whereby the muting point was the same at all wavelengths, Figure 4.8a and b show that the muting point of lipid solution was higher at 930 nm (i.e., about 8 °C) compared to 970 nm (where muting point was at 2.5 °C). Moreover, Figure 4.8c shows the BSA solution's muting point at 1070 nm, found to be at 1.8 °C. However, the OA signal at higher wavelengths did not mute at all, as shown in Figure 4.5d. We currently investigate the variation of thermal expansion coefficient as a function of temperature for biomolecules such as glucose, lipids, and proteins to gain better insights into these muting point variations along the equations (4.8-(4.10). Finally, LoD and sensitivity measurements were also performed for the lipid solution. We found the LoD for lipid to be 2% of intralipid solution, using the current CIROAS setup, while the sensitivity of lipid detection, i.e., the minimum change that could be observed in our setup, was 1% of intralipid solution. Lipid LoD and sensitivity were determined as the minimum change of the OA signal ratio at 930 nm to the OA signal at 975 nm that could be reliably obtained using the CIROAS setup (Figure 4.9).

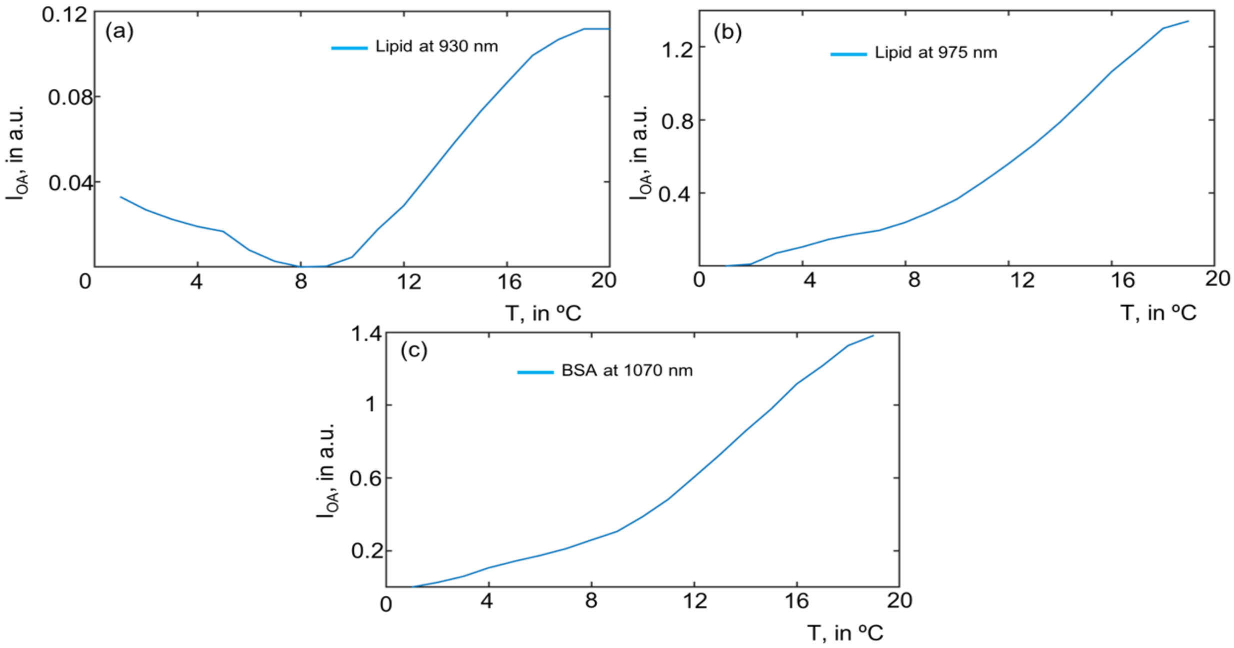

Figure 4.8 Variation of OA signal as a function of temperature for lipid and BSA solutions. (a) OA measurements as a function of temperature from lipid solution at 930 nm wavelength, (b) OA measurements as a function of temperature from lipid solution at 975 nm, (c) OA measurements as a function of temperature from BSA solution with 1070 nm illumination.

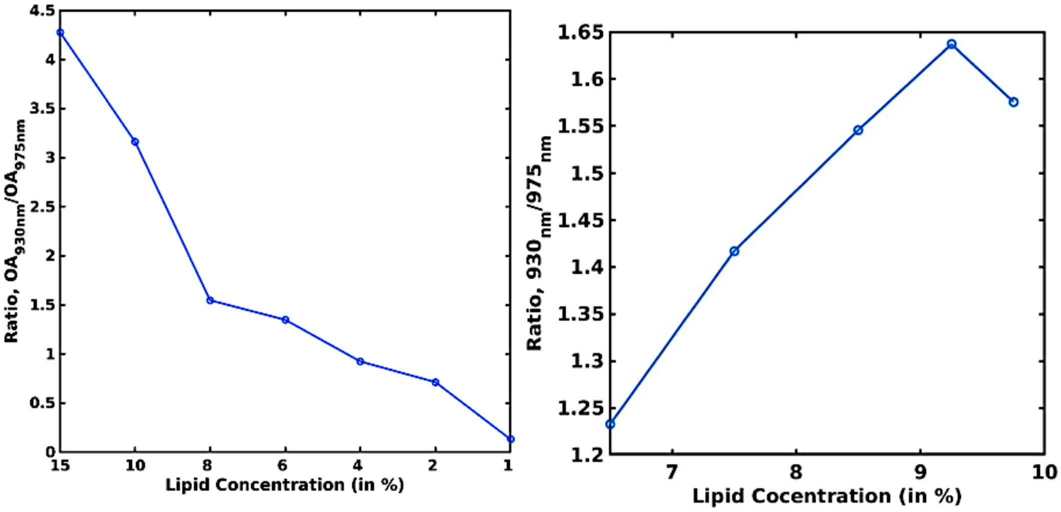

Figure 4.9 Ratio of OA signal of Lipid to that of water. a) Ratio of OA signal at 930 nm vs. OA signal at 975 nm for lipid solution at different concentrations (for estimating limit of detection), b) Ratio of OA signal at 930 nm vs. OA signal at 975 nm for lipid solution at different concentrations (for estimating minimum distinguishable concentration).

4.5. Conclusion and Discussion

We exploited the dependence of optoacoustic signals on temperature for improving the sensitivity of infrared spectroscopy. Compared to measurements at room temperature, CIROAS at 4 °C yielded on an average, a 5-fold sensitivity improvement in the SWIR over measurements at room temperature. These improvements can be observed as more pronounced spectral differences in the glucose spectrum (e.g., Figure 4.3f) or as relative changes for lipids and BSA, i.e., with respect to the ratio $\frac{OA_{930}}{OA_{975}}$ in case of lipid and the per wavelength normalized difference $\frac{OA_{1100}-OA_{1000}}{100}$ in the case of BSA. We explored the muting point's modifications as a function of solute concentration and measured the OA signal as a function of temperature for a carbohydrate, a protein, and a lipid solution. Previously, the optoacoustic signal's temperature-dependence has been utilized for determining the temperature of a sample; for example, during thermal therapy using focused ultrasound [110], [111], or while ablating tissue with a laser fiber [112], [113]. This dependency has also been used to discriminate nonlinear optoacoustic emission of gold nanospheres dissolved in water from the linear optical absorption of the water solvent in the NIR-I region [114]. However, the effects of muting water responses at about the 4 degrees Celsius temperature has not been previously explored. We show a new spectroscopic approach by exploiting this muting property and demonstrating benefits in utilizing optoacoustic readings over conventional optical readings, common in IR spectroscopy.

Our demonstration and analysis focused on the IR wavelengths, particularly in the SWIR range, and addressed the long-standing problem of strong light absorption by water in this spectral region, which challenges the detection sensitivity. Moreover, it has been particularly challenging to detect metabolites such as glucose since both water and glucose molecules have the O-H group, giving rise to a similar spectrum with a strong absorption peak at 1440 nm. As per Figure 4.2, we can conclude that the generated OA signal from the water below 4 °C changes its polarity i.e., negative peak will be followed by the positive peak (because of thermal expansion coefficient becoming negative). Conversely, the OA signal generated from glucose retains a positive peak sequence followed by a negative peak at temperatures below 4 °C. As a result, there would be an interaction of these two OA signals generated due to water and glucose molecules, resulting in the shifting of the muting point to 3 °C (below 4 °C). By lowering the temperature and muting water contributions, we enable more sensitive spectroscopic detection of glucose and possibly other biomolecules, as elaborated in Figure 4.3, Figure 4.5, Figure 4.7.

We provide evidence that the “muting point” can be observed at all SWIR wavelengths and represents an essential CIROAS feature that allows up to 5-fold improved sensitivity in biomolecule detection compared to room-temperature spectroscopy. For the glucose solution, the exact muting point and the slope of the optoacoustic signal's thermal dependence were shown to depend on glucose concentration. This trend could be modeled by assuming a thermal expansion coefficient β that depends on solute concentration analogously to other colligative water properties, such as boiling point freezing point and vapor pressure [115], [116]. We show that the dependence of muting point on the solute concentration can be employed to quantify the concentration of biologically relevant solutes, i.e., CIROAS measurements at different temperatures can quantify the concentration of solutes in aqueous solutions. The results further show that besides glucose, CIROAS improves the sensitivity of the detection of protein and lipid, which opens up the possibility of improving the detection of many other biomolecules, such as lactose, sucrose, galactose, cathepsin, integrin, and myosin. Optoacoustic measurements in the SWIR spectral range are unaffected by other abundant, but weakly absorbing chromophores such as hemoglobin and melanin, making CIROAS an attractive method for metabolites' measurements in solution.

5 Future and outlook

During this work, we designed, built, and characterized two spectroscopic systems based on the optoacoustic effect in SWIR. The main goal was to push the boundaries of sensitivity and selectivity with a reasonable depth of penetration. This particular ability is vital for studying biological samples in an experimental animal model.

The LSOS, presented in chapter 3, has made it possible for the first time, to detect glucose from the most informative layer of the skin at hypodermis. The correlation of the assessed optoacoustic signals to blood sugar levels changes is always challenged by the imprecise dynamics of bulk skin measurements. Initially, we merged an optoacoustic spectrometer employing light in the SWIR region with a machine-learning algorithm to evaluate glucose levels at different skin depths in live mice. The LSOS showed an outstanding correlation of the optoacoustic signal with gold standard glucose readings obtained from blood samples in all control mice and mice injected with glucose. Our results significantly strengthen the accuracy of preceding initiatives to assess glucose through the OA or purely optical approaches, giving a practical path to produce a non-invasive, optical-based product for glucose monitoring, which is much needed for people with diabetes. We discovered that exclusively focusing on the hypodermis enhances the correlation of the OA signal with changes in blood glucose levels more accurately. The application of SWIR radiation allows for much deeper penetration than MIR, allowing direct measurements from the blood in the hypodermis region. LSOS relies on two path designs to minimize the consequences of unavoidable fluctuations in the laser beam energy throughout spectral specifications. It allows real-time modification of the laser beam emission profile at various wavelengths.

Regardless of the benefits of LSOS over conventional optical approaches, there are still difficulties to be overcome. The layer segmentation technique is based on supervised learning of a small dataset, thus requiring annotated labeling for training the models. In the future, we aim to obtain more measurements to be enough to perform unsupervised learning methods to cluster the skin layers. Additionally, like all pre-existing glucose monitoring approach, LSOS need to be calibrated before each experiment. As a next step, as we validate glucose from the skin's hypodermis layer, we hypothesize to build a calibration-free device. This is possible as we target the glucose from the depth in the skin, which does not rely on optical skin property.

We have also developed another technique, which we call cooled IR OA spectroscopy (CIROAS). In a preliminary device, we performed it *in situ* to exploit the dependence of optoacoustic signals on temperature for improving the sensitivity of infrared spectroscopy. Compared to measurements at room temperature, CIROAS at 4°C yielded on an average, a 5-fold sensitivity improvement in the SWIR wavelength range, over measurements at room temperature. The effects of muting water responses at about 4 °C has not been previously explored. Accordingly, we show, therefore a new spectroscopic approach and demonstrate its benefits in utilizing optoacoustic readings over conventional optical readings, common in IR spectroscopy. Furthermore, our approach provides a solution to the long-standing problem of strong light absorption by water in this SWIR region that shadowed other metabolites detection sensitivity. It has been particularly challenging to detect metabolites such as glucose, since both water and glucose molecules have the O-H group, giving rise to a similar spectrum. We also observed that the muting point shifts in different solutions. This is due to the interaction between solute polarization (typically with positive OA peak following by negative peak) and water’s (negative OA peak following by positive OA peak) at the muting point.

CIROAS involves changing the temperature, which alters the speed of sound [117], [118], thereby changing the optoacoustic sources calculated position. However, the change in position should not pose a problem for the quantitation of solutes in a homogeneous solution. Nevertheless, accurate determination of sound speed may be useful, especially since it can allow an estimation of sample temperature [119] during solute quantification or spectral analysis or in imaging applications [120]. CIROAS appears to be superior to alternative optical spectroscopic methods that use heavy water to overcome the effects of strong water absorption [79]. Besides being impractical and cost-ineffective, heavy water is not compatible with measuring biological samples that consist of >80% of water.

Broad implementation of CIROAS will require hardware that allows the variation of the sample's temperature, using a Peltier element or other means. Such implementations are widely available, and they do not represent a technological barrier. Therefore, CIROAS can enable a new spectroscopic approach with high dissemination potential offering a straightforward way to improve the sensitivity of the detection of various molecules in biological samples. The method can be employed for conventional laboratory measurements or for analyzing biological fluids, such as blood measurements. Miniaturization of components is also technically straightforward, which implies applications in conventional spectroscopy or as part of micro-fluidic and lab on a chip measurement setup. In the future, imaging implementations using two- or three-dimensional optoacoustic scans can also be contemplated. So far, we employed CIROAS *in situ* applications, but our ultimate goal is to combine the LSOS system and boost glucose detection sensitivity *in vivo*.

List of Figures

Figure 2.1 The energy diagram depicts the excitation and relaxation mechanism. hv represents the photon energy, and A, F, P, and R denote absorption, fluorescence, phosphorescence, and Raman scattering [37]. 8

Figure 2.2 Simulated OA signal generated by spherical absorber with different diameters measured at 500 µm from a sphere and using equation (2.16). a) Time-domain signals, b) Frequency-domain signals [37], [49]. 18

Figure 2.3 Cross-section view of a single element transducer. The main components are; the piezoelectric element, the backing, and matching layers. 22

Figure 3.1 Schematic representation of LSOS; UST– ultrasound transducer; BS – beam splitter; AMP – Amplifier; DAQ – data acquisition card; L – lenses, PL – Polarizer, HWP – Half waveplate. The inset figure shows the skin's placement from the back of a mouse under the UST holder. 25

Figure 3.2 Pulse energy spectrum of the OPO laser at five wavelengths. a) Pulse energy without applying HWP and polarizer to control the pulse energy, b) pulse energy using a combination of HWP and polarizer, and setting the output pulse energy at 0.2 mJ at all wavelengths. 27

Figure 3.3 LSOS Algorithm for in vivo measurements: 1) collecting OA signals in dual-path in the range 1450-1800 nm, 2) skin sectioning, 3) OA Intensity calculation, 4) Pulse-to-pulse correction, 5) glucose signal’s contrast improvement, 6) LOOC, 7) invasive measurement every 5 minutes using a glucometer (to have one invasive measurement for each cycle of OA measurements from 1450-1800 nm), 8) interpolation to find corresponding reference value (invasive measurement) at the time OA measurement was done, 9) comparison of invasive and non-invasive results. 29

Figure 3.4 LSOS system characterization; fifty pulses were measured at each wavelength, with the final OA intensity value being the mean of the fifty measurements. The figure exhibits the SNR improvement of water spectra in the range of 1350 - 2000 nm before (black) and after (red) performing pulse-to-pulse correction, and the inset figure depicts fifty measured pulses at 1920 nm before (black) and after (red) performing pulse-to-pulse correction. 31

Figure 3.5 Sectioning of the OA signal according to skin sectioning using a ML algorithm. A window of ~130 ns in length was moved with ~10 ns step sizes along an acquired OA raw signal at all measured wavelengths, producing spectra using a Hilbert transformation and integral of the signal in the window. These spectra were sorted into three classes corresponding to the dermis, hypodermis, and muscle layers of the skin. a) Histology of the folded skin, b) a sample of a raw OA signal of a section of mouse skin. Each colored line corresponds to a different excitation wavelength. The dotted red lines delineate the skin layers estimated borders, c) classification of spectra corresponding to each time window movement into three skin layers using ML. d-f) Absorption spectra and characteristic absorption of collagen (C), lipid (L), and water (W) from the areas of the OA signal assigned to each skin layer by the ML algorithm as follows: d) the dermis (including the epidermis), e) the hypodermis, and f) the muscle (including fascia). 33

Figure 3.6 Water spectrum versus glucose spectrum; A comparison of the OA intensities (OAI) of glucose that of water (blue squares). The glucose solution was prepared by dissolving glucose powder in heavy water. The glucose signal was calculated by subtracting the heavy water spectrum from the spectrum of the glucose+D2O solution. 38

Figure 3.7 Workflow is showing different stages of the experiment with glucose injected group (N=10) and control group (N=6).. 39

Figure 3.8 Skin histology and changes in thickness and homogeneity of each layer. Here D stands for dermis layer (including epidermis), H stands for hypodermis, and M stands for muscle layer (including fascia). a) Histology of folded skin of three different mice represents how the thickness of skin layers changes in different mice. b) CD31 histology of three different mice to depict blood vessels (red arrow) and follicles/glands (yellow arrow) more clearly and representing the most informative (due to the presence of blood vessels) and the most heterogeneous (change in the structure of the layer through optical paths due to presence of glands) region to sense glucose directly from blood... 40

Figure 3.9 Importance of skin layers and illumination wavelength to glucose sensing. The average correlation coefficient between the OA intensities and test-strip measurements is indicated for the data pooled from all ten animals. Coefficients are shown for specific skin layers, as assigned by the ML algorithm, and for bulk skin, defined as everything from the epidermis to the muscle and fascia. The inset figure shows a comparison of normalized pure glucose spectra with normalized mean of correlation coefficients (CC) in the hypodermis layer, averaged for all ten mice. 43

Figure 3.10 The Clark Error Grid displays the accuracy of the glucose-sensing using OA intensities at 1650 nm wavelength at the (a) dermis, (b) hypodermis, (c) muscle and fascia, and bulk skin (e) in 10 mice after glucose injection. LOOC method was used to predict glucose levels from OA intensities at 1650 nm.. 45

Figure 3.11 A comparison of OA measurements in the skin's hypodermis layer at 1650 nm to reference glucometer readings in ten mice after glucose injection (GI group) and six mice after PBS injection (Control group). Sixteen mice that received glucose injections or PBS were scanned for approximately 50 minutes after injection over the same skin region. The blue square represents OA measurements, and the orange square represents glucometer readings. 48

Figure 4.1 a) Schematic representation of the experimental setup for CIROAS. UST – ultrasound transducer; PD – photodiode; AMP – amplifier; TS – temperature sensor; PM – power meter; ST – stirrer; PE – Peltier Element; PC/ DAQ – personal computer with data acquisition card b) Data processing and analysis steps. OAS raw data (RD, left) was transformed by Hilbert transformation (HT, middle), and the area of interest (AI, right – in blue) under curves was taken as the intensity of the OAS signal (I_{OA}). 63

Figure 4.2 Optoacoustic signal of pure water at different temperatures after illumination in the SWIR range. (a) Raw optoacoustic signal of water at different temperatures after exposition at 1440 nm. (b) The temporal raw optoacoustic signal at 1.8 °C. (c) The temporal raw optoacoustic signal at 21 °C. (d) Optoacoustic spectra of water at different temperatures after illumination in the SWIR range. (e) Comparison of the signal obtained from pure water to varying temperatures after exposure at 1440 nm using optical and optoacoustic measurements. 66

Figure 4.3 Optoacoustic signal of an aqueous solution of glucose (452.2 mg/dl) at different temperatures after illumination in the SWIR range. a) The raw optoacoustic signal at temperatures between 0.6 and 18.5 °C after illumination at 1580 nm. b) Superposition of the optoacoustic signals of pure water (red line) and the aqueous glucose (blue line) solution at 4 °C. c) Optoacoustic spectra of pure water at 4 °C (dotted blue line) and the aqueous glucose solution(dashed black line) at 4 °C. d) Normalized optoacoustic spectra of pure water (solid red), the aqueous solution of glucose at 18 °C (dotted cyan), and the aqueous solution of glucose at 4 °C (dash black). e) Optoacoustic spectra of the aqueous glucose solution at different temperatures after illumination in the SWIR range. f) The absolute normalized difference in OA signal was recorded from aqueous glucose and water solutions at 4 °C, 10 °C, and 18 °C. 69

Figure 4.4 Optoacoustic signal of an aqueous solution of distilled water and saturated glucose at 25 °C and 400 mg/dl aqueous solution of glucose at 4 °C in the SWIR range. (a) Repeat optoacoustic spectra of pure water at 25 °C (solid red line), the aqueous solution of glucose (dashed black line) at 4 °C, and saturated glucose solution (dotted blue line). (b) OA measurements as a function of varying glucose concentration in water at different wavelengths to demonstrate non-linear behavior. 70

Figure 4.5 Temperature dependence of optoacoustic signal measured from water as a function of solute concentration. a) Temperature dependence of the optoacoustic signal intensity of pure water (black squares) and aqueous solutions of glucose at 149.6 mg/dl (red circles) or 452.2 mg/dl (blue triangles). Linear fitting of monotonically increasing signals is shown. (Inset) The muting point of each solution, defined as the intersection with the temperature axis. b) Variation in muting point (T*) with glucose concentration (C_{gl}). c) Variation in muting point (T*) with glucose concentration (C_{gl}) in serum solution. 71

Figure 4.6 Variation in muting point with glucose concentration in water solution (for estimating the minimum distinguishable concentration). 72

Figure 4.7 Optoacoustic signal of an aqueous solution of lipid (10%) and BSA (50 g/L) at different temperatures after illumination in the SWIR range. (A) Optoacoustic spectra of lipids in aqueous solution at different temperatures after illumination in the wavelength range of 890 to 1000 nm. (B) Comparison of normalized OA spectra of lipid solution at 19 °C (dotted orange line) and 4 °C (solid blue line). (C) The optoacoustic signal ratio from the lipid solution at 930 nm (lipid peak) signaled at 970 nm (water peak) at different temperatures. (D) Optoacoustic spectra of BSA in aqueous solution at different temperatures after illumination in the wavelength range of 1000 to 1210 nm. (E) Comparison of normalized OA spectra of BSA solution at 19 °C (dotted orange line) and 4 °C (solid blue line). (F) The gradient in the measured optoacoustic signal from the BSA solution between 1000 and 1100 nm at different temperatures. 75

Figure 4.8 Variation of OA signal as a function of temperature for lipid and BSA solutions. (a) OA measurements as a function of temperature from lipid solution at 930 nm wavelength, (b) OA measurements as a function of temperature from lipid solution at 975 nm, (c) OA measurements as a function of temperature from BSA solution with 1070 nm illumination. 76

Figure 4.9 Ratio of OA signal of Lipid to that of water. a) Ratio of OA signal at 930 nm vs. OA signal at 975 nm for lipid solution at different concentrations (for estimating limit of detection), b) Ratio of OA signal at 930 nm vs. OA signal at 975 nm for lipid solution at different concentrations (for estimating minimum distinguishable concentration). 77

List of Tables

Table 3.1 The correlation coefficient between OAI at 1650 nm (after referencing to 1710 nm) at different skin layers and glucometer measurements. The last six rows are showing the mean and standard deviation of results for all mice (Mean, SD), glucose injected mice group (Mean-GI, SD-GI), and control mice group (Mean-Control, SD-Control), respectively. The green color represents the best results (top 10% at each category), the yellow color showing the results in the first percentile (between top 25 to 10%), and the red color are the worst results.. 49

Table 3.2 Comparing the data located in A region of Clark grid error (∓20% of glucosemeter measurements): the predicted glucose levels are calculated after applying OA measurement at 1650 nm (after referencing to 1710 nm and performing LOOCV) at different skin layers. The percentage of the data located in the A region of the Clark grid error display is shown as a bar plot, where longer bars show the best results, and shorter bars show the worst results. 50

Table 3.3 Comparison of RMSE_{CV} between predicted glucose measurement at 1650 nm (after referencing to 1710 nm and performing LOOCV) at different skin layers and glucometer measurements. The last six rows are showing the mean and standard deviation of results for all mice (Mean, SD), glucose injected mice group (Mean-GI, SD-GI), and control mice group (Mean-Control, SD-Control), respectively. The green color represents the best results (top 10 % at each category), the yellow color showing the results in the first percentile (between top 25 to10 %), and the red color are the worst results. 51

Table 4.1 Indicates the actual concentration and the recovered values from CIROAS measurements and glucometer values. 73

Bibliography

[1] "Diabetes." [Online]. Available: https://www.who.int/health-topics/diabetes#tab=tab_1. [Accessed: 29-Oct-2020].

[2] L. M. M S Ahuja Hemraj B Chandalia *et al.*, "International Journal of Diabetes in Developing Countries Incorporating Diabetes Bulletin Founder Editors Editor-in-Chief Executive Editor Associate Editors NATIONAL ADVISORY BOARD INTERNATIONAL ADVISORY BOARD," 2018.

[3] L. C. Clark and L. M. Bargeron, "Detection and direct recording of left-to-right shunts with the hydrogen electrode catheter," *Surgery*, vol. 46, no. 4, pp. 797–804, Oct. 1959.

[4] A. J. Bandodkar, W. Jia, C. Yard, X. Wang, J. Ramirez, and J. Wang, "Tattoo-Based Noninvasive Glucose Monitoring: A Proof-of-Concept Study," 2015.

[5] W. Gao *et al.*, "Fully integrated wearable sensor arrays for multiplexed in situ perspiration analysis," *Nature*, vol. 529, no. 7587, pp. 509–514, Jan. 2016.

[6] M. J. Tierney, J. A. Tamada, R. O. Potts, L. Jovanovic, and S. Garg, "Clinical evaluation of the GlucoWatch® biographer: A continual, non-invasive glucose monitor for patients with diabetes," in *Biosensors and Bioelectronics*, 2001, vol. 16, no. 9–12, pp. 621–629.

[7] L. Lipani *et al.*, "Non-invasive, transdermal, path-selective and specific glucose monitoring via a graphene-based platform," *Nat. Nanotechnol.*, vol. 13, no. 6, pp. 504–511, 2018.

[8] J. Kim, A. S. Campbell, B. E.-F. de Ávila, and J. Wang, "Wearable biosensors for healthcare monitoring," *Nat. Biotechnol.*, 2019.

[9] J. Heikenfeld *et al.*, "Accessing analytes in biofluids for peripheral biochemical monitoring," *Nature Biotechnology*, vol. 37, no. 4. Nature Publishing Group, pp. 407–419, 01-Apr-2019.

[10] T. Arakawa *et al.*, "Mouthguard biosensor with telemetry system for monitoring of saliva glucose: A novel cavitas sensor," *Biosens. Bioelectron.*, vol. 84, pp. 106–111, Oct. 2016.

[11] J. Kim *et al.*, "Wearable salivary uric acid mouthguard biosensor with integrated wireless electronics," *Biosens. Bioelectron.*, vol. 74, pp. 1061–1068, Dec. 2015.

[12] M. Senior, "Novartis signs up for Google smart lens," *Nature biotechnology*, vol. 32, no. 9. p. 856, 01-Sep-2014.

[13] J. Kim *et al.*, "Wearable smart sensor systems integrated on soft contact lenses for wireless ocular diagnostics," *Nat. Commun.*, vol. 8, 2017.

[14] Z. Sonner *et al.*, "The microfluidics of the eccrine sweat gland, including biomarker partitioning, transport, and biosensing implications," *Biomicrofluidics*, vol. 9, no. 3, 2015.

[15] N. S. Oliver, C. Toumazou, A. E. G. Cass, and D. G. Johnston, "Glucose sensors: A review of current and emerging technology," *Diabet. Med.*, vol. 26, no. 3, pp. 197–210, 2009.

[16] X. Jintao, Y. Liming, L. Yufei, L. Chunyan, and C. Han, "Noninvasive and fast measurement of blood glucose in vivo by near infrared (NIR) spectroscopy," *Spectrochim. Acta - Part A Mol. Biomol. Spectrosc.*, vol. 179, pp. 250–254, 2017.

[17] L. A. Nelson, J. C. McCann, A. W. Loepke, J. Wu, B. Ben Dor, and C. D. Kurth, "Development and validation of a multiwavelength spatial domain near-infrared oximeter to detect cerebral hypoxia-ischemia," *J. Biomed. Opt.*, vol. 11, no. 6, p. 064022, 2006.

[18] K. Maruo, M. Tsurugi, M. Tamura, and Y. Ozaki, "<I>In Vivo</I> Noninvasive Measurement of Blood Glucose by Near-Infrared Diffuse-Reflectance Spectroscopy,"

Appl. Spectrosc., vol. 57, no. 10, pp. 1236–1244, 2003.

[19] A. Taruttis and V. Ntziachristos, "Advances in real-time multispectral optoacoustic imaging and its applications," *Nat Phot.*, vol. 9, no. 4, pp. 219–227, 2015.

[20] H. F. Zhang, K. Maslov, G. Stoica, and L. V. Wang, "Functional photoacoustic microscopy for high-resolution and noninvasive in vivo imaging," *Nat. Biotechnol.*, vol. 24, no. 7, pp. 848–851, 2006.

[21] K. Yoshioka, S. Kino, and Y. Matsuura, "Noninvasive measurement of blood glucose level using mid-infrared quantum cascade lasers," in *Biomedical Imaging and Sensing Conference*, 2017, vol. 10251, p. 102511U.

[22] S. Kino, S. Omori, T. Katagiri, and Y. Matsuura, "Hollow optical-fiber based infrared spectroscopy for measurement of blood glucose level by using multi-reflection prism," *Biomed. Opt. Express*, vol. 7, no. 2, p. 701, Feb. 2016.

[23] C. Vranić *et al.*, "Continuous glucose monitoring by means of mid-infrared transmission laser spectroscopy in vitro," *Analyst*, vol. 136, no. 6, pp. 1192–1198, Mar. 2011.

[24] A. Werth, S. Liakat, A. Dong, C. M. Woods, and C. F. Gmachl, "Implementation of an integrating sphere for the enhancement of noninvasive glucose detection using quantum cascade laser spectroscopy," *Appl. Phys. B Lasers Opt.*, vol. 124, no. 5, May 2018.

[25] S. Liakat, K. A. Bors, L. Xu, C. M. Woods, J. Doyle, and C. F. Gmachl, "Noninvasive in vivo glucose sensing on human subjects using mid-infrared light," *Biomed. Opt. Express*, vol. 5, no. 7, p. 2397, Jul. 2014.

[26] D. I. Ellis and R. Goodacre, "Metabolic fingerprinting in disease diagnosis: Biomedical applications of infrared and Raman spectroscopy," *Analyst*, vol. 131, no. 8. pp. 875–885, 2006.

[27] B. Schrader, "Raman spectroscopy in the near infrared - A most capable method of vibrational spectroscopy," *Fresenius. J. Anal. Chem.*, vol. 355, no. 3–4, pp. 233–239, 1996.

[28] "US7510849B2 - OCT based method for diagnosis and therapy - Google Patents." [Online]. Available: https://patents.google.com/patent/US7510849B2/en. [Accessed: 04-Dec-2019].

[29] I. L. Jernelv, K. Milenko, S. S. Fuglerud, D. R. Hjelme, R. Ellingsen, and A. Aksnes, "A review of optical methods for continuous glucose monitoring," *Appl. Spectrosc. Rev.*, vol. 54, no. 7, pp. 543–572, 2019.

[30] J. J. Burmeister and M. a Arnold, "Evaluation of measurement sites for noninvasive blood glucose sensing with near-infrared transmission spectroscopy.," *Clin. Chem.*, vol. 45, pp. 1621–1627, 1999.

[31] R. Myllylä, "Pulsed Photoacoustic Techniques and Glucose Determination in Human Blood and Tissue," *Handb. Opt. Sens. Glucose Biol. Fluids Tissues Ser. Med. Phys. Biomed. Eng.*, pp. 419–455, 2009.

[32] M. A. Pleitez, T. Lieblein, A. Bauer, O. Hertzberg, H. Von Lilienfeld-Toal, and W. M??ntele, "In vivo noninvasive monitoring of glucose concentration in human epidermis by mid-infrared pulsed photoacoustic spectroscopy," *Anal. Chem.*, vol. 85, no. 2, pp. 1013–1020, 2013.

[33] M. A. Pleitez, T. Lieblein, A. Bauer, O. Hertzberg, H. von Lilienfeld-Toal, and W. Mäntele, "Windowless ultrasound photoacoustic cell for *in vivo* mid-IR spectroscopy of human epidermis: Low interference by changes of air pressure, temperature, and humidity caused by skin contact opens the possibility for a non-invasive monitoring of glucose in the interstitial fluid," *Rev. Sci. Instrum.*, vol. 84, no. 8, p. 084901, Aug. 2013.

[34] M. Á. Pleitez Rafael, “Pulsed mid-infrared photoacoustic spectroscopy for in vivo non-invasive glucose monitoring in human epidermis,” p. 84, 2013.
[35] M. A. Pleitez *et al.*, “Photothermal deflectometry enhanced by total internal reflection enables non-invasive glucose monitoring in human epidermis,” *Analyst*, vol. 140, no. 2, pp. 483–488, Jan. 2015.
[36] J. Y. Sim, C.-G. Ahn, E.-J. Jeong, and B. K. Kim, “In vivo Microscopic Photoacoustic Spectroscopy for Non-Invasive Glucose Monitoring Invulnerable to Skin Secretion Products,” *Sci. Rep.*, vol. 8, no. 1, p. 1059, Dec. 2018.
[37] L. V. ; W. H.-I. Wang, *Biomedical Optics*. 2007.
[38] J. T. Olesberg, L. Liu, V. Van Zee, and M. A. Arnold, “In vivo near-infrared spectroscopy of rat skin tissue with varying blood glucose levels,” *Anal. Chem.*, vol. 78, no. 1, pp. 215–223, 2006.
[39] H. Xu, X. H. Wang, M. P. Persson, H. Q. Xu, M. Käll, and P. Johansson, “Unified treatment of fluorescence and Raman scattering processes near metal surfaces,” *Phys. Rev. Lett.*, vol. 93, no. 24, Dec. 2004.
[40] W.-C. Shih, K. L. Bechtel, and M. V. Rebec, “Noninvasive glucose sensing by transcutaneous Raman spectroscopy,” *J. Biomed. Opt.*, vol. 20, no. 5, p. 051036, Feb. 2015.
[41] K. Ma, J. M. Yuen, N. C. Shah, J. T. Walsh, M. R. Glucksberg, and R. P. Van Duyne, “In Vivo, Transcutaneous Glucose Sensing Using Surface-Enhanced Spatially Offset Raman Spectroscopy: Multiple Rats, Improved Hypoglycemic Accuracy, Low Incident Power, and Continuous Monitoring for Greater than 17 Days,” *Anal. Chem.*, vol. 83, no. 23, pp. 9146–9152, Dec. 2011.
[42] E. A. Moschou, B. V. Sharma, S. K. Deo, and S. Daunert, “Fluorescence glucose detection: Advances toward the ideal in vivo biosensor,” *Journal of Fluorescence*, vol. 14, no. 5. pp. 535–547, Sep-2004.
[43] A. F. Fercher, W. Drexler, C. K. Hitzenberger, and T. Lasser, “Optical coherence tomography - Principles and applications,” *Reports Prog. Phys.*, vol. 66, no. 2, pp. 239–303, Feb. 2003.
[44] A. Bell, “Upon the production of sound by radiant energy,” 1881.
[45] “Radiation-induced thermoacoustic imaging (Patent) | ETDEWEB.” [Online]. Available: https://www.osti.gov/etdeweb/biblio/6241302. [Accessed: 07-Oct-2020].
[46] A. Taruttis and V. Ntziachristos, “Advances in real-time multispectral optoacoustic imaging and its applications,” *Nat. Photonics*, vol. 9, no. 4, pp. 219–227, Apr. 2015.
[47] N. S. Oliver, C. Toumazou, A. E. G. Cass, and D. G. Johnston, “Glucose sensors: a review of current and emerging technology,” *Diabet. Med.*, vol. 26, no. 3, pp. 197–210, Mar. 2009.
[48] Y. Zhou, J. Yao, and L. V. Wang, “Tutorial on photoacoustic tomography,” *J. Biomed. Opt.*, vol. 21, no. 6, p. 061007, 2016.
[49] P. Vetschera, “Engineering Hybrid Optical and Optoacoustic Microscopy for Extended Depth Penetration,” 2019.
[50] L. V Wang and J. Yao, “A practical guide to photoacoustic tomography in the life sciences,” *Nat. Methods*, vol. 13, no. 8, pp. 627–638, 2016.
[51] C. Li and L. V Wang, “Photoacoustic tomography and sensing in biomedicine,” *Phys. Med. Biol.*, vol. 54, no. 19, pp. R59-97, 2009.
[52] “Textbook of in vivo Imaging in Vertebrates - Google Kitaplar.” [Online]. Available: https://books.google.de/books?hl=tr&lr=&id=SfkSijyDwuwC&oi=fnd&pg=PR5&dq=V.+Ntziachristos,+A.+Leroy-Willig,+and+B.+Tavitian,+Textbook+ofin+vivo+Imaging+in+Vertebrates.+J.+Wiley+%26+Sons,+2007&ots=R6LsD_7hSD&sig=8FIRLWD9VXS8GOqiMj8cwiy1p7M&re

dir_esc=y#v=onepage&q=V. Ntziachristos%2C A. Leroy-Willig%2C and B. Tavitian%2C Textbook ofin vivo Imaging in Vertebrates. J. Wiley %26 Sons%2C 2007&f=false. [Accessed: 30-Oct-2020].

[53] X. L. Den-Ben, D. Razansky, and V. Ntziachristos, “The effects of acoustic attenuation in optoacoustic signals,” *Phys. Med. Biol.*, vol. 56, no. 18, pp. 6129–6148, Sep. 2011.

[54] K. Shung, … M. Z.-E. in M. and B., and undefined 1996, “Ultrasonic transducers and arrays,” *ieeexplore.ieee.org*.

[55] A. Maxwell, S. Huang, T. Ling, … J. K.-I. J. of, and undefined 2008, “Polymer microring resonators for high-frequency ultrasound detection and imaging,” *ieeexplore.ieee.org*.

[56] J. Prakash, M. M. Seyedebrahimi, A. Ghazaryan, J. Malekzadeh-Najafabadi, V. Gujrati, and V. Ntziachristos, “Short-wavelength optoacoustic spectroscopy based on water muting,” *Proc. Natl. Acad. Sci.*, p. 201910597, Feb. 2020.

[57] A. Ghazaryan, S. V Ovsepian, and V. Ntziachristos, “Extended Near-Infrared Optoacoustic Spectra of Glucose within the Physiological Concentration Range,” pp. 1–5, 1900.

[58] M. Xu and L. V. Wang, “Photoacoustic imaging in biomedicine,” *Rev. Sci. Instrum.*, vol. 77, no. 4, p. 041101, Apr. 2006.

[59] L. Breiman, “Random Forests,” *Mach. Learn.*, vol. 45, no. 1, pp. 5–32, 2001.

[60] M. Sepaniak *et al.*, “Capillary Electrophoresis Techniques in Biomedical Analysis,” in *Biomedical Photonics Handbook, Second Edition*, CRC Press, 2014, pp. 169–198.

[61] “Near infrared spectroscopy for body fat sensing in neonates: Quantitative analysis by GAMOS simulations,” *Biomed. Eng. Online*, vol. 16, no. 1, p. 14, Dec. 2017.

[62] A. Caduff, M. S. Talary, and P. Zakharov, “Cutaneous Blood Perfusion as a Perturbing Factor for Noninvasive Glucose Monitoring,” *Diabetes Technol. Ther.*, vol. 12, no. 1, pp. 1–9, Jan. 2010.

[63] T. Tajima, M. Nakamura, Y. Tanaka, and M. Seyama, “Advances in Noninvasive Glucose Sensing Enabled by Photonics, Acoustics, and Microwaves,” *Int. J. Autom. Technol.*, vol. 12, no. 1, pp. 64–72, Jan. 2018.

[64] J. Prakash, M. M. Seyedebrahimi, A. Ghazaryan, J. Malekzadeh-Najafabadi, V. Gujrati, and V. Ntziachristos, “Short-wavelength optoacoustic spectroscopy based on water muting,” *Proc. Natl. Acad. Sci.*, p. 201910597, Feb. 2020.

[65] W. L. Clarke, D. Cox, L. A. Gonder-Frederick, W. Carter, and S. L. Pohl, “Evaluating clinical accuracy of systems for self-monitoring of blood glucose.,” *Diabetes Care*, vol. 10, no. 5, pp. 622–8, Sep. 1987.

[66] J. F. BIEBUYCK, “EFFECTS OF ANAESTHETIC AGENTS ON METABOLIC PATHWAYS: FUEL UTILIZATION AND SUPPLY DURING ANEASTHESIA,” *Br. J. Anaesth.*, vol. 45, no. 3, pp. 263–268, Mar. 1973.

[67] A. Ciudin, C. Hernandez, and R. Simo, “Non-Invasive Methods of Glucose Measurement: Current Status and Future Perspectives,” *Curr. Diabetes Rev.*, vol. 8, no. 1, pp. 48–54, 2012.

[68] A. Ghazaryan, S. V. Ovsepian, and V. Ntziachristos, “Extended Near-Infrared Optoacoustic Spectrometry for Sensing Physiological Concentrations of Glucose,” *Front. Endocrinol. (Lausanne).*, vol. 9, p. 112, Mar. 2018.

[69] W. A. Alto, D. Meyer, J. Schneid, P. Bryson, and J. Kindig, “Assuring the accuracy of home glucose monitoring.,” *J. Am. Board Fam. Med.*, vol. 15, no. 1, 2002.

[70] K. Maruo *et al.*, “New Methodology to Obtain a Calibration Model for Noninvasive Near-Infrared Blood Glucose Monitoring,” *Appl. Spectrosc.*, vol. 60, no. 4, pp. 441–449, Apr. 2006.

[71] W. D. (William D. James, D. M. Elston, T. G. Berger, and G. C. Andrews, *Andrews’*

Diseases of the skin : clinical dermatology. Saunders Elsevier, 2011.
[72] P. Libby, P. M. Ridker, and A. Maseri, “Inflammation and atherosclerosis,” *Circulation*, vol. 105, no. 9, pp. 1135–1143, 2002.
[73] L. S. Eberlin *et al.*, “Molecular and Cellular Pathobiology Classifying Human Brain Tumors by Lipid Imaging with Mass Spectrometry,” *AACR*, 2012.
[74] N. Marty, M. Dallaporta, B. Thorens, and B. Thorens, “Brain glucose sensing, counterregulation, and energy homeostasis.,” *Physiology*, vol. 22, pp. 241–51, 2007.
[75] American Diabetes Association, “Diagnosis and classification of diabetes mellitus.,” *Diabetes Care*, vol. 34 Suppl 1, pp. S62-9, 2011.
[76] E. B. Hanlon *et al.*, “Prospects for in vivo Raman spectroscopy,” *Physics in Medicine and Biology*, vol. 45, no. 2. 2000.
[77] A. Glinzer *et al.*, “Targeting Elastase for Molecular Imaging of Early Atherosclerotic Lesions,” *Arterioscler. Thromb. Vasc. Biol.*, vol. 37, no. 3, 2017.
[78] X. Ma *et al.*, “Integrin-Targeted Hybrid Fluorescence Molecular Tomography/X-ray Computed Tomography for Imaging Tumor Progression and Early Response in Non-Small Cell Lung Cancer,” *Neoplasia (United States)*, vol. 19, no. 1, 2017.
[79] Q. Cao, N. G. Zhegalova, S. T. Wang, W. J. Akers, and M. Y. Berezin, “Multispectral imaging in the extended near-infrared window based on endogenous chromophores.,” *J. Biomed. Opt.*, vol. 18, no. 10, p. 101318, 2013.
[80] G. Hong *et al.*, “HHS Public Access,” vol. 8, no. 9, pp. 723–730, 2016.
[81] R. Pandey *et al.*, “Noninvasive Monitoring of Blood Glucose with Raman Spectroscopy,” *Acc. Chem. Res.*, vol. 50, no. 2, pp. 264–272, Feb. 2017.
[82] K. Weinger, A. M. Jacobson, M. T. Draelos, D. M. Finkelstein, and D. C. Simonson, “Blood glucose estimation and symptoms during hyperglycemia and hypoglycemia in patients with insulin-dependent diabetes mellitus,” *Am. J. Med.*, vol. 98, no. 1, pp. 22–31, 1995.
[83] P. Larkin, *Infrared and Raman Spectroscopy; Principles and Spectral Interpretation*. 2011.
[84] H. W. Siesler, Y. Ozaki, and S. Kawata, *Near-Infrared Spectroscopy. Principles, Instruments, Applications*, vol. 16, no. 12. 2002.
[85] S. L. Jacques, “Optical Properties of Biological Tissues: A Review,” *Phys. Med. Biol.*, vol. 58, no. 11, pp. R37-61, 2013.
[86] A. T. Buss, N. Fox, D. A. Boas, and J. P. Spencer, “Probing the early development of visual working memory capacity with functional near-infrared spectroscopy,” *Neuroimage*, vol. 85, pp. 314–325, 2014.
[87] G. A. Wagnières, W. M. Star, and B. C. Wilson, “In Vivo Fluorescence Spectroscopy and Imaging for Oncological Applications,” *Photochemistry and Photobiology*, vol. 68, no. 5. American Society for Photobiology, pp. 603–632, 1998.
[88] R. L. Mccerry, *Raman spectroscopy in chemical bioanalysis.*, vol. 8, no. 5. 2000.
[89] K. Kneipp, H. Kneipp, I. Itzkan, R. R. Dasari, and M. S. Feld, “Ultrasensitive Chemical Analysis by Raman Spectroscopy,” *ACS Publ.*, vol. 99, no. 10, pp. 2957–2975, 1999.
[90] V. Gujrati, A. Mishra, and V. Ntziachristos, “Molecular Imaging Probes for Multi-Spectral Optoacoustic Tomography,” *Chem. Commun.*, vol. 53, pp. 4653–4672, 2017.
[91] J. Laufer, D. Delpy, C. Elwell, and P. Beard, “Quantitative spatially resolved measurement of tissue chromophore concentrations using photoacoustic spectroscopy: Application to the measurement of blood oxygenation and haemoglobin concentration,” *Phys. Med. Biol.*, vol. 52, no. 1, pp. 141–168, Jan. 2007.
[92] A. Rosencwaig, “Photoacoustic spectroscopy of biological materials.,” *Science (80-.).*, vol. 181, no. 4100, pp. 657–658, 1973.
[93] A. C. Tam, “Appliacations of photoacoustic sensing techniques,” *Rev. Mod. Phys.*, vol.

58, no. 2, pp. 381–431, 1986.

[94] G. P. Luke, S. Y. Nam, and S. Y. Emelianov, "Optical wavelength selection for improved spectroscopic photoacoustic imaging," *Photoacoustics*, vol. 1, no. 2, pp. 36–42, 2013.

[95] L. O. Usoltseva, D. S. Volkov, D. A. Nedosekin, M. V. Korobov, M. A. Proskurnin, and V. P. Zharov, "Absorption spectra of nanodiamond aqueous dispersions by optical absorption and optoacoustic spectroscopies," *Photoacoustics*, vol. 12, pp. 55–66, 2018.

[96] T. A. Filimonova, D. S. Volkov, M. A. Proskurnin, and I. M. Pelivanov, "Optoacoustic spectroscopy for real-time monitoring of strongly light-absorbing solutions in applications to analytical chemistry," *Photoacoustics*, vol. 1, no. 3–4, pp. 54–61, 2013.

[97] J. Kottmann, J. M. Rey, J. Luginbühl, E. Reichmann, and M. W. Sigrist, "Glucose sensing in human epidermis using mid-infrared photoacoustic detection," *Biomed. Opt. Express*, vol. 3, no. 4, p. 667, 2012.

[98] A. Ghazaryan, M. Omar, G. J. Tserevelakis, and V. Ntziachristos, "Optoacoustic detection of tissue glycation.," *Biomed. Opt. Express*, vol. 6, no. 9, pp. 3149–56, 2015.

[99] A. Ghazaryan, S. V. Ovsepian, and V. Ntziachristos, "Extended near-infrared optoacoustic spectrometry for sensing physiological concentrations of glucose," *Front. Endocrinol. (Lausanne).*, vol. 9, no. MAR, Mar. 2018.

[100] G. S. Kell, "Precise Representation of Volume Properties of Water at One Atmosphere," *J. Chem. Eng. Data*, vol. 12, no. 1, pp. 66–69, 1967.

[101] I. G. Calasso, W. Craig, and G. J. Diebold, "Photoacoustic point source," *Phys. Rev. Lett.*, vol. 86, no. 16, pp. 3550–3553, Apr. 2001.

[102] E. Petrova, A. Liopo, A. A. Oraevsky, and S. A. Ermilov, "Temperature-dependent optoacoustic response and transient through zero Grüneisen parameter in optically contrasted media," *Photoacoustics*, vol. 7, pp. 36–46, 2017.

[103] L. V. Wang and Hsin-I Wu, *Biomedical Optics: Principles and Imaging*. 2012.

[104] P. Beard, "Biomedical photoacoustic imaging.," *Interface Focus*, vol. 1, no. 4, pp. 602–31, Aug. 2011.

[105] M. F. Cawley, D. McGlynn, and P. A. Mooney, "Measurement of the temperature of density maximum of water solutions using a convective flow technique," *Int. J. Heat Mass Transf.*, vol. 49, no. 11–12, pp. 1763–1772, 2006.

[106] M. V. Kaulgud and W. K. Pokale, "Measurement of the temperature of maximum density of aqueous solutions of some salts and acids," *J. Chem. Soc. Faraday Trans.*, vol. 91, no. 6, pp. 999–1004, 1995.

[107] A. Danielli, K. Maslov, C. P. Favazza, J. Xia, and L. V. Wang, "Nonlinear photoacoustic spectroscopy of hemoglobin," *Appl. Phys. Lett.*, vol. 106, no. 20, May 2015.

[108] A. J. Rose and E. a Richter, "Skeletal muscle glucose uptake during exercise: how is it regulated?," *Physiology (Bethesda).*, vol. 20, no. 131, pp. 260–270, 2005.

[109] G. Freckmann *et al.*, "Continuous glucose profiles in healthy subjects under everyday life conditions and after different meals.," *J. diabetes Sci. Technol.*, vol. 1, no. 5, pp. 695–703, 2007.

[110] M. Kuniyil Ajith Singh and W. Steenbergen, "Photoacoustic-guided focused ultrasound (PAFUSion) for identifying reflection artifacts in photoacoustic imaging," *Photoacoustics*, vol. 3, no. 4, pp. 123–131, 2015.

[111] Y. Sun and B. O'Neill, "Imaging high-intensity focused ultrasound-induced tissue denaturation by multispectral photoacoustic method: an ex vivo study.," *Appl. Opt.*, vol. 52, no. 8, pp. 1764–70, 2013.

[112] E. Bay, A. Douplik, and D. Razansky, "Optoacoustic monitoring of cutting efficiency and thermal damage during laser ablation," *Lasers Med. Sci.*, vol. 29, no. 3, pp. 1029–

1035, 2014.

[113] G. A. Pang, E. Bay, X. L. De??n-Ben, and D. Razansky, “Three-dimensional optoacoustic monitoring of lesion formation in real time during radiofrequency catheter ablation,” *J. Cardiovasc. Electrophysiol.*, vol. 26, no. 3, pp. 339–345, 2015.

[114] O. Simandoux, A. Prost, J. Gateau, and E. Bossy, “Influence of nanoscale temperature rises on photoacoustic generation: Discrimination between optical absorbers based on thermal nonlinearity at high frequency,” *Photoacoustics*, vol. 3, no. 1, pp. 20–25, 2014.

[115] F. C. Andrews, “Colligative properties of simple solutions.,” *Science (80-.).*, vol. 194, no. 4265, pp. 567–71, 1976.

[116] G. S. Manning, “Limiting Laws and Counterion Condensation in Polyelectrolyte Solutions. III. An Analysis Based on the Mayer Ionic Solution Theory,” *J. Chem. Phys.*, vol. 51, no. 8, p. 3249, 1969.

[117] S. Mandal, E. Nasonova, X. L. Deán-Ben, and D. Razansky, “Optimal self-calibration of tomographic reconstruction parameters in whole-body small animal optoacoustic imaging,” *Photoacoustics*, vol. 2, pp. 128–136, Sep. 2014.

[118] J. Jose, R. G. H. Willemink, W. Steenbergen, C. H. Slump, T. G. van Leeuwen, and S. Manohar, “Speed-of-sound compensated photoacoustic tomography for accurate imaging.,” *Med. Phys.*, vol. 39, no. 12, pp. 7262–71, Dec. 2012.

[119] D. de Sompel, L. S. Sasportas, A. Dragulescu-Andrasi, S. Bohndiek, and S. S. Gambhir, “Improving image quality by accounting for changes in water temperature during a photoacoustic tomography scan,” *PLoS One*, vol. 7, no. 10, p. e45337, 2012.

[120] I. Steinberg, D. M. Huland, O. Vermesh, H. E. Frostig, W. S. Tummers, and S. S. Gambhir, “Photoacoustic Clinical Imaging,” *Photoacoustics*, 2019.

List of Publications

Scientific journal publications as a first author:

Prakash, J.(*), **Seyedebrahimi, M. M**.(*, first author with equal contribution**)**, Ghazaryan, A.(*), Malekzadeh-Najafabadi, J., Gujrati, V., & Ntziachristos, V. (2020). “Short-wavelength optoacoustic spectroscopy based on water muting”. *Proceedings of the National Academy of Sciences*, *117*(8), 4007-4014.

Mir Mehdi Seyedebrahimi, Pouyan Mohajerani*, Miguel A. Pleitez*, Jaya Prakash, Ara Ghazarian, Vipul Gujreti. **“**Machine-learning powered, layer-selective optoacoustic sensor for non-invasive glucose measurements in the short-wavelength infrared”, 2020. (In Process)

Seyedebrahimi, M. Mehdi, Pouyan Mohajerani, and Vasilis Ntziachristos. "Non-invasive in-vivo sensing of metabolites with a novel optoacoustic spectroscope in the SWIR." *European Conference on Biomedical Optics*. Optical Society of America, 2019.